

A MICROSTRIP TRANSMISSION LINE RF BIOSENSOR: A BIOSENSING DEVICE TO
MEASURE INTERACTION BETWEEN MICROLITER AQUEOUS SOLUTIONS
AND RADIO FREQUENCIES

A Dissertation
Submitted to the Graduate Faculty
of the
North Dakota State University
of Agriculture and Applied Science

By

Mary Elizabeth Godfrey

In Partial Fulfillment of the Requirements
for the Degree of
DOCTOR OF PHILOSOPHY

Major Program:
Biomedical Engineering

April 2024

Fargo, North Dakota

North Dakota State University
Graduate School

Title

A MICROSTRIP TRANSMISSION LINE RF BIOSENSOR: A
BIOSENSING DEVICE TO MEASURE INTERACTION
BETWEEN MICROLITER AQUEOUS SOLUTIONS AND
RADIO FREQUENCIES

By

Mary Elizabeth Godfrey

The Supervisory Committee certifies that this *disquisition* complies with North Dakota
State University's regulations and meets the accepted standards for the degree of

DOCTOR OF PHILOSOPHY

SUPERVISORY COMMITTEE:

Daniel Ewert

Chair

Benjamin Braaten

Amanda Brooks

Kouhyar Tavakolian

Mijia Yang

Approved:

April 9, 2024

Date

Long Jiang

Department Chair

ABSTRACT

Biosensors exploring the interaction between electromagnetic (EM) energy and aqueous solutions have long been an area of research interest. Previous research designs have employed various experimental setups, testing device structures, and frequency ranges to determine if property changes occur within the aqueous solutions under test after/during exposure to (EM) energy. Previous works have identified needs in the field, including smaller experimental device dimensions, a requirement of nanoliter to milliliter sampling volumes, and the ability to gather repeatable and sensitive measurements.

Research Aim 1: The following dissertation questioned: Is it possible to design a sensor capable of measuring levels of interaction between RF energy and aqueous samples with reasonable reproducibility, sensitivity, and repeatability, all while being small in dimension, inexpensive to produce, and requiring microliter sample sizes?

Research Aim 2: If the abovementioned sensor can be designed and verified, can it be used to measure the interaction levels between a broadband sweep of radiofrequencies and aqueous lambda DNA?

In response to Research Aim 1, a millimeter-sized, microstrip transmission line biosensor with a microliter well operating on a broadband radio frequency range of 1.0-17.0 GHz was designed, simulated, and experimentally verified. Aqueous solutions, including deionized water, Tris-EDTA buffer, and lambda DNA, were loaded into the microliter well, and non-ionizing RF waves were transmitted down the transmission line. S-parameters were measured in sets to determine the interaction between the aqueous solution under test and the broadband radiofrequency sweep. Reproducibility and sensitivity were calculated for experimental data sets.

Experimental data demonstrated 1) the RF biosensor's ability to repeatably measure increasing concentrations of aqueous solutions, for example, lambda DNA diluted in Tris-EDTA buffer, and 2) a high measurement sensitivity, with the highest error value observed being 0.36%. Addressing Research Aim 2, increasing concentrations of lambda DNA diluted in Tris-EDTA buffer were experimentally measured, and reproducible trends were observed. Overall, the RF biosensor design was verified and determined to be a valid solution for measuring interaction levels between radiofrequencies and aqueous solutions of microliter quantities.

ACKNOWLEDGEMENTS

A heartfelt thank you to all who have encouraged and supported me with kind thoughts and words throughout this journey! A special thank you to my supportive husband, Jeff, who has always encouraged me never to quit and for always lending an ear to my ponderings, scientific questions, and ideas. A tender thank you to our newborn son, John, for motivating me to see this research past the finish line. A joyous thank you to my immediate family: Mom, Dad, Angie, Betsy, Julia, Molly, Riley, William, Clair, Stella, Sylvia, Andy, Mary Jo, Gemma, and Oscar! You help me always maintain sight of the end goal, cheered me on, and help me persevere. Thank you also to my friends and colleagues for much friendship, collaboration, and fun!

This work was made possible through help via training, advice, and conversation in the labs of Dr. Benjamin Braaten, Dr. Amanda Brooks, and Dr. Jane Schuh. Thank you for supporting me, encouraging me, and helping me grow throughout this journey! Also, thank you to Dr. Kouhyar Tavakolian for welcoming us to collaborate with your lab and the University of North Dakota's Biomedical Engineering Department. Sending a big thank you to Jerika (Cleveland) Hayes and Ryan Striker who were always available to give insight, advice and quick to lend a helping hand when I got stuck on a thought, experimental design, or simulation error. Thank you!

Finally, huge thank you for being an awesome, inspiring, joyful, and insightful advisor, Dr. Dan Ewert! You have always believed in me, even when I did not, and you truly bring out the best in everyone you meet. Your excitement and passion for teaching and learning are contagious!

DEDICATION

This work is dedicated to my grandparents, who cheered me on throughout my education to stay curious and filled with wonder. Especially my Grandma LaVonne, whose life of deep physical suffering did not stop her from living with a warm, tender heart overflowing with love and a big smile for everyone she met. Her refusal to complain about her own numerous sufferings and always being empathetic to others' trials above her own is my source of inspiration to use my talents towards alleviating the suffering of others via technological advancement.

TABLE OF CONTENTS

ABSTRACT.....	iii
ACKNOWLEDGEMENTS.....	v
DEDICATION.....	vi
LIST OF TABLES.....	xii
LIST OF FIGURES.....	xiii
LIST OF ABBREVIATIONS.....	xv
LIST OF SYMBOLS.....	xix
LIST OF APPENDIX FIGURES.....	xxi
1. INTRODUCTION.....	1
1.1. Impact.....	1
1.2. Research Objective.....	1
1.3. Author’s Publications Based on this Dissertation Work.....	2
1.4. Dissertation Structure.....	2
2. BACKGROUND.....	4
2.1. Forces of Interaction.....	4
2.1.1. Van der Waals Forces.....	4
2.1.2. Aqueous Solutions.....	5
2.1.3. Electric Stimuli Naturally Occurring in Living Organisms.....	5
2.1.4. Coulomb’s Law and Maxwell’s Equations.....	6
2.1.5. Permittivity of a Material.....	8
2.2. Electromagnetic Waves.....	8
2.2.1. Electromagnetic Wave Spectrum.....	8
2.2.2. Ionizing and Non-ionizing Electromagnetic Waves.....	9
2.3. Conservation of Energy.....	9

2.3.1. Reflected Waves and Transmitted Waves	10
2.3.2. Waves Absorbed and Converted to Heat	10
2.3.3. Specific Absorption Rate (SAR)	11
2.3.4. Waves Absorbed and Stored as Energy	11
2.3.5. Molecular Shifting Due to Storage of Electromagnetic Energy.....	12
2.4. Current Measurement Techniques	13
2.4.1. Scattering Parameters	14
2.4.2. Free Space Methods	14
2.4.3. Open-ended Coaxial Probe Method	15
2.4.4. Resonator Techniques	16
2.4.5. Transmission Line and Reflection Techniques	17
2.4.6. Microstrip Transmission Line Theory.....	18
2.5. Sensing Methods Used for Volumes of Microliter to Milliliter Aqueous Solutions	18
2.5.1. Chemical and Biological Sensors.....	19
2.5.2. Optical Detection Systems and Spectroscopy	19
2.5.3. Microfluidic Channels.....	20
2.5.4. Computation Fluid Dynamics	21
3. LITERATURE REVIEW	22
3.1. Detecting Dielectric Properties and Polarizations.....	22
3.2. Biosensor Types	25
3.2.1. Optical Biosensors.....	25
3.2.2. Electromagnetic (EM) Wave Biosensors	26
3.2.3. Biosensing in Terahertz Frequencies	26
3.2.4. Biosensing in Microwave (MW) Frequencies	27
3.2.5. Biosensing in Millimeter Wave (mmW) Frequencies.....	28

3.2.6. Biosensors Operating in Radiofrequencies	29
3.3. Sensors Measurement Detection Techniques and Design Considerations	30
3.3.1. In-vivo versus Ex-vivo Experimentation	30
3.3.2. Label versus Label-free Experimentation	31
3.3.3. Direct versus Indirect Measurement	32
3.3.4. Detection and Measurement Techniques	32
3.4. “The Gap” - Current Needs for Improvement for EM Wave Biosensors	32
3.4.1. Proposed RF Biosensor Meeting “The Gap”	34
4. METHODOLOGY	35
4.1. Proposed RF Biosensor Design.....	36
4.1.1. 2D Simulations in Advanced Design System (ADS).....	36
4.2. 3D Ansys HFSS Simulation Design	38
4.3. Production of the RF Biosensor	39
4.3.1. Simulation File Map, Material Used, and Milling Machine Specifications.....	39
4.3.2. LPKF ProtoMat Milling Machine Accuracy and Repeatability.....	39
4.3.3. Milling the RF Biosensor	40
4.4. Testing the Microliter Well’s Absorbency.....	40
4.5. Testing the Substrate Heating During Experimentation	41
4.6. RF Biosensor Functionality Verification	43
4.6.1. Experimental Stage 1: Full 2-Port Calibration.....	45
4.6.2. Experimental Stage 2: Repeatability of Measurements	45
4.6.3. Experimental Stage 3: Sensitivity of Measurements.....	46
4.6.4. Experimental Stage 4: Reproducibility of Measurements.....	47
4.7. Equipment, Materials Used, and Experimental Setup	47
4.7.1. Preparation of Aqueous Solution Materials	47

4.8. Statistical Analysis and Data Manipulation	49
4.8.1. Scattering Parameter Conversion to Voltage Ratio.....	49
4.8.2. MATLAB	50
4.8.3. Statistical Analysis	51
5. RESULTS	53
5.1. Advanced Design System (ADS) 50- and 75-Ohm Load 2D Simulation Results.....	53
5.2. Ansys HFSS 3D Simulation Final Designs.....	54
5.2.1. Designing SMA Connectors for the Microstrip Transmission Line Biosensor	55
5.2.2. Microstrip Transmission Line Only (Without a Well).....	55
5.2.3. Introduction of Microliter Well.....	55
5.2.4. Resulting Electric and Magnetic Fields: Enough to Reach Well Contents.....	56
5.3. MATLAB Results	58
5.4. Statistical Analysis of Experimental Data.....	59
5.4.1. Resulting Mean, Standard Deviation, and Confidence Interval Calculations Based on Repeatability Data	59
5.5. RF Biosensor Design and Experimental Setup.....	59
5.6. Comparison of Simulation vs. Initial Experimental RF Biosensor Testing.....	60
5.7. Verification of RF Biosensor’s Measurement Validity	61
5.7.1. Repeatability Measurements	62
5.7.2. Sensitivity Measurements	64
5.7.3. Reproducibility of Measurements Independent of Vector Network Analyzers Used.....	65
5.7.4. Determining Interaction by Calculating the DNA Signal	68
6. DISCUSSION.....	72
7. CONCLUSION.....	75
REFERENCES	78

APPENDIX A. ADS TRANSMISSION LINE SIMULATION SOP	90
APPENDIX B. HFSS TRANSMISSION LINE SIMULATION SOP.....	95
APPENDIX C. RF BIOSENSOR MEASUREMENT SOP	98
APPENDIX D. MATLAB EXAMPLE CODE FOR S-PARAMETER TO VOLTAGE RATIO CONVERSIONS	100
APPENDIX E. SAMPLE DATA FOR TESTING MATLAB CODE	102
APPENDIX F. COMPARISON OF HAND CALCULATIONS VERSUS MATLAB SCRIPT ON STATISTICAL ANALYSIS	105

LIST OF TABLES

<u>Table</u>	<u>Page</u>
1. Biosensor Types and Operating Frequency Ranges.	25
2. Resulting Dimension Calculations for the Proposed RF Biosensor Design.	37
3. Thermocouple Study: 15 Minute Continuous Sweep Leaving the Microliter Well Empty.	42
4. Thermocouple Study: 4 Minute Continuous Sweep with Microliter Well Loaded with Deionized Water.	43
5. List of Equipment and Materials Used for Experimentation.	48
6. Calculations of Absolute Average Error, Min/Max Standard Error Range, and Relative Standard Error Range.	65

LIST OF FIGURES

<u>Figure</u>	<u>Page</u>
1. Charge Separation Due to Van der Waals Forces.....	4
2. Biological Functions Dependent on Electrical Stimuli to Function Correctly.	6
3. Charge Alignment Without and With Electric Field Exposure.	6
4. A Parallel Plate Capacitor Example.....	7
5. The Electromagnetic Energy Spectrum.	8
6. Possible EM Wave Energy Pathways After Transmission.	10
7. Real and Imaginary Dielectric Permittivity Frequency Response.	12
8. The Effects of Hydrophobic/Hydrophilic Molecular Behavior During Electric Field Exposure.	13
9. A Horn-to-Horn Antenna Experimental Setup.	14
10. A Dielectric Probe Experimental Setup.....	15
11. Complementary Split Ring Resonators (CSRR) and Split Ring Resonators (SRR) Designs.....	16
12. A Waveguide Setup.	17
13. Microstrip Transmission Line Geometry with E and H-field Lines.	18
14. Process of a Chemical Sensor.	19
15. An Optical Sensor Emitting Light onto A Sample.	20
16. A Microfluidic Device Experimental Setup.	21
17. A Rendering of the Proposed RF Biosensor.	36
18. The 50-ohm Copper Transmission Line with Simulation Mapping Lines.	38
19. The LPKF ProtoMat Milling Accuracy/Repeatability Layout.	39
20. The dry weight (8.6096 grams) and wet weight (8.6493 grams) of RF biosensor during porosity testing.	41
21. Thermocouple Experimental Setup.....	42

22.	Outline of Stages 1- 4 of Experimental Verification of the Proposed RF Biosensor.	44
23.	RF Biosensor Connected to Experimental Setup.....	45
24.	ADS Simulation of 50-ohm Transmission Line of Width 1.7965mm.....	53
25.	ADS Simulation of 75-ohm Transmission Line of Width 0.8160mm.....	54
26.	The Front and Back Faces of the SMA Connector Design Modeled in HFSS.....	55
27.	HFSS RF Biosensor Model: Top, Side, and Ground Plane Views.....	56
28.	Simulated Electric Field Lines at Frequencies 1.5 and 16.625 GHz.....	57
29.	Simulated Magnetic Field Lines at Frequencies 1.5 and 16.625 GHz.....	57
30.	Comparison of ADS and Experimental S_{21} Data for a 50-ohm Transmission Line.....	60
31.	Comparison of HFSS and Experimental S_{21} Data for Testing the Empty Well.....	61
32.	Comparison of Experimental S_{21} Data Measuring an Empty and Distilled Water Within the Microliter Well.....	62
33.	Comparison of Four Consecutive Experimental S_{21} Datasets Measuring an Empty (Air-filled) Microliter Well Displayed in Voltage Ratio.....	63
34.	Comparison of Four Consecutive Experimental S_{21} Datasets Measuring Deionized Water in the Microliter Well.....	64
35.	Voltage Ratio Measurements Taken on Machine A of Tris-EDTA, DI Water, and DNA Diluted in Increasing Concentrations Tris-EDTA Buffer.....	66
36.	Voltage Ratio Measurements Taken on Machine B of Tris-EDTA, DI Water, and DNA Diluted in Increasing Concentrations Tris-EDTA Buffer.....	67
37.	Voltage Ratio Magnitude Calculations from Machine A of the Resulting Signal Contributed by each Concentration of Lambda DNA.....	68
38.	Voltage Ratio Magnitude Calculations from Machine B of the Resulting Signal Contributed by each Concentration of Lambda DNA.....	69
39.	Voltage Ratio Extended Phase Calculations from Machine A of the Resulting Signal of each Concentration of Lambda DNA.....	70
40.	Voltage Ratio Extended Phase Calculations from Machine B of the Resulting Signal of each Concentration of Lambda DNA.....	71

LIST OF ABBREVIATIONS

RF.....	Radio frequency.
EM.....	Electromagnetic.
DNA.....	Deoxyribonucleic acid.
RNA.....	Ribonucleic acid.
Tris-EDTA (or TE).....	Ethylenediamine Tetraacetic acid, a buffer commonly used to store DNA and/or RNA.
S-Parameter.....	Scattering parameter.
GHz.....	Gigahertz.
ADS.....	Advanced Design System.
Ansys HFSS.....	Ansys High-Frequency Structure Simulator.
μ L.....	Microliter.
mL.....	Milliliter.
SAR.....	Specific Absorption Rate.
MUT.....	Material Under Test.
VNA.....	Vector Network Analyzer.
COMSOL.....	A Multiphysics software used to simulate diverse designs, devices, and structures.
CAD.....	Computer-aided Design, a structural simulation software.
MW.....	Microwave.
mmW.....	Millimeter Wave.
THz.....	Terahertz.
LF.....	Low Frequency.
MF.....	Medium Frequency.
PCB.....	Printed Circuit Board.

5G.....	Fifth Generation of Mobile Communications.
6G.....	Sixth Generation of Mobile Communications.
BBB.....	Blood Brain Barrier.
POCT	Point of Care Testing.
UK.....	United Kingdom.
SIW	Substrate Integrated Waveguide.
O ₂	Oxygen.
CO ₂	Carbon Dioxide.
X-ray	A type of Electromagnetic Radiation.
3D.....	Three Dimensional.
R + jX.....	Rectangular form of impedance.
2D.....	Two Dimensional.
.s2p	A Touchstone file extension.
.csv	A Comma-separated Value file extension.
LPKF ProtoMat S63	A machine used for milling and machining various Radio Frequency applications such as microstrip transmission line or patch antennas.
Rogers TMM4.....	A specific type of laminate from Rogers Corporation used for designing Radio Frequency applications.
SMA	SubMiniature version A, a type of connector used with radio frequency connectors.
dB	Decibels.
kHz.....	Kilohertz.
DI Water.....	Deionized water.
dBm.....	Decibels per milliwatt, a measurement of the power level.

Machine A.....	An abbreviation used in this research to denote an E5071C Vector Network Analyzer, 4-port, ranging from 300 kHz – 20 GHz.
Machine B.....	An abbreviation used in this research to denote an N5230A, 2-port, ranging from 10 MHz – 20 GHz.
N-port.....	An electrical network or Blackbox system with N (the number or amount) of ports in the system.
CSRR.....	Complimentary Split Ring Resonator.
SRR.....	Split Ring Resonator.
mm.....	Millimeter.
MHz.....	Megahertz (or $1 \cdot 10^6$ Hertz).
P200 Micropipette.....	A micropipette that holds between 20 μ L-200 μ L of liquid.
log.....	Logarithm of Base 10.
H-field.....	Magnetic field.
T.L.....	Transmission Line.
DE Probe.....	Dielectric Probe.
NIH.....	National Institute of Health.
O ₂	Oxygen.
CO ₂	Carbon Dioxide.
MATLAB.....	Programming language focusing on matrix computations, plotting functions and data, and algorithms.
ADS.....	Advanced Design System, a software package.
VR.....	Voltage Ratio.
SD.....	Standard Deviation.
SE.....	Standard Error.
AE.....	Absolute Average Error.

RSERelative Standard Error.

LIST OF SYMBOLS

Q.....	Charge on capacitor plates.
C.....	Capacitance.
V.....	Voltage.
ϵ	Dielectric permittivity of a material.
A.....	Area of the plates of a capacitor.
d.....	Distance separating the plates of a capacitor.
E.....	Electric field.
D.....	Electric flux Density.
ϵ'	Real portion of dielectric permittivity.
ϵ''	Imaginary portion of dielectric permittivity.
ϵ_r'	Real portion of relative dielectric permittivity.
ϵ_r''	Imaginary portion of relative dielectric permittivity.
T.....	Thickness of the substrate.
H.....	Height of the substrate.
W.....	Width of the substrate.
ϵ_r	Relative dielectric permittivity.
Z.....	Impedance.
l x h x w.....	Length by height by width dimension.
Vol.....	Volume.
Ω	Ohms.
$^{\circ}\text{C}$	Degrees Celsius.
M.....	Molarity.
V_1^+	Incident voltage wave coming from Port 1.
V_1^-	Reflected voltage wave coming from Port 1.

S_{11}	Scattering parameter measurement of the ratio of incident voltage and Port 1 to reflected voltage at Port 1.
S_{12}	Scattering parameter measurement of the ratio of incident voltage and Port 1 to reflected voltage at Port 2.
S_{21}	Scattering parameter measurement of the ratio of incident voltage and Port 2 to reflected voltage at Port 1.
S_{22}	Scattering parameter measurement of the ratio of incident voltage and Port 2 to reflected voltage at Port 2.
$<$	Less than.
$>$	Greater than.
Σ	The sum.
$\sqrt{\quad}$	Square root.
$()^2$	Squaring the value inside the parentheses.
\pm	Plus or minus.
$ $	The absolute value.
$\%$	Percentage.

LIST OF APPENDIX FIGURES

<u>Figure</u>	<u>Page</u>
A1. Screenshot of ADS main workspace screen..	90
A2. The finished 75Ω transmission line model in ADS workspace..	91
A3. Assigning a 2-Port system and frequency setup in ADS for the 50Ω transmission line model.....	93
A4. Assigning a 1.0-17.0 GHz frequency sweep for the 50Ω transmission line model.....	94
A5. Selecting a rectangular plot for S ₂₁ data or any S-parameter of interest.	94
F1. Screenshot verifying MATLAB imported experimental data as expected.....	105
F2. Screenshot verifying MATLAB result matches data combined into a table.	106
F3. Screenshot verifying MATLAB result of dB conversion to voltage ratio values in comparison to hand calculations located in table.	106
F4. Screenshot verifying MATLAB result of point-by-point mean calculation in comparison to hand calculations located in table.	107
F5. Screenshot verifying MATLAB result of standard deviation calculation in comparison to hand calculations located in table.	108
F6. Screenshot verifying MATLAB result of 99.5% confidence envelope calculation in comparison to hand calculations located in table.	108
F7. Screenshot verifying MATLAB result of standard error calculation in comparison to hand calculations located in table.	109
F8. Screenshot verifying MATLAB result of absolute average error calculation in comparison to hand calculations located in table.	109
F9. Screenshot verifying MATLAB result of relative standard error calculation in comparison to hand calculations located in table.	110

1. INTRODUCTION

Biosensors are commonly used in healthcare, diagnostic, and laboratory settings to measure and characterize the behavior of materials under test (MUT), both liquid and semi-solid. Biosensing encompasses a vast field of knowledge, designs, and current research that provides ways to measure biological signals using various combinations of classification types, operating frequencies, and detection methodologies.

1.1. Impact

The ability to measure and characterize MUTs responses to electromagnetic (EM) energy exposure using a biosensing device operating in a broadband radio frequency range, which is non-ionizing and label-free, requiring microliter size volumes, with repeatable and sensitive data measurements saving research labs and diagnostic testing facilities time, money, and laboratory supplies.

My master's work provided evidence for increased levels of interaction between specific radio frequencies and extracellular lambda DNA suspended in Tris-EDTA buffer, using a horn-to-horn antenna setup. The results also identified a need for an experimental setup proportional to sample volume size and whose design decreased experimental uncertainty and measurement errors. Therefore, the research included in this dissertation was proposed, aiming to utilize a microstrip transmission line antenna as a sensing device for measuring the interaction between radiofrequency energy and MUTs to increase the measurement sensitivity and reduce the experimental setup size and sampling volume.

1.2. Research Objective

The following dissertation has a two-part research aim questioning:

Research Aim 1: Is it possible to design a biosensor, which is millimeters in dimension, operating in a broadband frequency range of 1.0-17.0 GHz, and requiring microliter sample sizes, capable of measuring levels of interaction between RF energy and aqueous samples with reasonable reproducibility, sensitivity, and repeatability?

Research Aim 2: If the abovementioned biosensor can be designed and verified, can it be used to measure the interaction levels between the same 1.0-17.0 GHz broadband sweep of radiofrequencies and aqueous lambda DNA?

1.3. Author's Publications Based on this Dissertation Work

At the time of this dissertation publication there were two resulting journal publications resulting from this dissertation work. The first being a 2021 Rocky Mountain Bioengineering Conference paper which focused on the ADS, HFSS and initial experimental validity of the proposed RF biosensor prototype [128]. Next, the resulting validation of the RF biosensor, i.e. experimentally testing the repeatability, sensitivity, and reproducibility of the biosensor design, was published in the MDPI's *Biosensors* Open Access journal in May 2023 [129].

1.4. Dissertation Structure

The following dissertation is formatted as follows: Chapter 2 conducts a literature review, resulting in identifying a gap and also addresses some theoretical frameworks needed to explain the process and results of this work entirely. Chapter 3 discusses the methodology, design, construction, sample preparation, and equipment used in this research. Chapter 4 lays out the results of all simulations and experimentation. Chapter 5 discusses lessons learned from the experiments and research. Finally, Chapter 6 makes conclusions determined from the results. Additionally, the Appendices at the end of this dissertation contain Standard Operating

Procedures (SOP) for simulation creation and experimental protocols, MATLAB code, and example data.

2. BACKGROUND

To fully understand all aspects of the following research, a foundation will be laid involving numerous topics from various disciplines. To begin with, types of forces, specifically Van der Waals, will be examined along with how the interactions between EM energy and aqueous solutions can be related through 1) measuring these forces via permittivity values and 2) can be theoretically derived using Maxwell's equations and Coulombs Law.

2.1. Forces of Interaction

2.1.1. Van der Waals Forces

Organisms are structured and held together by various bonds, attractions, and interactions. Van der Waals forces focus on the interactions and attractions between ions and molecules while trying to maximize the separation between positive and negative ions, as seen in Figure 1 [1]. Compared to hydrogen, covalent, and ionic bonds, Van der Waals forces are weak in strength and energy. Nonetheless, these interaction forces still influence the behavior of living things based simply on the shifting of positively and negatively charged ions [2], [3].

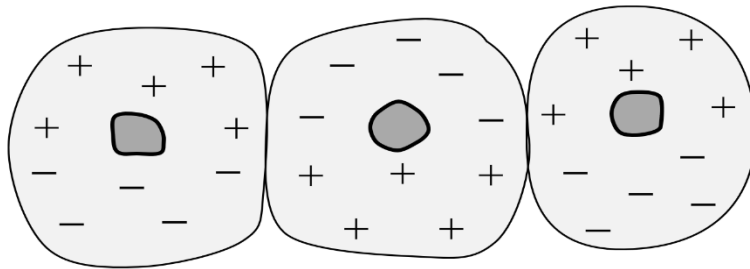


Figure 1. Charge Separation Due to Van der Waals Forces.

Note: Positive and negatively charged ions disperse themselves out to maximize space between other similarly charged ions. Van der Waals forces are weak interactions that attract or repel molecules to each other.

2.1.2. Aqueous Solutions

Water is the most abundant and well-studied biological resource. Water acts as a solvent for one or more compounds or chemicals, resulting in what is known as an aqueous solution [4]. The aqueous solution has measurable properties such as conductivity and dielectric constant depending on what solute is dissolved into the water. These properties can be changed, for example, by varying the concentration of solutes dissolved in water or by exposing the solution to an external electric field [5]. Knowing the conductivity of a material gives information on how electric currents travel through that material under test, and the dielectric constant describes how electric energy is stored within the material.

2.1.3. Electric Stimuli Naturally Occurring in Living Organisms

Along with interaction forces, electric gradients naturally occur in organisms such as biomolecules, tissues, and cells. Examples of this phenomena, shown in Figure 2., include transmembrane potential, voltage-regulated ion pumps, neural electrical stimuli, and cell depolarization, which are all naturally occurring processes in healthy cells. Any external electric stimuli, such as an applied electric field, would introduce energy into a system that experiences signal responses in millivolt (mV) voltage changes. Therefore, an externally applied electric field influences organisms' functions by triggering responses due to the addition of energy, for example, adding positively or negatively charged ions or molecules to the system [6].

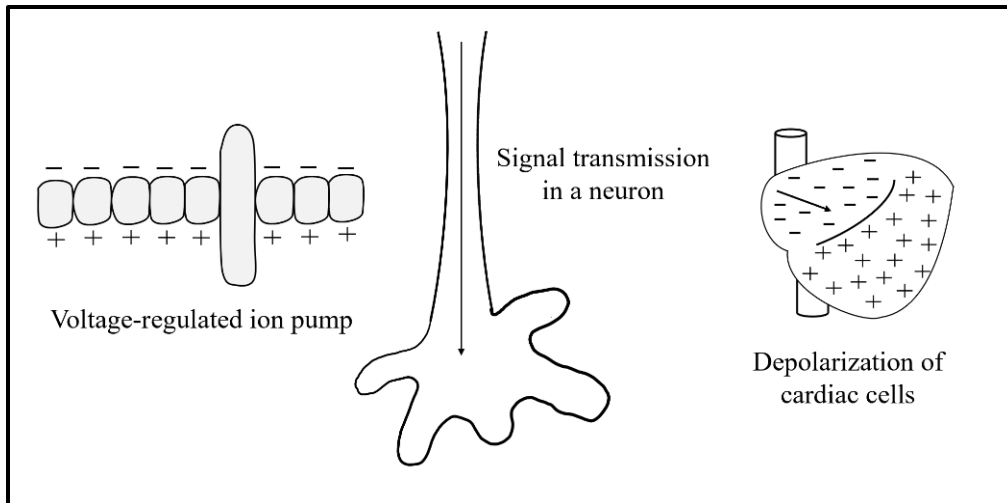


Figure 2. Biological Functions Dependent on Electrical Stimuli to Function Correctly. Note: Examples of external electric field exposure influencing biological processes within the human body include activation of voltage-regulated ion pumps, signal transmission in neural networks, and depolarization of cardiac cells for cardiac contraction.

2.1.4. Coulomb's Law and Maxwell's Equations

Using Coulomb's Law and Maxwell's equations, electric field lines resulting in charge attraction or repulsion can be determined. When an applied electric field passes through a material, as seen in Figure 3, the field lines allow for the reorientation and polarization of charges inside the material.

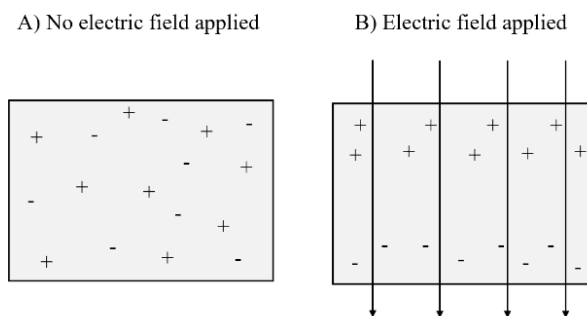


Figure 3. Charge Alignment Without and With Electric Field Exposure. Note: With no electric (E) field present, ions are evenly dispersed within a material. After exposure to an E field, ions become polarized, similar to what happens in a parallel plate capacitor.

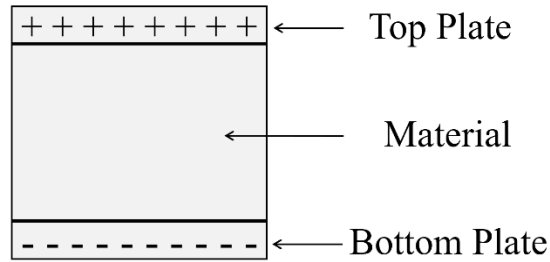


Figure 4. A Parallel Plate Capacitor Example.

Note: The example of a parallel plate capacitor shows how two conductive plates can obtain a difference of positively and negatively charged ions between a material, leading to a voltage drop across the material.

The material's molecular structure, for example, a liquid between two plates, is unchanged due to the breakage of ionic and/or covalent bonds. However, the shifting charges can induce dipoles on these structures. The permittivity of a material, or stored electrical energy inside that material, can be derived by the stored charge, or capacitance, between the two parallel plates as stated in the following charge equation and shown in Figure 4.

$$Q = C \cdot V, \quad \text{(Equation 1)}$$

where Q is the charge, C is the capacitance, and V is the applied voltage. Substituting in an alternate definition of capacitance, permittivity can be determined through the following,

$$Q = \frac{(\epsilon \cdot A)}{d} \cdot V, \quad \text{(Equation 2)}$$

where ϵ is the permittivity of the material, A is the area of the plates, d is the distance separating the plates, and V is the applied voltage [7], [8].

This form of the charge equation relates to how the presence of an applied electric field, E , influences the behavior of ϵ . Specifically, by defining D , the electric flux density, the extent of the electric field inside the material is described as

$$E = \epsilon \cdot D. \quad \text{(Equation 3)}$$

Electric fields can be naturally occurring or artificially introduced, but either way, these fields made up of electric charge can induce electrical currents and have observed effects on living organisms [6].

2.1.5. Permittivity of a Material

Permittivity, ϵ , is the measurement of the amount of energy stored inside the material after exposure to an electric field [9]. Therefore, theoretically deriving or experimentally measuring the permittivity of material demonstrates the electrical response of each specific material under test during electric field exposure. Suppose the permittivity of a material is measured over a range of values. In that case, it can be determined how the material's properties shift with a change in exposure to electromagnetic energy at various frequencies, for example.

2.2. Electromagnetic Waves

2.2.1. Electromagnetic Wave Spectrum

Electromagnetic (EM) waves are waves of energy that contain an electric and a magnetic part, an example being the sun's rays. EM waves occur over many frequencies, meaning their wavelength varies and oscillates at different rates. The Electromagnetic Wave Spectrum plots the

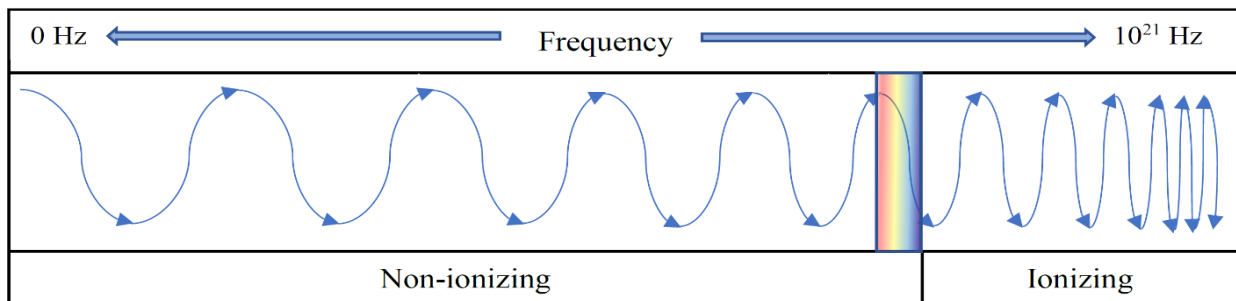


Figure 5. The Electromagnetic Energy Spectrum.

Note: The frequency of the EM wave will affect the wave's properties. Lower frequencies oscillate more slowly and have a longer wavelength. EM waves with higher frequencies oscillate more quickly and have a shorter wavelength. The EM Energy Spectrum can be broken into two wavelength classifications: non-ionizing and ionizing radiation.

broad range of frequencies of EM waves, as seen in Figure 5. Overall, EM waves can be split into two categories based on frequency: non-ionizing and ionizing [8].

2.2.2. Ionizing and Non-ionizing Electromagnetic Waves

Ionizing EM waves have a higher frequency, inversely meaning the wavelength is shorter, and since ionizing waves have shorter wavelengths, they travel through space carrying a higher amount of energy. Upon meeting a surface or object, the energy carried by ionizing waves travels deeply within the object and has substantial amounts of energy, which is absorbed by the object. This absorbed energy is large enough to dislodge atoms from molecules and cause other molecular damage. Other pathways the transmitted energy can take are to be transmitted or reflected by the surface or object. These phenomena will be discussed in greater detail in later sections.

In comparison, non-ionizing waves traveling through space oscillate at a slower frequency and, therefore, have longer wavelengths. Non-ionizing waves carry lower amounts of energy because of these properties. Therefore, upon reaching a surface or object, non-ionizing waves do not carry enough energy to cause the profound cellular and molecular changes that ionizing waves do. Based on this characteristic, non-ionizing waves are less harmful to human health [10].

2.3. Conservation of Energy

Based on the Conservation of Energy, all the energy from an electromagnetic wave traveling through any medium must always be accounted for; energy cannot be created or

destroyed. So, when an EM wave encounters a surface or object, the energy of the wave has four options seen in Figure 6: 1) energy storage, 2) dissipation of heat, 3) transmission through the object, or 4) reflecting off the object's surface [11].

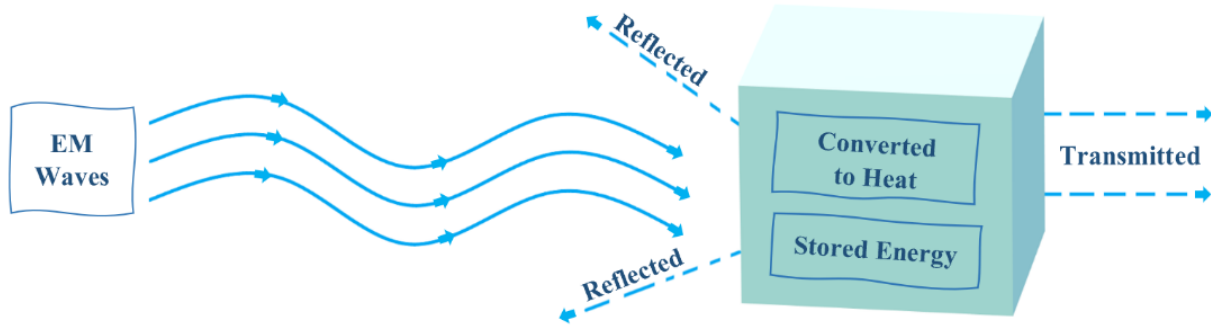


Figure 6. Possible EM Wave Energy Pathways After Transmission.

Note: Energy cannot be added or destroyed based on the Conservation of Energy. To account for energy conservation, an incident EM wave after hitting the surface of an object is either 1) reflected, 2) transmitted, 3) dissipated as heat, or 4) stored as energy by the object.

2.3.1. Reflected Waves and Transmitted Waves

Upon reaching an object or medium, electromagnetic waves have two options: 1) to be reflected by the object or medium or 2) transmitted through the object or medium. If an EM wave is reflected, the reflection coefficient can calculate the amount of the wave reflected. Similarly, the transmission coefficient calculates the amount of the EM wave that passes through the object or medium without any interaction. Although the total energy of the EM wave needs to be accounted for due to the Conservation of Energy, the following research takes an interest in the portion of the EM wave that is absorbed by the object or material [11].

2.3.2. Waves Absorbed and Converted to Heat

A portion of a propagating EM wave energy may be converted from electrical energy to mechanical energy after being absorbed by an object or medium via heat production. Heating effects due to EM radiation have been well studied by research spanning decades. The thermal effects, such as self-heating of tissues and cells, raise the temperature beyond the point of

viability [12], [13], [14], [15], [16], [17]. Therefore, safety measures such as the specific absorption rate are regulated to define power levels that do not rise above what is considered harmful to the healthy function of humans by reducing/limiting heating due to EM wave exposure [18].

2.3.3. Specific Absorption Rate (SAR)

To ensure humans are not exposed to harmful levels of ionizing or non-ionizing radiation produced by electronic machines and devices, worldwide and governmental organizations have created guidelines on radiation exposure safety limits. These limits are known as the Specific Absorption Rate (SAR), the amount of radiation energy absorbed by an object relative to its mass [15], [18].

2.3.4. Waves Absorbed and Stored as Energy

The phenomenon of absorption converted to stored energy can be explained as a small portion of a total EM wave's energy being stored by the material under test (MUT). This stored energy rearranges charges and/or ions inside the material, polarizing a portion of the material. These polarization effects can be measured using dielectric property measurements, such as permittivity. Types of polarizations may include ionic, cellular membrane, and dipolar orientational polarization, which may occur in the tested liquid materials. These types of polarization occur when an applied electric field causes the positive and negative ions and molecular dipoles, whether permanent or instantaneous, to shift in efforts to orient themselves most favorably [1], [19], [20], [21]. The proposed research will be conducting measurements in

the Gigahertz of the Radiofrequency (RF) frequency range, labeled RF in Figure 7.

Inside the range of RF exposure, the predominate polarization is interfacial polarization, but ionic and dipolar polarizations are also seen. Ionic polarization is the alignment of ions within a dielectric material, and dipolar polarization is when dipoles on a molecule move due to an electric field stimulus. Interfacial polarization occurs when positive and negative charges align along the cell membrane [22].

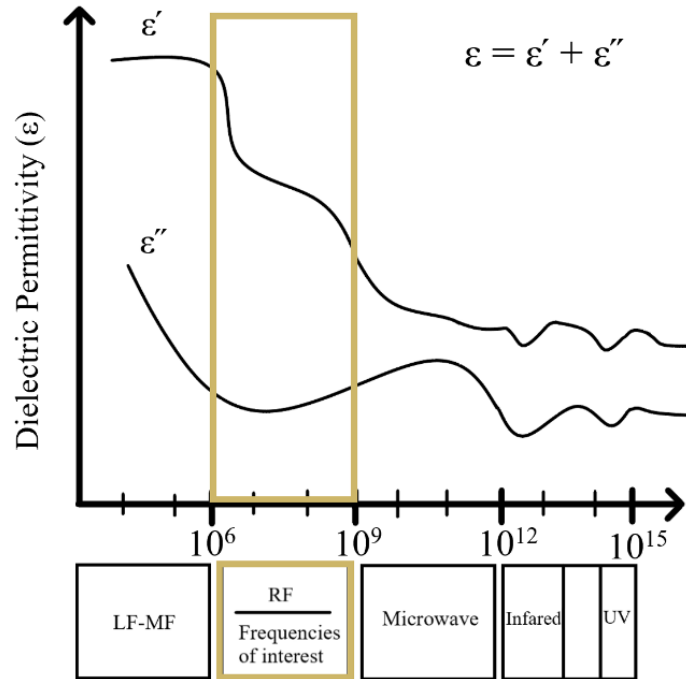


Figure 7. Real and Imaginary Dielectric Permittivity Frequency Response. Note: This research will operate in the RF region of EM waves. The dielectric permittivity measurements' real (ϵ') and imaginary (ϵ'') portions could give insight into ionic or cell membrane polarization behaviors.

2.3.5. Molecular Shifting Due to Storage of Electromagnetic Energy

Polarization and reorientation of ions can affect the behavior of a material's hydrophobic and hydrophilic portions. Figure 8 illustrates the following example of how an intercellular DNA molecule experiences changes due to an applied electric field. For example, the hydrophobic and hydrophilic portions of a DNA molecule keep the molecule stable in shape and orientation.

Suppose this same DNA molecule is located inside a cell, primarily composed of a polar, aqueous liquid, and this intercellular liquid becomes polarized due to an externally applied electric field. In that case, the DNA molecule will also experience these effects. The change in the overall charge of the intercellular solution may result in the hydrophobic portion of a molecule reorienting itself outside of the hydrophilic portion. A molecular reorientation could cause the DNA molecule to change structurally, consequently altering the molecule's functionality [1], [23].

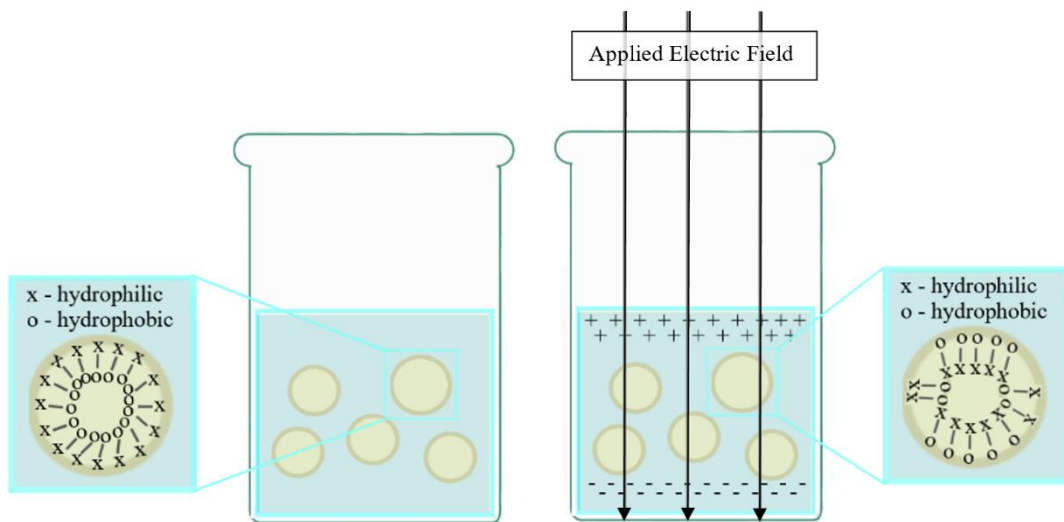


Figure 8. The Effects of Hydrophobic/Hydrophilic Molecular Behavior During Electric Field Exposure.

Note: Polar solutions can maintain their stable orientation and structure without an external electric field. Hydrophobic portions are inside the molecule and surrounded by hydrophilic portions, which meet the solution's molecules, namely water. By polarizing the liquid, the hydrophobic portions may switch orientation with the hydrophilic portions, creating an unstable structure within the molecule.

2.4. Current Measurement Techniques

The main categories of measurement techniques operating with RF sources and used to gather complex permittivity values are discussed below. However, the measurement techniques discussed below do not include exhaustive subsets of each main category.

2.4.1. Scattering Parameters

Using lab equipment, scattering (S) parameters can be obtained, and the resulting interaction between a material under test (MUT) from exposure to EM fields. These parameters explain how the EM waves are transmitted and reflected down a transmission line. From scattering parameters, dielectric property values can be derived [7].

2.4.2. Free Space Methods

A free space measurement method includes a MUT between free space measurement equipment. Figure 9. demonstrates a free space experimental system that includes a horn-to-horn antenna setup with the MUT located in free space between those antennas [19], [24], [25], [26]. EM waves traveling through free space are measured by both antennas, connected to a Vector Network Analyzer (VNA) via coaxial cables to measure S-parameters. S-parameters are a ratio measurement of signal sent by the transmitting antenna and then reflected by that antenna or received by the second receiving antenna [8]. This method was used in my master's work to measure microliter (μL) solutions during exposure to RF waves. The most significant advantage of using this setup is its ability to measure the interaction level of a solution non-invasively through a wide range of frequencies [27].

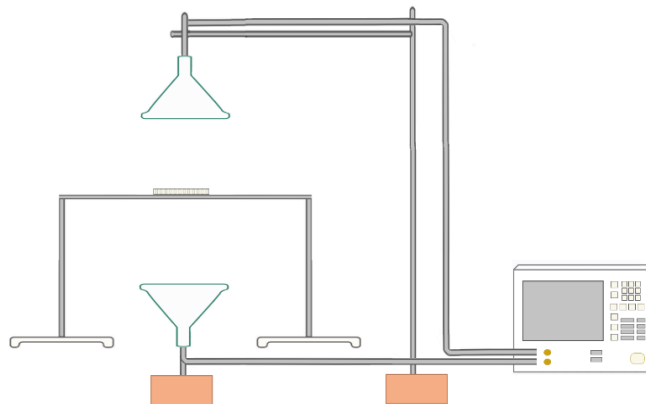


Figure 9. A Horn-to-Horn Antenna Experimental Setup.

Note: A horn-to-horn antenna setup is an example of a free space method where EM waves are transmitted through free space from one antenna to another.

2.4.3. Open-ended Coaxial Probe Method

The open-ended coaxial probe is another measurement method that can non-destructively measure interactions of a MUT to RF wave exposure. EM waves are propagated through a material, such as a liquid, and the dielectric properties are measured by a piece of equipment called a VNA. A dielectric probe is the best example in this category as seen in Figure 10. Other methods may include a waveguide or dielectric resonator [19], [24], [25], [28]. A dielectric probe setup is an easy-to-use, standard measurement tool requiring a single calibration to take sample measurements from various materials. The results are displayed in a Debye graph, and many solutions have been characterized using this method [29]. One drawback to using an open-probe method is the large sample volume needed for testing. This large volume is needed to reduce the effects of EM wave reflections off the edges of the measurement containers. Since the overarching goal of the following dissertation research is to measure microliter to milliliter solutions, this technique will not be used.

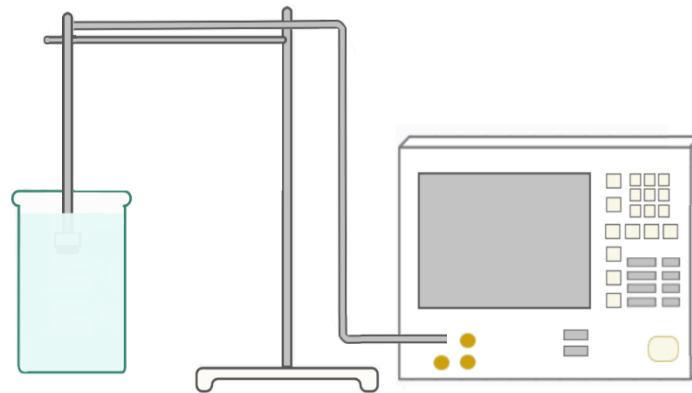


Figure 10. A Dielectric Probe Experimental Setup.

Note: A coaxial cable connects a dielectric probe to a VNA. The DE Probe measures semi-liquid and liquid material's dielectric properties. For example, the probe is inserted into the liquid solution in a liquid material, and EM waves propagate out from the probe end.

2.4.4. Resonator Techniques

Resonant techniques measure materials' complex relative permittivity, ϵ_r' (real part) and ϵ_r'' (imaginary part), by transmitting EM waves across a substrate's surface. This technique's sensors are classified as resonators or narrowband sensors because they are designed to work on a single or small range of frequencies. Numerous resonators have been designed to measure changes in small volumes of solutions [19], [20], [24], [30].

Two common types of resonators are complementary split-ring resonators (CSRR) and split-ring resonators (SRR) simply sketched in Figure 11. CSRRs are commonly included along with the use of metamaterials to act as chemical sensors to measure S-parameters of solutions such as methanol and ethanol [31], [32]. SRRs have also been designed to act as chemical sensors and work along with metamaterials and microfluidic channels [33] for dielectric measurement [34]. SRRs have also been used to measure DNA hybridization from S-parameter measurements [35].

The resonant techniques discussed above have many favorable features, such as 1) accurately characterizing dielectric properties by approximating electric and magnetic fields of new MUTs, 2) requiring a small sample size, 3) being small in dimension, and 4) being

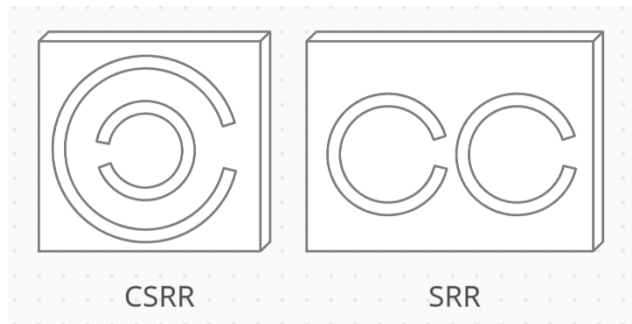


Figure 11. Complementary Split Ring Resonators (CSRR) and Split Ring Resonators (SRR) Designs.

Note: CSRRs and SRRs are typically designed for single-frequency and can be used for testing the material's dielectric properties by placing the material on the structure's surface.

inexpensive to produce. However, resonant techniques are best used with designs for limited frequencies and low-loss materials [19], [36]. Low-loss materials are materials that have low electron mobility and the ability to move charges and form dipoles [37], which are not materials expected to be tested in this dissertation research.

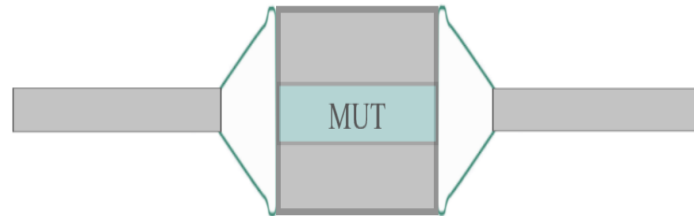


Figure 12. A Waveguide Setup.

Note: A waveguide provides a closed path for EM waves to travel with a MUT enclosed in the middle of the setup. This is a transmission/reflection technique used for RF material testing.

2.4.5. Transmission Line and Reflection Techniques

Transmission line theory measures a dielectric material's response to an EM wave exposure. The setup of these types of systems includes some MUT, whether solid, liquid, or gaseous, located on or inside a transmission line or waveguide, as shown in Figure 12. The transmission line or waveguide apparatus can determine the permittivity and permeability of a material via coaxial cables connected to a VNA to obtain S-parameter measurements [19], [24], [28], [38].

Additionally, transmission line techniques are preferable for measuring materials with high loss, such as materials that can quickly move electrons or become easily polarized, such as water, which is expected in this research [19]. This measurement technique is popular because it can non-invasively and non-destructively sweep a wide frequency range when experimentally measuring a material's response to RF exposure [29]. However, the accuracy of measurements

using this method is affected by any air gaps, intentional or unintentional, within the setup. Also, low measurement accuracy can be expected when the material's physical length is one-half the wavelength of the wave being transmitted through the material.

2.4.6. Microstrip Transmission Line Theory

A microstrip transmission line is a type of antenna that is categorized by having a copper line, known as a transmission line, running from one edge to another of milled material. Usually, the shape of a microstrip transmission line is rectangular and has the transmission line milled on the top and a copper plane, known as the ground plane, on the bottom as seen in Figure 13. Passing an energy source, such as an EM wave, down the transmission line produces an electric and magnetic field from the copper line. Based on the frequency passed down the line, the electric and magnetic fields oscillate more quickly or slowly [39].

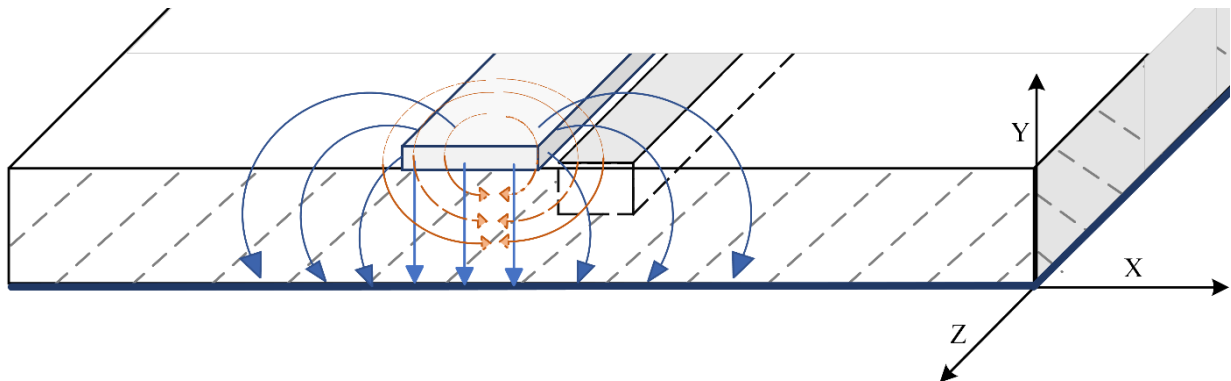


Figure 13. Microstrip Transmission Line Geometry with E and H-field Lines.

Note: The microstrip transmission line geometry consists of a square or rectangular shape with a conductive ground plane (dashed blue) and transmission line (top plane). The radiation pattern consists of electric field lines (solid blue) radiating perpendicular to the transmission line in a clockwise and counterclockwise circular pattern. Meanwhile, the magnetic field lines (solid red) radiate parallel to the transmission line.

2.5. Sensing Methods Used for Volumes of Microliter to Milliliter Aqueous Solutions

Many sensing techniques have been used to detect changes, characteristics, and other features from micro- and milliliter liquid solutions. Some popular techniques include

biochemical sensors, optical detection systems, microfluidic channels, computational fluid dynamics, and biosensors.

2.5.1. Chemical and Biological Sensors

As discussed in previous sections, chemical and biological sensors can be designed and incorporated within sensing systems. These sensors are subjected to a sample and work by detecting the presence, or lack thereof, of a specified molecule/compound/organism bound on its receptor. This receptor binding creates a chemical signal which is transmitted to the output and states the detection of a molecule of interest within a given sample, as Figure 14 illustrates [40].

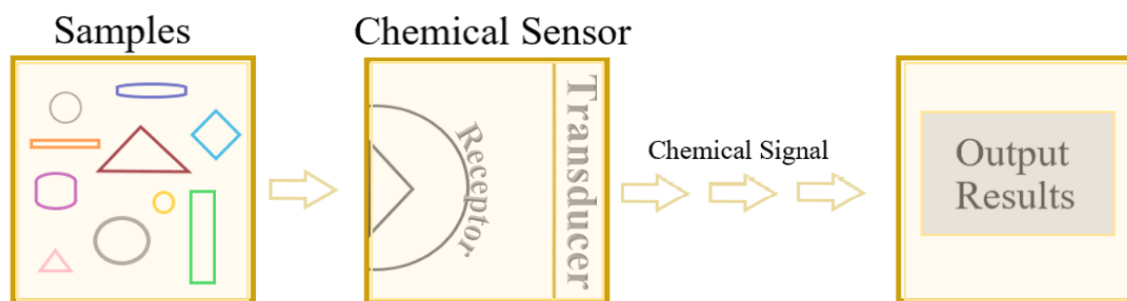


Figure 14. Process of a Chemical Sensor.

Note: Samples can be tested using a chemical sensor. The sensor detects if the sample can bind to a specific receptor and then reports, via a chemical signal, the test results.

2.5.2. Optical Detection Systems and Spectroscopy

Dielectric characterization and analysis can be performed using optical detection and spectroscopy techniques. Staining, fluorescence, and cytometry have been used to fixate and analyze cells and biomolecules for decades [22], [41], [42]. Optical sensing requires the transmission of light onto a sample where a fluorescent stain is added within the sample to indicate the presence of a target molecule, as seen in Figure 15. These procedures can be costly

and time-consuming and could be improved by automation. Using an RF sensing device to take measurements of biological materials' behavior offers a non-destructive, more accurate tool [21].

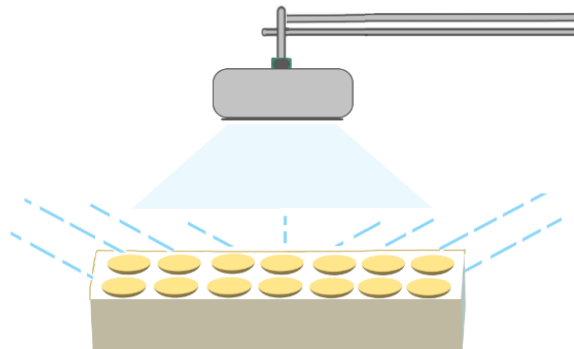


Figure 15. An Optical Sensor Emitting Light onto A Sample.

Note: Using fluorescent detection at a specific light frequency, molecules within the sample may bind with the fluorescent detectors and emit the fluorescence after exposure.

2.5.3. Microfluidic Channels

Microfluidic devices help reduce the number of samples needed when testing biomaterials. All microfluidic devices have the characteristics of pumping a liquid solution through its channels, as seen by a generic rendering in Figure 16. These devices can mix multiple solutions to create reactions for sample analysis [43]. Microfluidics, such as Lab-on-a-chip devices, can measure extremely small-sized samples ranging from 10^{-9} to 10^{-12} liters [44]. These devices push the sample through channels to analyze them. Microfluidic devices can measure samples for characteristics such as protein levels, ionic strength, and other chemical and biological characteristics [45].

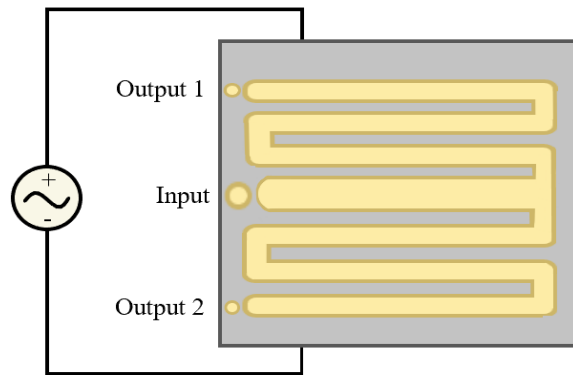


Figure 16. A Microfluidic Device Experimental Setup.

Note: Microfluidic devices can pump solutions through the various channels within the device, each providing results about the solution under test.

2.5.4. Computation Fluid Dynamics

Complex modeling and simulation software have opened many possibilities for researchers to study and test problems that are difficult to measure experimentally. Software programs like ANSYS, COMSOL, CAD (Computer Aided Design), etc., can model and simulate many possibilities without performing any lab experiment [46]. One example of simulations and modeling gaining beneficial information for scientists without lab experimentation is the design of various cardiovascular malfunctions and potential treatments. Virtual modeling saves researchers time and money by identifying which experiments are the best to pursue before entering the lab.

3. LITERATURE REVIEW

This review will investigate the several types of biosensors developed to test milliliter to microliter sample sizes. There are two main categories of biosensors: EM wave biosensors and optical biosensors. There are four main subcategories of EM wave biosensors based on their operating frequency, which are radio frequency (RF), microwave (MW), millimeter wave (mmW), and terahertz (THz) biosensors. A focus will be on the subcategory of RF biosensors, which is a trending sensor design. RF biosensors offer positives over previous sensing designs, which include non-invasive testing and label-free detection.

This review also lays out the current trends in sensing technique and design of sensing apparatus for detecting dielectric properties changes in solutions after exposure to EM waves. By demonstrating design gaps of previous EM wave exposure and measurement setups using microliter solutions for testing, it will be shown how the microstrip transmission line "sensor" can help meet current testing shortcomings and increase efficiency in characterizing unknown aqueous solutions.

3.1. Detecting Dielectric Properties and Polarizations

Tissues, cells, and biomolecules are dielectric materials that act as electrical insulators during external electric field exposure. Unlike a conductive material that passes current through during electrical field exposure, dielectric materials store charge internally by becoming polarized. The effect of an externally applied electric field on dielectric material can be observed by measuring dielectric properties. Measuring the dielectric properties of biologic materials and biomaterials have been of interest for decades [47], [48], [49], [50], [51], [52], [53], [54], with most recent interest focusing on advancements in power transfer and wireless powering via EM waves [55].

Dielectric property measurements include permittivity, conductivity, and permeability of a material under test (MUT) [56]. Permittivity measurements of various biomaterials give a “unique signature” after being exposed to EM waves and are sensed using biosensors [50]. Dielectric permittivity is represented in a complex form where the real part represents the relaxations and resonances, i.e., how a material can store, transmit, or reflect the energy from an electromagnetic field. Meanwhile, the imaginary part represents the electromagnetic energy absorbed by the material [6]. Therefore, the measurement of a material’s dielectric properties can change based on a broad spectrum of varying factors, including but not limited to temperature, orientation, molecular structure, pressure, fat content, and geometry of the specific material [57].

According to the review paper [55], there needs to be more in-vivo tissue studies regarding the interaction between EM waves and the various tissues found within the human body. [55] also points out the heavy reliance on empirical modeling to predict permittivity and conductivity values. A foundational collection of papers that gathered measurements of the permittivity of various aqueous liquids and materials was initially conducted by G. and S. Gabriel et al. [47], [49]. [44]– [46] states that although these models give estimates of tissue dielectric values, models should consider the variability of each person in the study. The variability of dielectric properties from tissue measurements is due to the variation in each person’s tissue, whether in shape, thickness, fat content, water storage in cells, and genetic variation. All these factors from inhomogeneous cellular structure alter the conductivity and permittivity measurements [61], [62].

Permittivity measurements can also be modeled on the cellular level to describe changes in a cell’s membrane potential, cell membrane’s thickness, concentration, and/or mobility of

cells as seen in graphics plotting a dielectric permittivity vs frequency response, described in [63] and shown in Figure 7 above.

Dielectric permittivity measurements show a correlation between the frequency of the propagated EM wave and the amount of water contained within the material [64], [65], [66], [67]. EM energy is increasingly absorbed by water molecules as the frequency of the EM wave increases, which together leads to a decreased numerical value in the dielectric permittivity measurement [64], [66], [68], [69]. Therefore, consideration should be given when testing biomaterials whose primary composition is water since water molecules readily absorb EM energy, which potentially may cover up the changes in permittivity due to the remaining smaller portion of the MUT that is not water [63].

When measuring the dielectric properties of various biomolecules, it is important to know how or if the biomolecule breaks down into smaller “building blocks,” such as amino acids or nucleonic acids. These building blocks may influence the overall response of the biomolecule to exposure to EM waves. Since biomolecules are often large and have a much greater molecular density than water, it is notable that the observed response after EM wave exposure may have identifying characteristics. One example is the presence of the amino acid tryptophan within a biomolecule [67] where specific irradiation frequencies have been observed to increase interaction. This may include levels of absorption, stored energy, dissipated heat, reflection/transmission of the EM wave. Meanwhile, other characteristics of biomolecules such as charged side chain groups, secondary and tertiary structures [70], already present dipole moments, size of molecules [71], and the presence of disulfide bonds [72], [73], [74], [75] will also affect permittivity measurements.

3.2. Biosensor Types

Biosensors are devices or instruments used to detect and convert a biological signal into a signal that can be measured, usually electrical or chemical. As mentioned, biosensors can be split into Optical or EM wave types, including RF, mmW, MW, and THz biosensors. Biosensors are often used commercially and in healthcare settings to determine concentrations of specific biomolecules within the human body [19], [22], [29]. Table 1 outlines a breakdown of biosensor characterization based on operating frequency. Biosensor design can be accounted for if a MUT is desired to be tested in a specific frequency range.

Table 1. Biosensor Types and Operating Frequency Ranges.

Biosensor Type	Approximate Frequency Range
Radiofrequency (RF) biosensors	100 MHz – 3 GHz
Microwave (MW) biosensors	3 GHz – 30 GHz
Millimeter wave (mmW) biosensors	30 GHz – 0.1 THz
Terahertz biosensors	0.1 THz – 100s THz
Optical biosensors	100s THz – 1000s THz source

Note: Listed above are the types of biosensors that can be designed and the operating frequency range of each type. If a specific frequency or range of frequencies are desired, this can help narrow the design considerations used [20].

3.2.1. Optical Biosensors

Optical biosensors are designed to detect changes in biomaterials by measuring the amount of backscattered light emitted off the biomaterial after light exposure. Two main categories of optical biosensors include visible light and infrared sensors. Typical optical properties measured by these sensors include absorption, reflectance, emission, or change in the interference pattern of a MUT [22]. Optical sensors can be used to measure a change in the

chemical potential of a MUT after EM energy exposure. Studies found evidence to conclude that absorbed EM energy is stored within biomaterials as chemical energy instead of being absorbed and turned into thermal energy [76], [77], [78], [79].

3.2.2. Electromagnetic (EM) Wave Biosensors

EM wave biosensors are categorized based on the frequency they are designed to operate in and use capacitive sensing or changes in permittivity measurements to determine concentrations of various materials under test. The operating frequency helps to determine what types of polarizations and relaxations/resonances may be happening during EM field exposure. Subgroups of EM biosensors are based on classification type, operating frequency, and detection methodology, extensively discussed in review papers [20], [22], [80], [81], [82]. The review found in [20] states that EM wave biosensors are attractive in their design because they are minimally invasive, label-free, and cost-effective.

3.2.3. Biosensing in Terahertz Frequencies

Of all EM wave biosensors, ones operating in the THz frequency range have been published frequently. A 2023 review outlining THz biosensors, too numerous to described here, with designs including numerous material choices, performance specifications, and choices for biological detection [83]. Since some biomolecules may have a resonant frequency occurring in THz frequency region, it is understandable why there is a great interest to study this interaction [84], [85], [86]. Various effects from exposure to THz radiation have been reported, including stimulating plant growth [87], [88] affecting the lifespan of insects [89], altering behavior in mice and rats [90], [91], [92], and increasing cellular stresses, such as mitochondrial stress, apoptosis, tissue coagulation, organelle function disruption, protein modification, changes in membrane permeability, and DNA damage [93]. These interactions include the spectrum of

biomaterials from whole tissues and cells, biomolecules such as DNA, sugars, and proteins, and down to ions in salt and water. It should be noted that these findings can be seen as a positive effect, if trying to eradicate biological materials such as harmful microbial cells [94] or a drawback if causing unhealthy cellular or molecular behavior [95], [96].

Of all EM wave biosensors, ones operating in the THz frequency range have been published frequently. A 2023 review has tables outlining designs of THz biosensors, too numerous to be described here, categorized by performance, material type and desired biological sample detection [83]. Since some biomolecules may have a resonant frequency occurring in the THz frequency region, it is understandable why there is a great interest to study this interaction [84], [85], [86]. Various effects from exposure to THz radiation have been reported, including stimulating plant growth [87], [88] affecting the lifespan of insects [89], altering behavior in mice and rats [90], [91], [92], and increasing cellular stresses, such as mitochondrial stress, apoptosis, tissue coagulation, organelle function disruption, protein modification, changes in membrane permeability, and DNA damage [93]. These interactions include the spectrum of biomaterials from whole tissues and cells, biomolecules such as DNA, sugars, and proteins, and down to ions in salt and water. It should be noted that these findings can be seen as a positive effect, if trying to eradicate biological materials such as harmful microbial cells [94] or a drawback if causing unhealthy cellular or molecular behavior [95], [96].

3.2.4. Biosensing in Microwave (MW) Frequencies

Biosensors operating in the MW frequency range popularly include sensing techniques such as patch antenna, planar microstrip transmission lines, microfluidic designs, and ring resonators. Recent designs integrating both microfluidic channel and ring resonator allow for loading samples and measuring S_{21} parameters for monitoring bacterial growth [97], detecting

solvents such as methanol and ethanol [98] and L-Lysine detection [99]. Another design approach used SRRs on a printed circuit board (PCB) to monitor blood glucose levels non-invasively [100]. Finally, a biosensor designs implementing planar microstrip transmission lines include a double SRR detecting hybridization of DNA molecules adhered to the surface [35] and microfluidic planar resonator sensing water/ethanol mixtures [101], both collecting S_{21} measurements.

3.2.5. Biosensing in Millimeter Wave (mmW) Frequencies

Experiments utilizing millimeter (mmW) wave exposure have shown effects on varying biological systems. This is a cause for concern for the current roll-out of 5G networks, according to a 2021 article by Martin Pall in the Reviews on Environmental Health Journal [102] and 6G networks [95]. Multiple biological organisms have been investigated, ranging from the subcellular level to the whole-body level. Specific experiments include testing done on bacteria and their function [86], [103], [104], fruit flies [105] and mice [106], [107], [108], neurons and ganglia [109], membrane hyperpolarization and interneuron firing [110], and permeability of cell membranes [111], [112]. These experiments led to varying results: some showed an increase in membrane permeability [111], [112] while others showed no effect [113], [114], and therefore the many findings may be viewed as inconclusive.

Water molecules, being an easily accessible testing material, have been tested in the mmW range and found to be a strong absorber of this wavelength of radiation [6]. Therefore, if another biomolecule wanted to be tested in this range, consideration should be taken to account for the strong energy absorption from the water molecules present.

In their 2017 review paper, Romanenko, S., Begley, R., Harvey, A., Hool, L., and Wallace V. call for further research to investigate how EM waves of all frequency ranges interact

with living organisms [6]. This and other recent review papers note causes for increased study and potential concern for adverse health risks influenced by EM wave exposure, such as an increase in the Blood Brain Barrier (BBB) permeability, alterations in intracellular calcium homeostasis, and effects on DNA-RNA associated systems all occurring after mmW exposure. Breaking it down, review papers [115], [116], [117] discuss in vitro and in-vivo experimentation of cells and how EM energy absorption may be modeled within the human body/skin. Meanwhile, reviews [118], [119] discussed specific frequencies and SAR levels that expressed various genes and heat-shock proteins.

3.2.6. Biosensors Operating in Radiofrequencies

Radiofrequency (RF) biosensors have high potential for application and use within the healthcare industry, specifically as a point-of-care testing (POCT) device because of the ability to take non-ionizing, non-invasive measurements [22] with a large amount of designs currently focusing on glucose monitoring. For example, a commercially available RF biosensor, Gluowise (UK), requires only a drop of blood to determine the concentration of glucose in the blood [120], [121]. A 2021 review highlighted numerous glucose monitoring RF biosensing designs collecting real-time, continuous measurements with design techniques including microfluidic subsystems, antennas (microstrip, resonators, patch, etc.), and substrate integrated waveguides (SIW), to generalize [122].

Key design features of this dissertation's proposed RF biosensor are the integration of a coplanar microstrip transmission line able to measure microliter sized MUT. Current devices cover a wide latitude, with a few highlighted below. A narrowband device features a rectangular slot antenna with a SIW used to characterize liquid solutions based on S_{11} measurements around 10 GHz [123]. In contrast, a broadband (400 MHz – 35 GHz) coplanar transmission line

biosensor with microfluidic channels measures complex permittivity [124]. A third such design features a cavity resonator, also with a SIW, operating a narrowband at 1.57-2.19 GHz to measure S_{21} values [125].

RF biosensors can be designed in numerous ways depending on the constraints of the MUT, both in physical design and sensing technique. The proposed RF biosensor design of this Ph.D. dissertation includes sensing techniques: label-free, minimally invasive, indirect sensing, and ex-vivo, which are discussed in the following section.

3.3. Sensors Measurement Detection Techniques and Design Considerations

In the previous sections, the broader design considerations of operating frequency and experimental setup were investigated. In the following section, finer design details for biosensors will be explored including experiment type, detection methods, and measurement techniques.

3.3.1. In-vivo versus Ex-vivo Experimentation

When considering the difference between the design requirements of in-vivo versus ex-vivo experimentation. The differentiation between the two is the ability to take measurements inside a test system or patient sometimes without extracting the sample (in-vivo) or extracting the sample from a system or patient and then performing tests and measurements on that sample (i.e., blood/plasma draw).

According to the NIH in article [126], in-vivo biosensing is a complex yet highly impactful tool area of study. Whether the goal of the device is to track drug delivery, glucose levels, or other various human functions, the fact that these measurements and diagnostics can be performed, often in real-time, without too many needle pricks is amazing. Some general in-vivo biosensing devices would include, but are not limited to, heart rate detector, sleep monitors, O_2 level saturation, CO_2 level saturation, personalized or handheld ultrasound, X-ray, or EM

imaging, machines. In contrast, ex-vivo measurement devices need the sample inside or on the surface of the device for proper sensing and/or detection (i.e., blood glucose monitors using finger-prick, influenza swabs, electrode/microfluidic devices/systems, etc.) [22].

3.3.2. Label versus Label-free Experimentation

Another popular technique used for detecting changes in dielectric properties of biologics such as biomolecules under test is to attach a label, commonly a biomarker, to a protein, gene, segment of DNA, etc., of interest. These attached biomarkers detect and then show whether a change has occurred to the biomolecule of interest during experimentation. Some examples of label detection results may be shown as an expressed gene, a specific fluorescent reading/response, or shape detection [22].

In contrast, label-free detection does not require a biomarker to be attached to the sample under test for detection of the desired response. A common example of label-free detection in electrical engineering is impedance sensing. This is where impedance or resistance measurements may be taken to analyze and conclude how a biomolecule's characteristics may be changing while under test, for example while exposed to an external electric or magnetic field. Typically, systems used to make these label-free measurements include probes, microfluidic devices, or antenna-based devices. These devices take measurements in real-time, which is beneficial in a laboratory setting to determine if the experimental test results appear valid upon visual inspection or if the test needs to be re-run. Also, designing devices that do not need labels cut down on the expense and time required to buy, safely store, and attach the labels to the biomolecule(s) of interest. Note that the limitation of label-free detection and biosensors is the need for an elevated level of sensitivity in measurement collection. This is because, unlike

labeled detection, not all interactions may be apparent based on read-out methods i.e., changes in measured impedance, voltage, permittivity, etc. [22].

3.3.3. Direct versus Indirect Measurement

A third design consideration is how the measurement can or should be taken by the biosensor. If choosing a direct measurement, the material under test will be directly exposed to EM energy. Meanwhile, an indirect measurement will not directly expose the material under test to EM waves but instead will use a method such as microfluidic channels with bioreceptors to obtain the change in permittivity measurements [22].

3.3.4. Detection and Measurement Techniques

The final choice for biosensor design is how exactly the biosensor will take measurements. There are numerous methods to obtain measurements depending on what is available and affordable, and the specifications of the machines/equipment used to power the biosensing device. Typical RF biosensor measurement choices may include, but are not limited to, the use of fluorescence, including specific frequency/color outputs, concentration levels i.e., of specific biomolecules, impedance, voltage, current, permittivity, and/or permeability, and scattering parameter values.

3.4. “The Gap” - Current Needs for Improvement for EM Wave Biosensors

Current aspects of biosensor design which can be improved upon include cost-effectiveness, miniaturization of on-board chips, single-use (disposable) biosensors to increase sterility of test and reduce contamination (improving the reliability of results) and increasing RF biosensor performance relating to sensitivity and repeatability of measurements [6], [20], [22], [29], [127]. Another pathway for growth within the area of RF biosensors is the opportunity to create a commercialized product that is easily portable, has increased sensitivity of test

measurements, and has ease of integration with common household electronic devices compared to current in-lab-only RF biosensors.

Collectively, current biosensing devices have many pathways for increased efficacy. Whether this is through labeling or tagging biomarkers on biomaterials that are going to be subject to testing or the cost of obtaining and safely storing expensive lab supplies and preparatory materials. Aiming to decrease the expense, by reducing lab supplies needed to take experimental tests, using testing equipment that can run multiple tests on a single sample, or using label-free testing methods are design considerations used to cut costs. Decreasing the sample size needed to perform a patient care or experimental test while maintaining the integrity of the results holds the potential for creating a substantial impact on any diagnostic device.

The technique of gathering test and experimental data also lends itself to improvement by design and integration of the equipment/device setup. With current technology, creating a real-time readout of results should be incorporated as often as possible. Also, creating a device that can measure/scan/operate at various frequencies, instead of one specific, targeted, or narrow band of frequency values would reduce the cost of redesigning the device if other frequencies of interest should come about. Also, being limited to test for the presence/absence of one specific compound/biomolecule increases the cost of time to run the test, samples/solutions needed, and expense. If increasing the sensitivity of a sensing device can reduce the cost, this alone would benefit researchers and diagnostic medicine alike. Not to mention, any sensing device with precise and sensitive measurements would also reduce the possibility of introducing testing errors and therefore increase the certainty and validity of all experimental and test results.

3.4.1. Proposed RF Biosensor Meeting “The Gap”

The RF biosensor proposed in this work strives to meet the needs for improvement of previous biosensor designs, specifically by reducing the cost of production, reducing lab supplies/equipment needed, and increasing the efficiency of the sensing process by increasing sensitivity, offering a multi-frequency device, and real-time results.

The RF biosensor described in detail in the following chapter can be produced inexpensively through current milling machine practices and future design iterations can be produced using 3D printing technology. This would provide a pathway to produce commercially available, inexpensive, and disposable, single-use sensors. Other design considerations used to reduce expense are: 1) Designing for label-free detection, which saves cost on lab preparation by eliminating the time and money needed for attaching expensive label-detecting materials and eliminates the risk of sample contamination, 2) Designing a broadband RF biosensor, so frequencies ranging from RF to MW can be tested, or a the biosensor can be tuned to a specific frequency, and 3) Not requiring the biosensor to be sample specific (i.e., no affinity binding required) meaning a variety of liquid or aqueous solutions can be loaded into the biosensor.

Regarding increasing testing efficacy, the proposed RF biosensor design is intended to require a microliter (μL) sample size. Although this design requires more sampling volume than current devices found commercially and in laboratories, it remains a small sample size. That, along with the reduction in experimental equipment setup size and display of real-time results, is included to increase testing efficiency and sensitivity.

4. METHODOLOGY¹

There are two desired outcomes of this work 1) to develop an RF biosensor that can measure permittivity changes in microliter aqueous samples after exposure to non-ionizing, electromagnetic waves in the radio frequency region and 2) after designing the RF biosensor use lambda DNA as the aqueous sample and measure its change in scattering parameters and compare to previous sensing methods (i.e. Master's work with horn-to-horn antenna exposure [27]).

The following chapter will discuss in detail the methodology used to meet the desired outcomes of this work. The first sections will explain the design of the RF biosensor itself including simulations and theoretical design which were published in 2021 RMBS Conference proceedings [128]. Next, an overview of the following methodology and corresponding results were published in MDPI's Biosensor journal [129]. Experimentation using the novel RF biosensor and measurement gathering will be described. Finally, the data collection and analysis process used to verify the RF biosensor sensing results will be explained. For detailed standard operating procedures, sample data used, and MATLAB code used see the appendices.

¹ The author was involved in this dissertation work every step of the way. The gap for this dissertation was originally realized by the author throughout the completion of her Master's thesis experimentation and confirmed by other's work discovered in a deep literature review. The author collaborated on the conceptualization of the RF biosensor prototype, fabrication of the physical biosensor, and development of experimental methodology. Other aspects of collaboration included designing and defining parameters for the RF biosensor's validation, performing a formal analysis of all resulting data, reviewing and editing journal publication drafts, and acquiring funds and lab space for the experimental testing. Creating simulation designs, developing MATLAB code for statistical analysis, data curation, MUT preparation, and both journal publication drafts were solely contributed by the author.

4.1. Proposed RF Biosensor Design

A rendering of the proposed biosensor design, shown in Figure 17., shows a microstrip transmission line with a microliter well, placed directly off one side of the transmission line. This microliter well will hold aqueous solutions under test and measure scattering parameter data during exposure to radiofrequency energy to observe if interactions take place at any frequencies of interest. Therefore, it is important to verify that both the E- and H-field lines cross through the entirety of the microliter well. The proposed RF biosensor will be milled on Rogers TMM4 material, which has a relative permittivity, ϵ_r , of 4.7 and copper cladding located on the ground plane and microstrip transmission line.

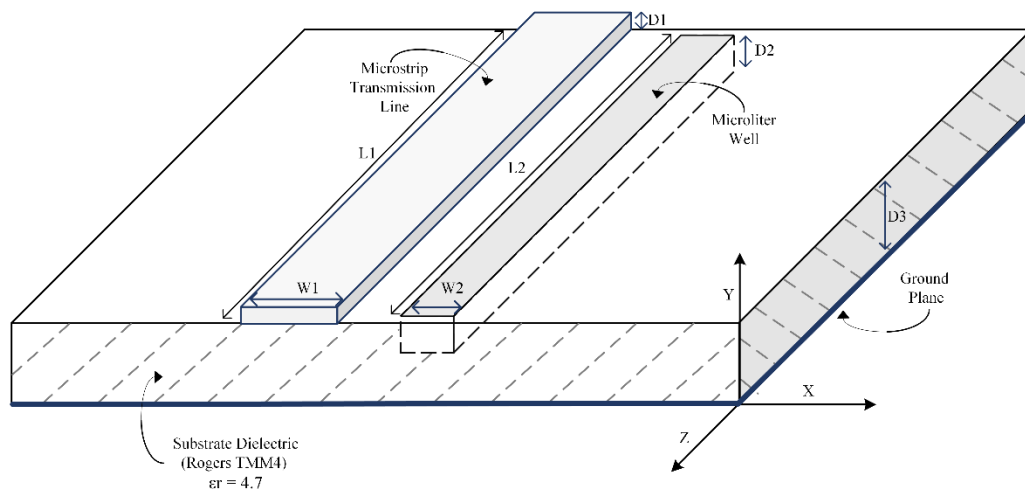


Figure 17. A Rendering of the Proposed RF Biosensor.

Note: A rendering of the proposed RF biosensor, which will be a 2-port system, operating on a broadband frequency spectrum, 1.0 - 17.0 GHz and milled on Rogers TMM4 material. An adjacent microliter well will hold up to 15 μ L of an aqueous solution for EM energy exposure.

4.1.1. 2D Simulations in Advanced Design System (ADS)

Using a 2D circuit simulation software called Advanced Design System, ADS, a microstrip transmission line was designed and simulated to fit desired requirements namely having a 50-ohm line impedance and being small in dimension. ADS simulations were used to simulate scattering (S) parameters in complex number form ($R + jX$).

To ensure a 50-ohm microstrip transmission line (matched load) was designed, both ADS' LineCalc and an online microstrip impedance calculator were used. The dimensions created a 50-ohm line impedance with the transmission line running down the center of the rectangular device while saving a short width, to create space for an etched well, to hold liquid/aqueous materials under test, off one side of the transmission line. The target volume of the etched well was in the range of microliters, μL . The chosen microstrip transmission line dimensions to fit these requirements are outlined below and reported in the *Pearson, et. al 2021* paper [128].

Table 2. Resulting Dimension Calculations for the Proposed RF Biosensor Design.

Trace Thickness	T	0.0175 mm
Substrate Height	H	1.0 mm
Trace Width	W	1.7965 mm
Substrate Dielectric (Rogers TMM4)	ϵ_r	4.7 (unitless)
Impedance	Z	49.9 Ω (ohms)
Well Dimensions	l x h x w	39.0 x 0.25 x 1.5 mm
Well Volume	V	14.625 μL

After the dimensions were created in ADS, two ports were attached to either side of the copper transmission line to create a 2-port wave. Next, a broadband frequency sweep was created spanning from 1.0 17.0 GHz with a step size of 0.01 GHz for 1601 points. The ADS simulation results are shown in Figure 18 with a step-by-step guide to build this design in Appendix A.

Both 50- and 75-ohm simulations were created in ADS (75 ohms determined with width = 0.8160mm. Commonly 75-ohm coaxial cables are used in experimentation, so both were simulated to compare the initial results of both cases. 50-ohm coaxial cables were used in the experimental setup so the focus will be on these simulated results.

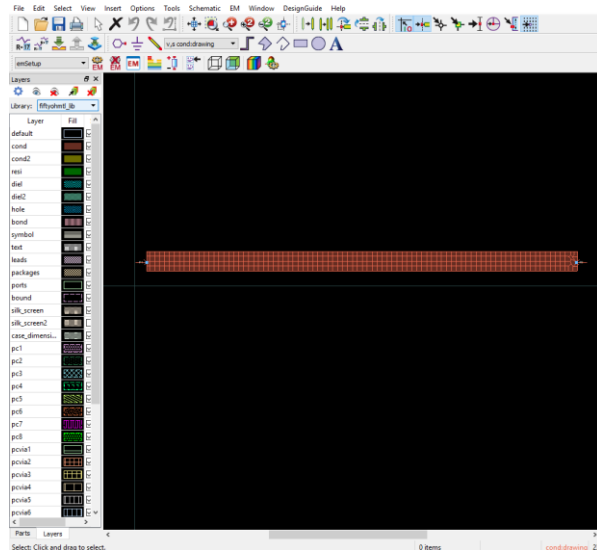


Figure 18. The 50-ohm Copper Transmission Line with Simulation Mapping Lines.

4.2. 3D Ansys HFSS Simulation Design

After the dimensions were calculated, designed, and simulated in ADS, a 2D circuit simulation software, the microstrip transmission line was inputted into HFSS, a 3D Multiphysics simulation software. The 50-ohm microstrip transmission line was designed and simulated to obtain complex ($R + jX$) S-parameters. These S-parameters were then exported as touchstone files (.s2p) and imported into MATLAB for comparison versus ADS simulations to establish an agreement between the two models.

After simulating the initial HFSS designs, an SMA connector was introduced into the microstrip transmission line design. The SMA connector is what, in lab experimentation, is soldered onto the milled copper ground plane and copper microstrip with the other end connecting to the coaxial cables attached to the VNA. The SMAs used in these HFSS

simulations were created and verified using YouTube tutorial videos from the Tensorbundle channel.

4.3. Production of the RF Biosensor

After the successful completion of HFSS and ADS simulations the next step was to mill out the finalized RF biosensor design. Then experimental verification of the design took place including sensitivity, reproducibility, and repeatability of RF biosensor measurements.

4.3.1. Simulation File Map, Material Used, and Milling Machine Specifications

The microstrip transmission line sensor HFSS simulation files were exported in Gerber files acceptable for milling. An LPKF ProtoMat S63 was used to mill the sensor. Rogers TMM4 material was used to create a 50Ω only microstrip transmission line, i.e., without the RF biosensor without the addition of the microliter well, and the RF biosensor. After milling was complete, 3mm RF SMA connectors were soldered on either end of copper transmission lines of both the 50Ω microstrip transmission line and the RF biosensor.

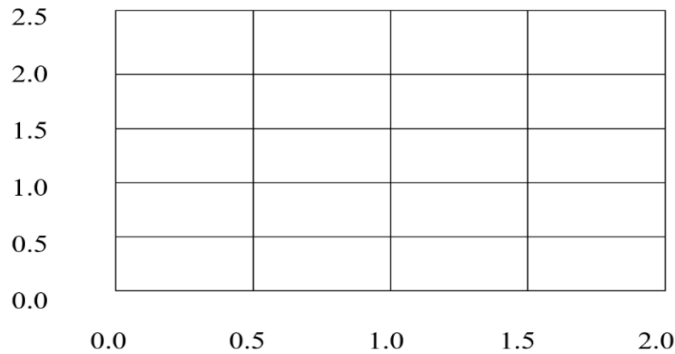


Figure 19. The LPKF ProtoMat Milling Accuracy/Repeatability Layout.

4.3.2. LPKF ProtoMat Milling Machine Accuracy and Repeatability

The LPKF ProtoMat S63 machine specifications sheet found in [130] discuss the resolution and precision specifications as the following:

- From the home position, the drill bit can travel to any 0.5um coordinate spot on the mat (example shown below).
- **Resolution (X/Y)** defines the relative precision of the machining process. i.e., The drill bit can move up/down 0.0005mm (0.5µm) increments of space on a mat, shown in Figure 19. If asked to move somewhere between these increments the machine will round up or down to the nearest available increment.

4.3.3. Milling the RF Biosensor

All milling was done using the LPKF ProtoMat from a Gerber file extracted from the final HFSS simulation design. The ProtoMat was programmed to use the most precise drilling bits during the milling process. After selecting the drilling bits to maximize milling precision and calibration of the drill bit location/exchange was completed. First, a microstrip transmission line, without a drilled-out well, following the exact dimensions of the RF biosensor was also created and used as a control to verify the procedure and set up for experimental testing purposes. Then the RF biosensor was milled with the well etched out using the LPKF ProtoMat as well, using the drilling function of the machine. When the milling was complete, canned air was used to rid the microstrip transmission line and the RF biosensor of any ceramic dust from the fabrication process. Then the biosensor was rinsed with water and cleaned with 70% ethanol spray before any testing began.

4.4. Testing the Microliter Well's Absorbency

A water absorbency test was conducted on the RF biosensor to determine if the microliter well, which is made of Rogers TMM4's ceramic portion, would absorb any aqueous MUT being held within the well. This water absorbency would influence the total volume located within the well which in turn would affect the EM interaction with the MUT.



(a)

(b)

Figure 20. The dry weight (8.6096 grams) and wet weight (8.6493 grams) of RF biosensor during porosity testing.

Note: (a): The weight of the RF biosensor before submersion, and (b) the weight of the RF biosensor after two hours of submersion in room temperature deionized water.

To test this, the RF biosensor was first weighed to collect a dry weight using a Shimadzu AUV220D Semi-Micro Balance. After the balance was internally calibrated to zero grams, the resulting dry weight recorded was 8.6096 grams as seen in Figure 20a.

Next the biosensor was immersed in room temperature ($\sim 25^{\circ}\text{C}$) deionized water for two hours. Immediately after immersion, the biosensor was reweighed to collect a wet weight, which was recorded as 8.6493 grams, as seen in Figure 20b. The net weight difference was 0.0397 gram. Therefore, it was concluded that a significant amount of MUT would not be absorbed by the ceramic material during an experimental sweep lasting milliseconds, and absorbency of the ceramic would not affect the resulting interaction signal between the MUT and EM energy.

4.5. Testing the Substrate Heating During Experimentation

To test if the MUT located inside the well was experiencing any heating effects due to the ceramic substrate while in use, a Digital 2-Channel K-Type Handheld Thermocouple was secured to both the top and bottom of the RF biosensor. Temperature ($^{\circ}\text{C}$) was measured and

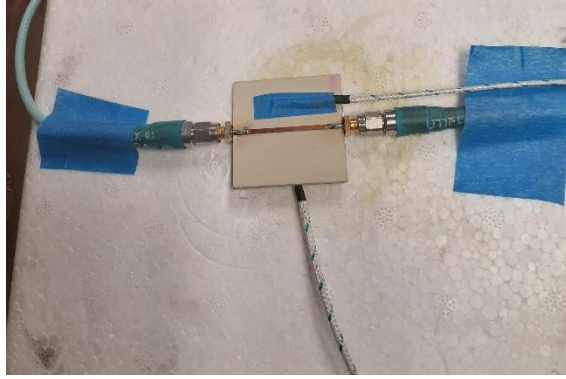


Figure 21. Thermocouple Experimental Setup.

Note: The thermocouple attached to the ceramic portion (top) of the RF biosensor is denoted T1 while the one attached to the ground plane (bottom) is T2.

recorded as the Continuous Sweep function was run for 15 minutes with the microliter well left empty. For reference T1 is the thermocouple attached to the top of the biosensor using Painter's tape and T2 is attached to the bottom as seen in Figure 21. The results are displayed in Table 3 below.

Table 3. Thermocouple Study: 15 Minute Continuous Sweep Leaving the Microliter Well Empty.

Time (minutes)	0	1	2	3	4	5	6	7	8	9
T1 (°C)	23.5	23.4	23.3	23.3	23.2	23.2	23.2	23.2	23.1	23.1
T2 (°C)	23.6	23.5	23.3	23.3	23.2	23.2	23.2	23.2	23.1	23.1
Time cont. (minutes)	10	11	12	13	14	15				
T1 (°C)	23.1	23.1	23.0	23.0	23.0	23.0				
T2 (°C)	23.1	23.1	23.0	23.0	23.0	23.0				

A second thermocouple study was performed using deionized water. At intervals of 30 seconds, for a total of four minutes, temperatures T1 and T2 were recorded. Again, T1 was located on the top of the RF biosensor while T2 was located at the bottom. Four minutes was the set time chosen because at the 5-minute mark signs of evaporation inside the microliter well occurred. This experimentation was repeated for two sets as shown in Table 4.

Overall, the thermocouple experimental data suggests that no heating of the substrate or ground plane is taking place during measurements whether the microliter well is loaded or not.

Table 4. Thermocouple Study: 4 Minute Continuous Sweep with Microliter Well Loaded with Deionized Water.

Deionized Water at 25°C	Time (minutes)	0	0.5	1	1.5	2	2.5	3	3.5	4
Set 1	T1 (°C)	23.0	23.0	23.0	22.9	22.8	22.8	22.8	22.7	22.7
	T2 (°C)	23.0	22.9	22.8	22.7	22.6	22.6	22.6	22.5	22.5
Set 2	T1 (°C)	23.0	22.9	22.8	22.7	22.7	22.7	22.6	22.6	22.6
	T2 (°C)	22.9	22.9	22.8	22.6	22.6	22.6	22.5	22.5	22.5

4.6. RF Biosensor Functionality Verification

The experimental procedures outlined below, in Figure 22, give evidence for the functionality and repeatability of the milled RF biosensor. First, a Full 2-Port Calibration was performed every time experimentation took place. Next, the 50Ω microstrip transmission line antenna was connected to a VNA to ensure the design is actually a 50ohm matched load as expected. After the 50Ω transmission line antenna was verified as a matched load, the RF biosensor was connected to the VNA where microliter volumes of aqueous solutions such as deionized and distilled water, salt water, Tris-EDTA buffer, and lambda DNA, were loaded into the microliter well and S-parameters were measured. Various experimental protocols were conducted to verify the repeatability, sensitivity, and reproducibility of the measurements, which will be discussed in detail below. Other environmental factors such as evaporation of the aqueous solution during testing, absorption of the aqueous solution into the ceramic material of the RF biosensor, and heating of the RF biosensor were observed and measured.

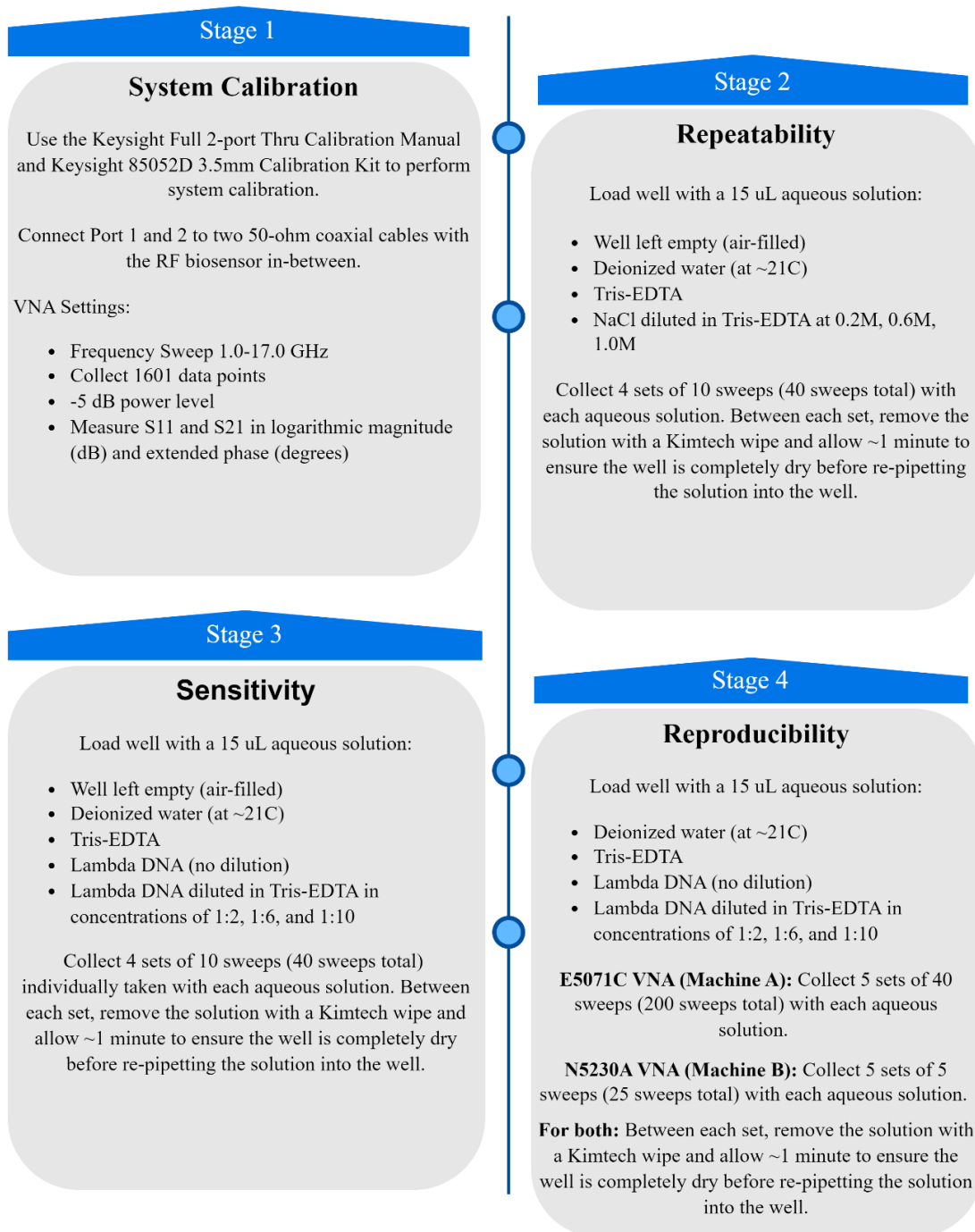


Figure 22. Outline of Stages 1- 4 of Experimental Verification of the Proposed RF Biosensor.

4.6.1. Experimental Stage 1: Full 2-Port Calibration

A Keysight Full 2-Port Calibration Manual and a Keysight 85052D 3.5mm Calibration Kit will be used to calibrate the experimental setup, shown in Figure 23, consisting of an E5071C VNA, two 50-ohm coaxial cables, which were performed every time experimentation took place. This Full 2-Port Calibration will ensure to minimize of the amount of experimental setup noise measured by the system. The VNA settings should be set as:

- Frequency Sweep: 1.0-17.0 GHz
- Data Points: 1601
- Input Power Level: -5 dB
- Measure S_{11} and S_{21} in logarithmic magnitude (dB) and extended phase (degrees)

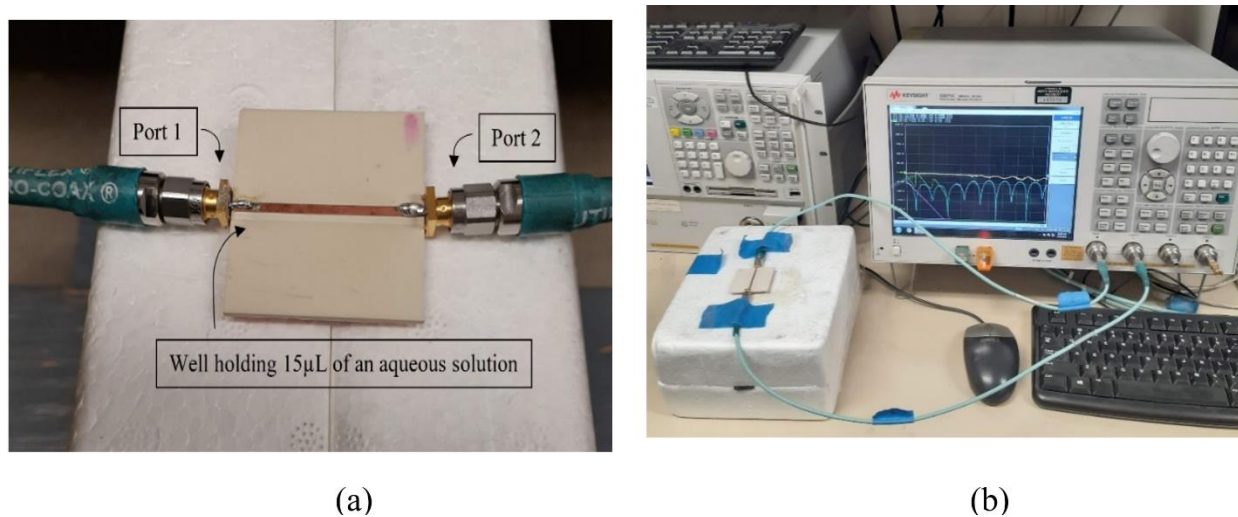


Figure 23. RF Biosensor Connected to Experimental Setup.

Note: (a): The RF biosensor, connected to ports 1 and 2 of the VNA. Also highlighted is the location of the microliter well, and (b) A full view of the VNA/RF biosensor experimental setup.

4.6.2. Experimental Stage 2: Repeatability of Measurements

A study was conducted to determine the ability of the RF biosensor to collect repeatable measurements. After the Full 2-Port Calibration, the RF biosensor was connected between the two 50ohm coaxial cables. Then using a micropipette, 15 μL of aqueous solutions of deionized

water (at room temperature, $\sim 21^{\circ}\text{C}$), Tris-EDTA buffer, NaCl diluted in Tris-EDTA at concentration a of 0.2M, 0.6M, and 1.0M, and the well left empty (air-filled) were placed in the well. Then 4 sets of 10 sweeps (40 sweeps total) were measured for each aqueous solution. To investigate the maximum potential for introduced error, the solution inside the well was replaced and re-pipetted between each set. A Kimtech wipe was used to remove the solution being tested and the well was allowed ~ 1 minute to completely dry before reloading the well.

4.6.3. Experimental Stage 3: Sensitivity of Measurements

Another important aspect of the RF biosensor design was the need to capture measurements that were sensitive, meaning there is a low error calculated between the population mean and individual sweep measurements. To determine the sensitivity of the RF biosensor, the absolute average error, a range from minimum to maximum standard error, and the relative standard error range were calculated using empty well (air-filled) and deionized water-filled well measurements. These sensitivity values were analyzed from the data collected during the repeatability study mentioned above. To calculate the absolute average error, the standard error was calculated for each of the 40 sweeps individually, and then the absolute value of the mean of the 40 sweeps was found using MATLAB. Next, to calculate the Relative Standard Error, the minimum and maximum standard error values of the 40 sweeps dataset were located using the `min()` and `max()` functions in MATLAB. Since all means are calculated on a point-by-point basis for all 1601 points, the corresponding population mean at the `min()` and `max()` frequency points were found. Finally, the min/max standard error was divided by the mean at the specified frequency point and the resulting value was multiplied by 100 to convert to a percentage. All equations for calculating the above-mentioned error values can be found in section 4.7.3.

4.6.4. Experimental Stage 4: Reproducibility of Measurements

The final stage in the RF biosensor verification experiment was to see if the experimental measurements were reproducible. This was completed by performing the same experimental protocol with two separate VNA machines, one newer and one older. The newer machine referred to in the following as Machine A, is a Keysight E5071C, 4-port, ranging from 300 kHz – 20 GHz, and the older machine, Machine B, is an N5230A, 2-port, ranging from 10 MHz – 20 GHz. Since Machine A could collect consecutive sweeps, it was set up to collect 5 sets of 40 sweeps (200 sweeps total). Machine B, on the other hand, needed buttons manually pressed for each sweep saved, so 5 sets of 5 sweeps (25 sweeps total) were gathered. For both Machines A and B, the well was unloaded with a Kimtech wipe and waited a minute to ensure well dryness before reloading via a micropipette. After gathering all the measurements, the mean and standard error of each aqueous solution were calculated.

4.7. Equipment, Materials Used, and Experimental Setup

Table 5 is a list of equipment including machines, lab supplies, software packages, and the laboratory biological supplies used during experimentation.

4.7.1. Preparation of Aqueous Solution Materials

Aqueous solutions used to load the well of the RF biosensor such as deionized water, distilled water, Tris-EDTA buffer (Promega Corporation, Madison, WI v6231), and solutions of NaCl dissolved in Tris-EDTA of concentrations 0.2M, 0.6M, and 1.0M were stored overnight in the lab space where the experimental measurements were to take place. The goal of this step was to make sure that any aqueous solutions tested were at room temperature (approx. 21°C), reducing the variability of liquid solution temperature.

Table 5. List of Equipment and Materials Used for Experimentation.

Equipment Used	Materials Used
E5071C Vector Network Analyzer, 4-port, ranging from 300 kHz – 20 GHz	Deionized water (kept at room temperature ~21°C)
N5230A Vector Network Analyzer, 2-port, ranging from 10 MHz – 20 GHz	Distilled water (kept at room temperature ~21°C)
50-ohm coaxial cables	
Keysight 85052D 3.5mm Calibration Kit	Tris-EDTA buffer (Promega Corporation, Madison, WI v6231)
Digital Precision Laboratory Scale	
Digital 2-Channel K-Type Handheld Thermocouple	Lambda DNA (New England Bio Labs, Ipswich, MA, N3011L)
Kimtech wipes	70% Ethanol spray
P200 Micropipette & P200 micropipette tips (20-200uL)	NaCl (table salt) which was dissolved in Tris-EDTA buffer
Styrofoam box and painters' tape	
MATLAB, Ansys HFSS, and ADS software packages	

Any aqueous solution containing lambda DNA (New England Bio Labs, Ipswich, MA, N3011L), however, was stored inside a sealed vial and placed in a -20°C biohazard freezer to ensure the biologic would stay viable for experimentation. About 20 minutes before any experimentation on solutions involving lambda DNA took place, the vials were removed from the freezer, allowed to thaw, and gently pipetted to mix the vial's contents.

4.8. Statistical Analysis and Data Manipulation

All data collected during experimentation in the form of S-parameters (dB) and extended phase (degrees) were saved onto a portable flash drive for later analysis. Data collected from the E5071C Vector Network Analyzer (VNA), were saved as .csv files, and data collected from the N5230A Vector Network Analyzer were saved as .s2p (touchstone) files. All experimental data files were imported into MATLAB. The touchstone files were handled by MATLAB's RF Toolbox while the .csv files were manually imported and data for plotting and calculations were extracted.

4.8.1. Scattering Parameter Conversion to Voltage Ratio

Scattering parameters are used to describe complex systems in a simplified way using N-port system calculations. The RF biosensor that was designed and verified in this work will be represented as a two-port system since there is an input and an output port. The mathematical setup for an N-port system is

$$\begin{bmatrix} V_1^- \\ V_2^- \\ \vdots \\ V_N^- \end{bmatrix} = \begin{bmatrix} S_{11} & S_{12} & \cdots & S_{1N} \\ S_{21} & S_{22} & \cdots & S_{2N} \\ \vdots & \vdots & \ddots & \vdots \\ S_{N1} & S_{N2} & \cdots & S_{NN} \end{bmatrix} \begin{bmatrix} V_1^+ \\ V_2^+ \\ \vdots \\ V_N^+ \end{bmatrix} \quad (\text{Equation 4})$$

Solving the above matrices for a two-port system gives four S-parameter measurements that describe the system. The S-parameter measurement being analyzed in the following Results chapter is S_{21} , the reflection coefficient, which is the measurement of the voltage seen at Port 2 concerning the input voltage from Port 1. The S-parameter matrix gives the following voltage information,

$$S = \begin{bmatrix} \frac{V_1^-}{V_1^+} & \frac{V_2^-}{V_1^+} \\ \frac{V_1^-}{V_2^+} & \frac{V_2^-}{V_2^+} \end{bmatrix} \quad (\text{Equation 5})$$

Since all scattering parameter data collected by the VNA were in decibels (dB), which is in a logarithmic scale, it was converted to voltage ratio (unitless of V/V), which is a linear scale for easier comparison of measurements. To convert S_{21} measurements, which are measured in decibels, to voltage ratio values using the following conversion,

$$S_{21}(\text{dB}) = 20 \log \frac{V_2^+}{V_1^-} \quad (\text{Equation 6})$$

Finally, solving to observe the measurements in voltage ratio fraction form gives

$$\frac{V_2^+}{V_1^-} = 10^{\frac{\text{dB}}{20}} \quad (\text{Equation 7})$$

The measured voltage ratio values can help describe how the aqueous solution inside the biosensor well is behaving during electromagnetic energy exposure. Since S_{21} is the experimental value being measured and analyzed, $\left(\frac{V_2^+}{V_1^-}\right)$, is the voltage ratio of interest. The resulting voltage ratio values give information on the behavior of V_2^+ and V_1^- . If the voltage ratio is

$$\left\{ \begin{array}{l} >1, \text{ says } V_2^+ \text{ is larger than } V_1^- \\ <1, \text{ says } V_2^+ \text{ is smaller than } V_1^- \\ =1, \text{ says } V_2^+ \text{ is equal to } V_1^- \end{array} \right\} \quad (\text{Equation 8})$$

4.8.2. MATLAB

MATLAB is crucial for handling the large amount of experimental data collected in this work. Besides importing all simulation and experimental data for plotting and converting experimental S-parameter data into voltage ratio values, MATLAB will be used to calculate the means, standard deviation, and standard error values. This will be done by using MATLAB's built-in commands for statistical analysis. Finally, the specific aim of this work was to see if the RF biosensor could detect any interaction between the aqueous solution in the biosensor's well and the transmitted electromagnetic waves. Since this lambda DNA signal cannot be measured

directly, it will be estimated by calculating the population mean of the lambda DNA suspended in Tris-EDTA buffer subtracted from the population mean of the Tris-EDTA buffer.

4.8.3. Statistical Analysis

The following statistical analysis techniques were used to draw conclusions about the collected experimental data. The mean, standard deviation, and confidence intervals for all experimental data were calculated by the following equations. The mean of the experimental data was calculated by finding,

$$mean = \frac{\Sigma(x)}{n}, \quad (\text{Equation 9})$$

where x is the sum of all data points and n is the size of the population. Next to calculate the standard deviation (SD) of the experimental data set the equation

$$SD = \sqrt{\frac{\Sigma(x_i - mean)^2}{n}} \quad (\text{Equation 10})$$

was used, where x_i is a data point in the dataset and n is the size of the population. Finally, to calculate a confidence envelope (CE) to encompass 99.5% of the gathered RF experimentation data assuming a normal distribution the following was used

$$99.5\% \text{ CE} = mean \pm 3(\text{standard deviation}) \quad (\text{Equation 11})$$

The second portion of statistical analysis was to calculate the error of the experimental measurements. The error calculations below are used to determine standard error (SE), absolute average error (AE), and relative standard error (RSE), will give numerical insight into the sensitivity and reproducibility of the RF biosensors measurements. First, standard error was calculated for each MUT using,

$$SE = \frac{\text{standard deviation}}{\sqrt{n}}, \quad (\text{Equation 12})$$

where n is the size of the dataset population. Next to determine the repeatability of measurements from consecutive loadings of a MUT the absolute average error was found as

$$AE = | \text{mean}(SE \text{ of entire dataset}) | \quad (\text{Equation 13})$$

Finally, the relative standard error is calculated,

$$RSE = \frac{\text{max/min standard error}}{\text{population mean (at identified max/min standard error frequency)}} * 100\% \quad (\text{Equation 14})$$

5. RESULTS

5.1. Advanced Design System (ADS) 50- and 75-Ohm Load 2D Simulation Results

Using ADS's built in feature, LineCalc, and an online transmission line impedance calculator, designs were simulated in ADS to calculate the expected response with a matched (50Ω) and mismatched (75Ω) load. The 50- and 75-ohm loads were chosen for design purposes to simulate the coaxial cables used in the experiments. After building the transmission line within ADS, with a length and width of 40mm, the ideal width for both of these transmission line widths were calculated using LineCalc.

Figure 24 displays the simulated S-parameter results for a 50-ohm transmission line with transmission width of 1.7965mm.

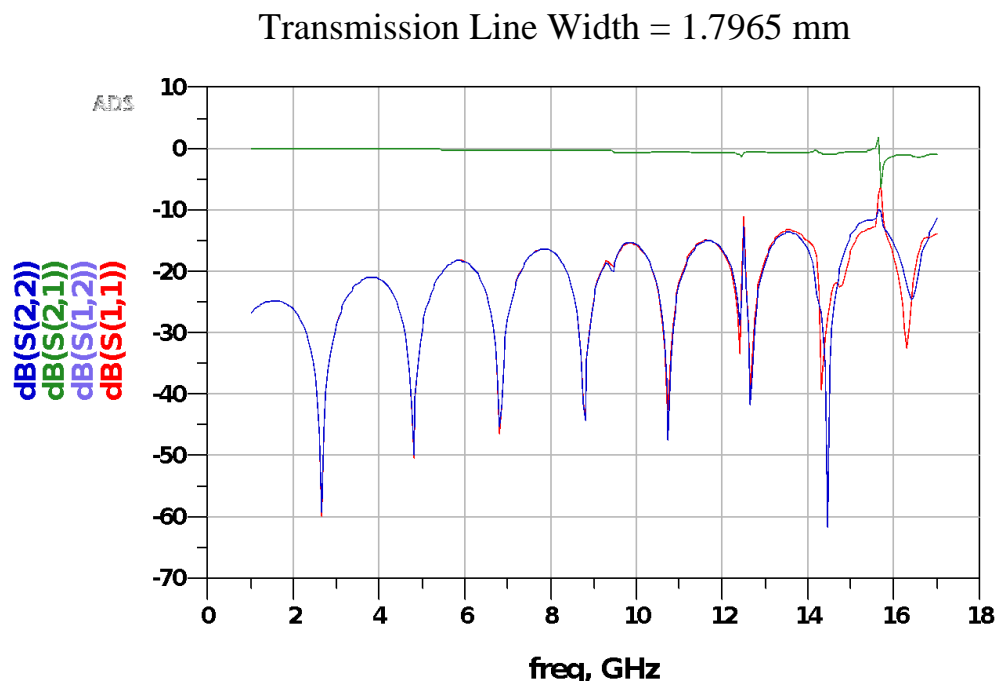


Figure 24. ADS Simulation of 50-ohm Transmission Line of Width 1.7965mm.
Note: S-parameter response of the ADS design for a 50-ohm transmission line throughout 1.0-17.0 GHz sweep.

The ADS scattering parameter results for the 75-ohm transmission line are shown in Figure 25.

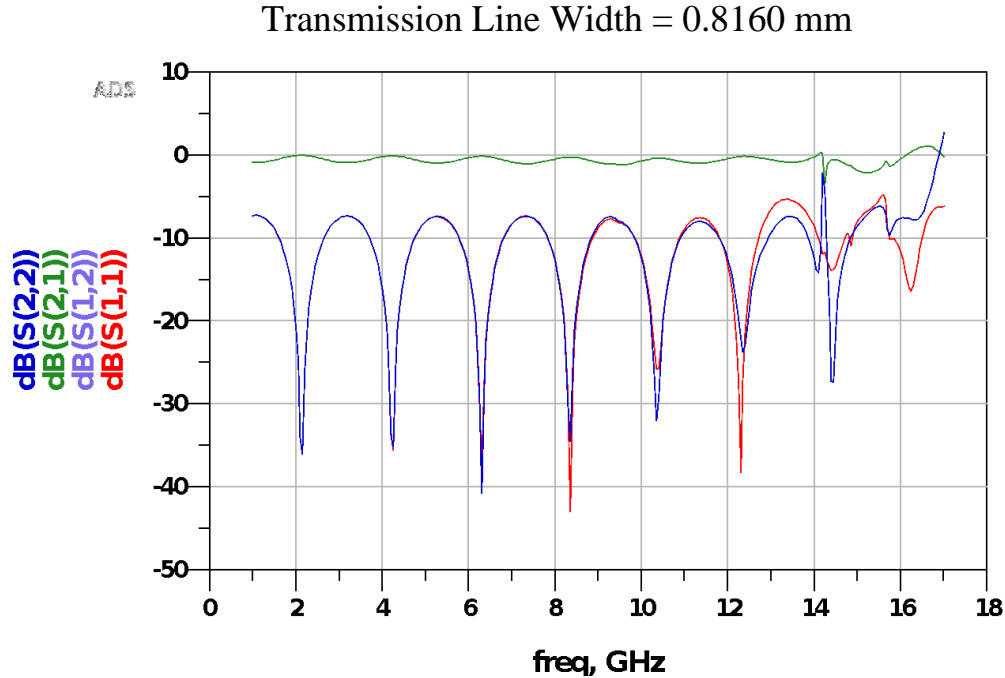


Figure 25. ADS Simulation of 75-ohm Transmission Line of Width 0.8160mm.
 Note: S-parameter response of the ADS design for a 75-ohm transmission line throughout 1.0-17.0 GHz sweep.

Since it was determined to complete the experimental testing would require the use of 50ohm coaxial cables, the 50ohm coaxial cable simulation design was chosen to be used to compare in the subsequent HFSS simulation and experimental testing phases for the design to have a matched load. Therefore, the resulting microstrip transmission line dimensions based on ADS simulation were extracted and describe the RF biosensor dimensions in Table 2 (located in Section 4.1.1).

5.2. Ansys HFSS 3D Simulation Final Designs

Using the numeric descriptions of Table 2, a 3-dimensional simulation model was created in the Multiphysics software HFSS. After each building block of the 3D model was created, it was simulated to determine the resulting scattering parameters.

5.2.1. Designing SMA Connectors for the Microstrip Transmission Line Biosensor

A critical piece of the microstrip transmission line biosensor simulation is the 3D modeling of the SMA connectors. Following an online tutorial and adding in design specific modifications, the following SMA model, seen in Figure 26, was connected to either end of the RF biosensor simulation model.

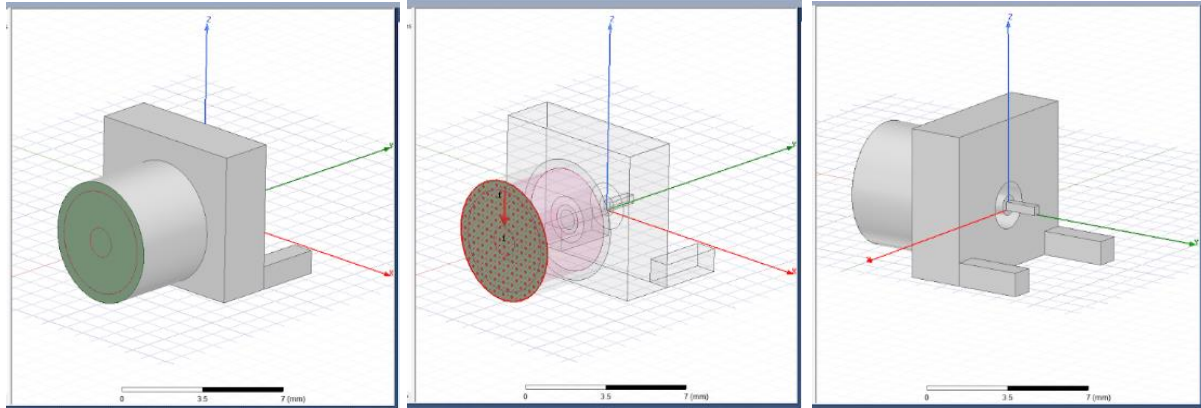


Figure 26. The Front and Back Faces of the SMA Connector Design Modeled in HFSS.

5.2.2. Microstrip Transmission Line Only (Without a Well)

After the SMA connector model was integrated with the microstrip transmission line biosensor, but before the addition of the well for holding aqueous solutions, the 50-ohm microstrip transmission line was simulated to show agreement/verification of simulations from ADS to HFSS.

5.2.3. Introduction of Microliter Well

After HFSS simulations were designed and had a successful build and simulation runs, the next step was the addition of the well with the capacity of holding 15 μ L. Figure 27. shows the HFSS top, side and ground plane views of the simulated biosensor. The HFSS component library has numerous solid and aqueous materials, which if a specific material is used in a design HFSS will also automatically loads all known characteristics such as permittivity/permeability to incorporate into the mathematical computations of resulting S-parameters. Cheap and easily

available aqueous solutions found in a lab setting and the HFSS material library were “loaded” into the simulation well and the resulting S-parameter values were simulated. These aqueous solutions included: deionized water, distilled water, and salt water.

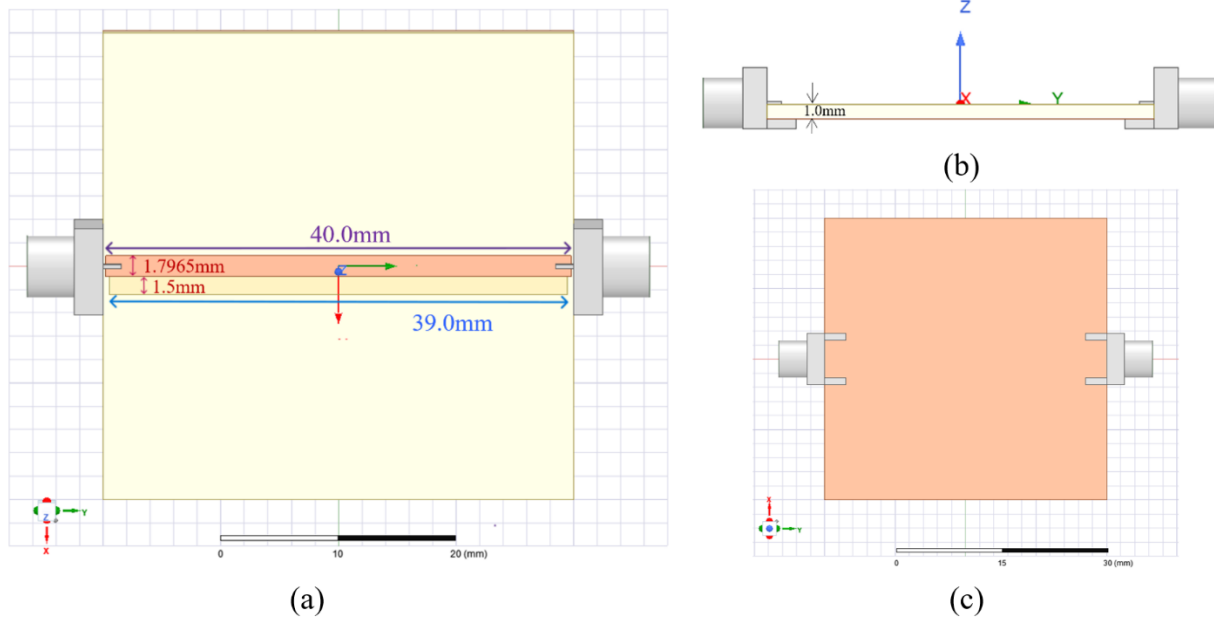


Figure 27. HFSS RF Biosensor Model: Top, Side, and Ground Plane Views.
 Note: (a) The top plane view of the 3D HFSS simulation modeled 50-ohm microstrip transmission line made with ceramic Rogers TMM4 material and SMA connectors. (b) The side view of the RF biosensor. (c) The ground plane made up of a copper sheet.

5.2.4. Resulting Electric and Magnetic Fields: Enough to Reach Well Contents

After the initial aqueous solutions simulations were run, the electric and magnetic field lines were also mapped, using HFSS software. These simulation videos were used to verify that the induced electric and magnetic field lines would reach from the transmission line to the outer edge of the well. Figure 28 shows stills of a beginning frequency, 1.5 GHz, and an ending frequency around 16.625 GHz of the animated electric field. Toward the beginning and end of the frequency sweep, the E-field lines pass through to the edges of the microliter well, albeit the lower the EM wave frequency value transmitted the lower in strength the resulting E-field lines

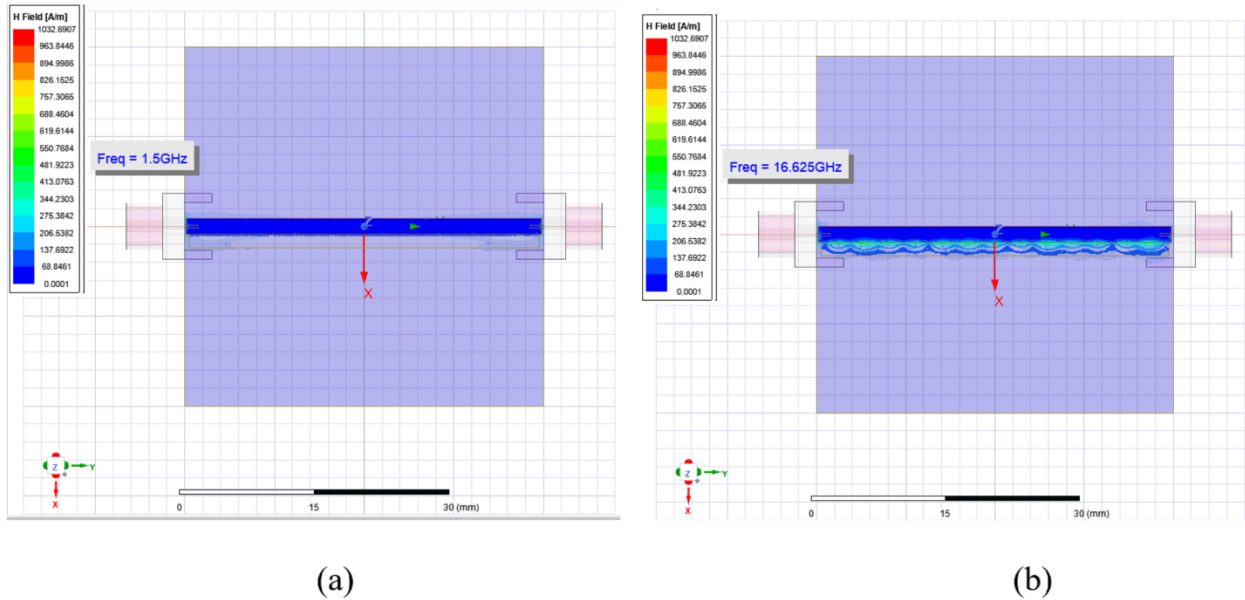


Figure 28. Simulated Electric Field Lines at Frequencies 1.5 and 16.625 GHz.
 Note: (a): HFSS simulated E-field line's strength at 1.5 GHz. (b) The simulated E-field line's strength at a frequency point of 16.625 GHz.

and vice versa at higher transmitted EM wave frequency an increase in E-field line strength.

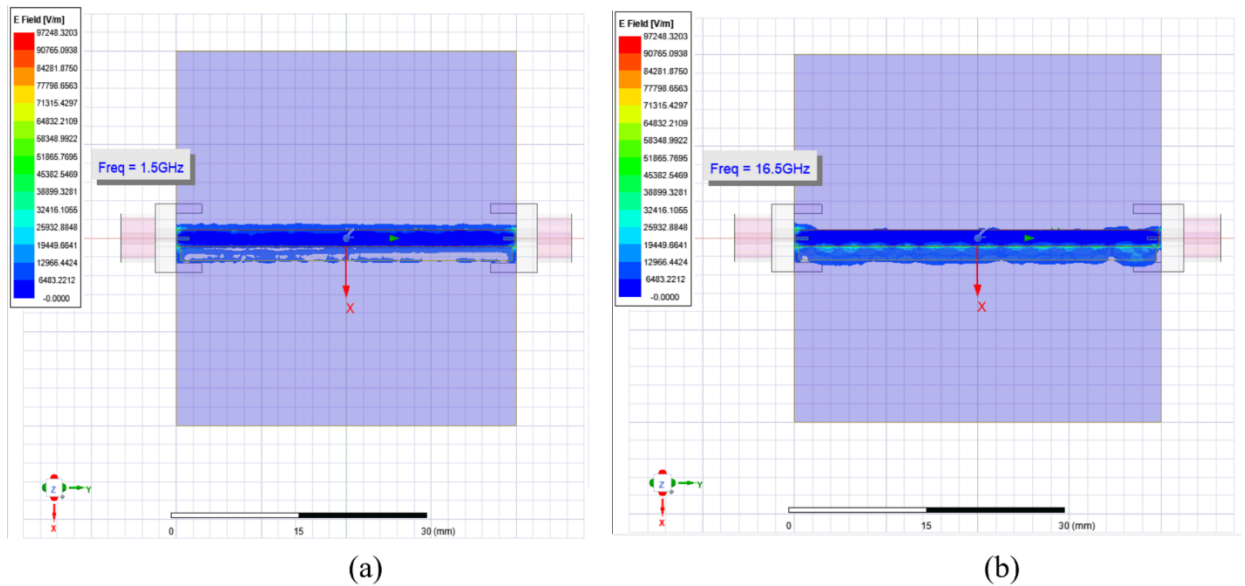


Figure 29. Simulated Magnetic Field Lines at Frequencies 1.5 and 16.625 GHz.
 Note: (a): The frequency sweep simulation of the magnetic field lines at 1.5GHz shows periodic field lines going across the microliter well edges. (b) As the frequency increases, to say 16.625 GHz, the magnetic field lines continuously cross the well's edges.

Again checking at frequencies, 1.5 GHz, and 16.625 GHz showed that the simulated magnetic field lines fully passed through the microliter well as seen in Figure 29. Therefore, the well is in a location where the simulated E- and H- fields would reach the edges of the microliter well.

5.3. MATLAB Results

The following steps were taken to import and convert data from S-parameters (dB) to voltage ratio and perform statistical analysis.

- A. Read in data (dB)
- B. Converge all 40 sweeps into one 40x1601 matrix
- C. Convert dB to voltage ratio ($\frac{V_2^+}{V_1^-}$)
- D. Calculate mean of the 40x1601 matrix
- E. Calculate standard deviation of the 40x1601 matrix
- F. Calculate 99% confidence envelope of 40 sweep dataset by finding +/- 3 standard deviations of the 40x1601 matrix
- G. Calculate standard error of the 40x1601 matrix
- H. Calculate absolute average error of the 40x1601 matrix
- I. Calculate relative standard error of the 40x1601 matrix

To verify that the MATLAB code was working as intended, it was compared to hand calculations with a worked through example of steps A-I detailed located in Appendix D. There an example of MATLAB handled the experimental and simulation data to convert decibels to voltage ratio is shown. MATLAB was also used to calculate the point-by-point mean, +/- 3 standard deviations, standard error range, absolute average error, min/max standard error range, and relative standard error range. Example MATLAB code is shown in Appendix E. for all

calculations along with sample data found in Appendix F. The same techniques used for analyzing magnitude data were used for analyzing phase data.

5.4. Statistical Analysis of Experimental Data

A parametric analysis was completed for all experimental data collected throughout the verification process. Calculations included a one sample t-test, a point-by-point mean, standard deviation, and standard error bars. These calculation techniques were also used on extracted simulation data from HFSS. Finally, the analysis calculations were used to compare simulation and experimental data.

5.4.1. Resulting Mean, Standard Deviation, and Confidence Interval Calculations Based on Repeatability Data

Each sweep consisted of a matrix holding 1601 values in decibel units. Since there were 40 sweeps total, this resulted in a 40 x 1601 matrix of data, which was first converted into a voltage ratio, $(\frac{V_2^+}{V_1^-})$. Then a point-by-point mean was calculated resulting in a 1x1601 matrix. Subsequently, the standard deviation and standard error were also calculated on the 40x1601 data set. This analysis was performed on all solutions being tested: deionized water (at ~25°C), Tris-EDTA buffer, and 0.2M, 0.6M, and 1.0M NaCl diluted in Tris-EDTA. Also, to compare with previous work, an empty well measurement set was collected.

5.5. RF Biosensor Design and Experimental Setup

The next step for verification was to experimentally test the milled biosensor throughout each step of biosensor creation. The first step was to test the milled RF biosensor as a 50Ω transmission line, before the microliter well was milled into the Rogers TMM4 material. A Keysight Full 2-Port Thru Calibration was conducted using the Keysight's 85052D 3.5mm Calibration kit and manual at the beginning of each stage of experimentation. Comparing S_{11} and

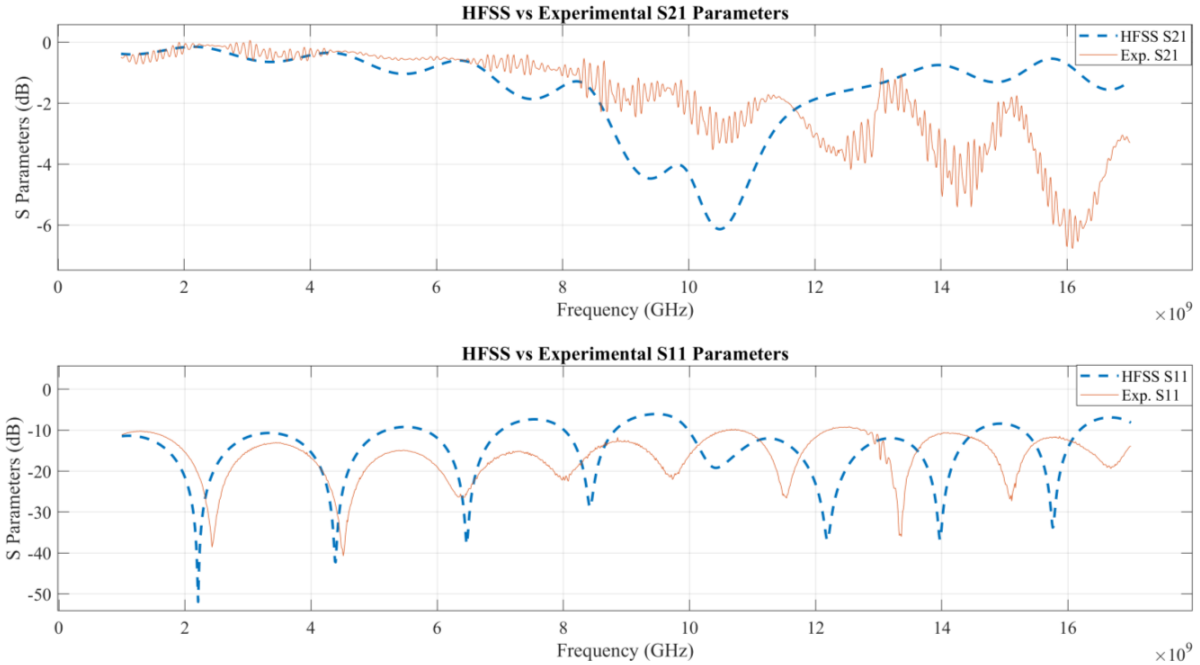


Figure 30. Comparison of ADS and Experimental S_{21} Data for a 50-ohm Transmission Line. Note: Comparing ADS simulation data with experimental results, both measuring S-parameters of the 50-ohm transmission line only, show relative agreement.

S_{21} parameter values for ADS simulation versus experimental measurements showed good agreement in waveform shape and magnitude as seen in Figure 30.

5.6. Comparison of Simulation vs. Initial Experimental RF Biosensor Testing

The next layer of prototyping included the addition of the milled microliter well and then loading of aqueous solutions into the well. This comparison was constructed in a 3D HFSS simulation to experimentally collected S-parameter measurements of the RF biosensor with an empty (or air-filled well) and account for the SMA connectors in the experimental prototype. Again, it is seen, in Figure 31, that the 3D simulation resulted in S-parameter measurements similar to experimentally gathered values.

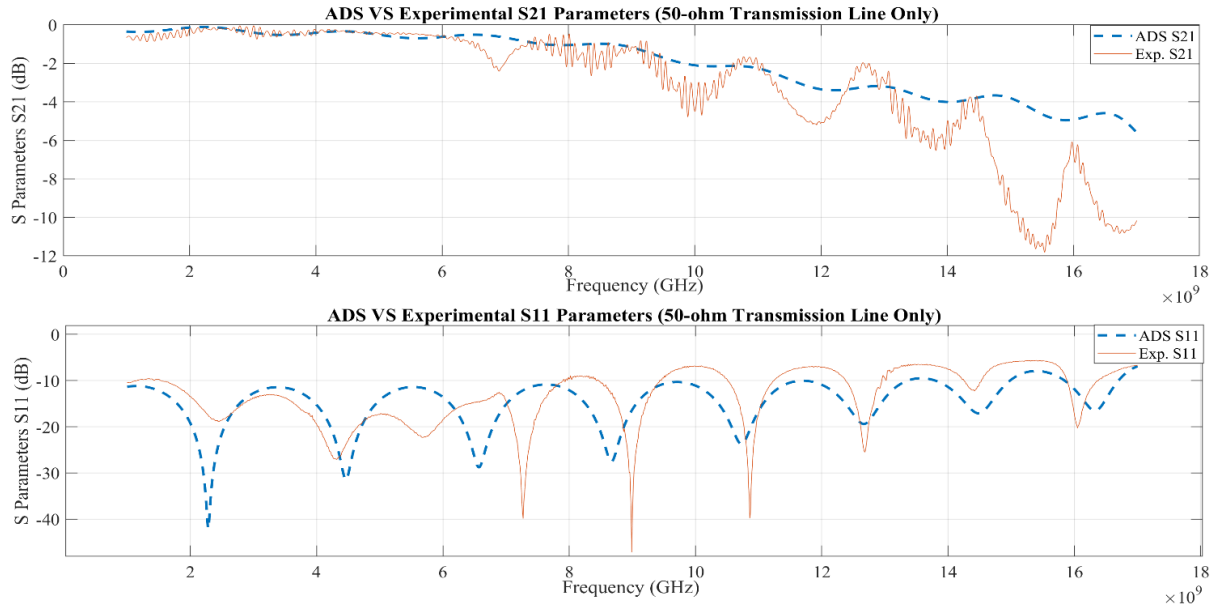


Figure 31. Comparison of HFSS and Experimental S_{21} Data for Testing the Empty Well.
 Note: Comparing the S-parameters of simulations in HFSS versus experimental data when the microliter well was left empty.

A final preliminary test was to provide evidence that the microliter well was able to detect the addition of an aqueous solution loaded into the well. To test this, deionized (DI) water measured at room temperature ($\sim 25^{\circ}\text{C}$), was pipetted into the well and 4 sets of 10 sweeps were measured for each test case to determine changes in S-parameters. Figure 32 shows the resulting S_{21} parameters have clear distinction between empty and loaded sweeps.

5.7. Verification of RF Biosensor's Measurement Validity

After initial testing confirmed an agreement between simulation and experimental results, more rigorous testing was needed to verify the RF biosensor met the work's original aims of creating a biosensor with 1) repeatability, 2) sensitivity, and 3) reproducibility, to be a viable diagnostic device. This 4-Stage Verification process was outlined in Figure 22, and results are shown in the following subsections.

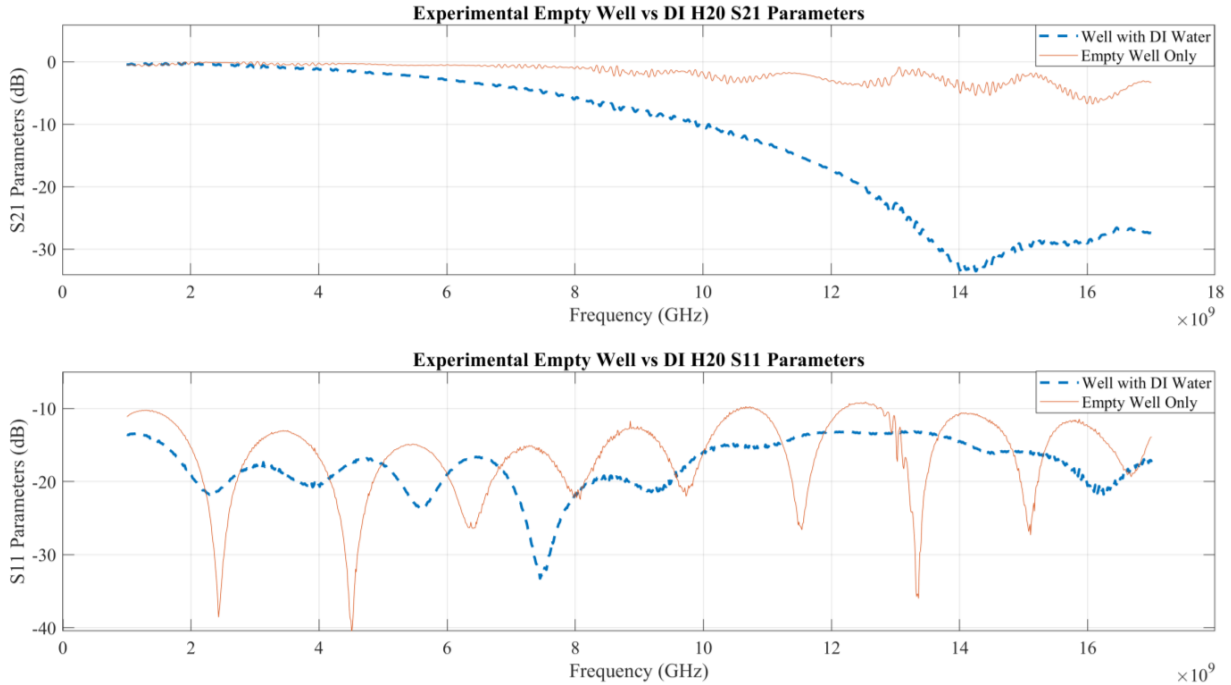


Figure 32. Comparison of Experimental S_{21} Data Measuring an Empty and Distilled Water Within the Microliter Well.

Note: Testing the RF biosensor capabilities of detecting the S-parameters of a loaded vs. non-loaded well. The resulting S_{21} waveform, after adding a load of deionized (DI) water into the well dramatically shifts the S-parameter response.

5.7.1. Repeatability Measurements

After collecting the 4 sets of 10 sweeps (40 sweeps total), outlined in Stage 1 in Figure 22 and converting the experimental data into voltage ratio values, outlined in Chapter 4.6.1, a parametric analysis was performed included calculations of a one-sample t-test, a point-by-point mean, standard deviation, and standard error bars.

To demonstrate the RF biosensor's ability to capture measurements reproducibly, the mean of each of the 4 sets of empty well measurements were calculated and plotted in Figure 33 including the standard error bars. Note that all aqueous solutions tested, or in this case lack thereof, were first converted from the scattering parameter measurements, originally collected in dB, to the voltage ratio, $(\frac{V_2^+}{V_1})$.

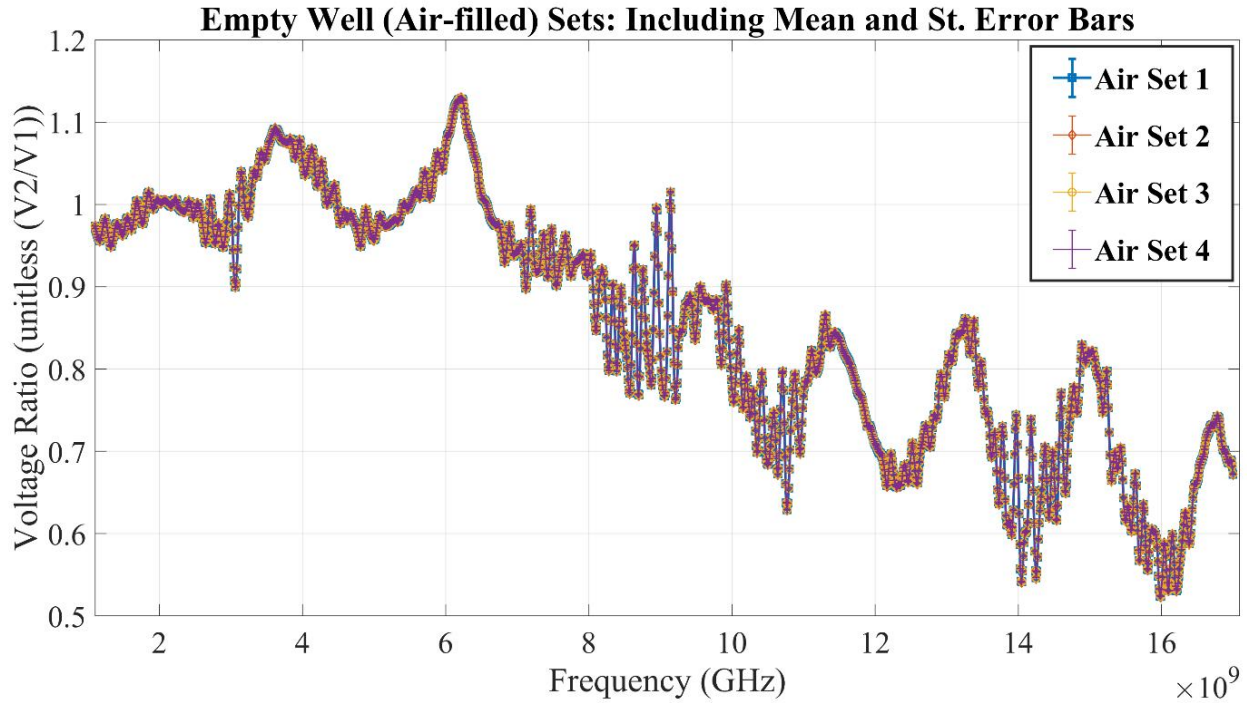


Figure 33. Comparison of Four Consecutive Experimental S_{21} Datasets Measuring an Empty (Air-filled) Microliter Well Displayed in Voltage Ratio.

Note: To verify the repeatability of the RF biosensor measurements, 4 sets of 10 sweeps were taken. As proof that the biosensor can detect a change in a loaded versus unloaded well, the above shows the voltage ratio with +/- standard error bars when the well was left empty (“filled with air”).

Using the same methodology as above, the microliter well was loaded with deionized water that was stored at room temperature ($\sim 25^{\circ}\text{C}$). shows the RF biosensor’s ability to collect repeatable measurements, even after aqueous solution removal and replacement. Slight variation can be seen between the 4 separate sweeps, but no measurements that fall outside of the standard error bars. Also of note, is the distinct waveform differences between the voltage ratio measurements when the well was loaded versus non-loaded.

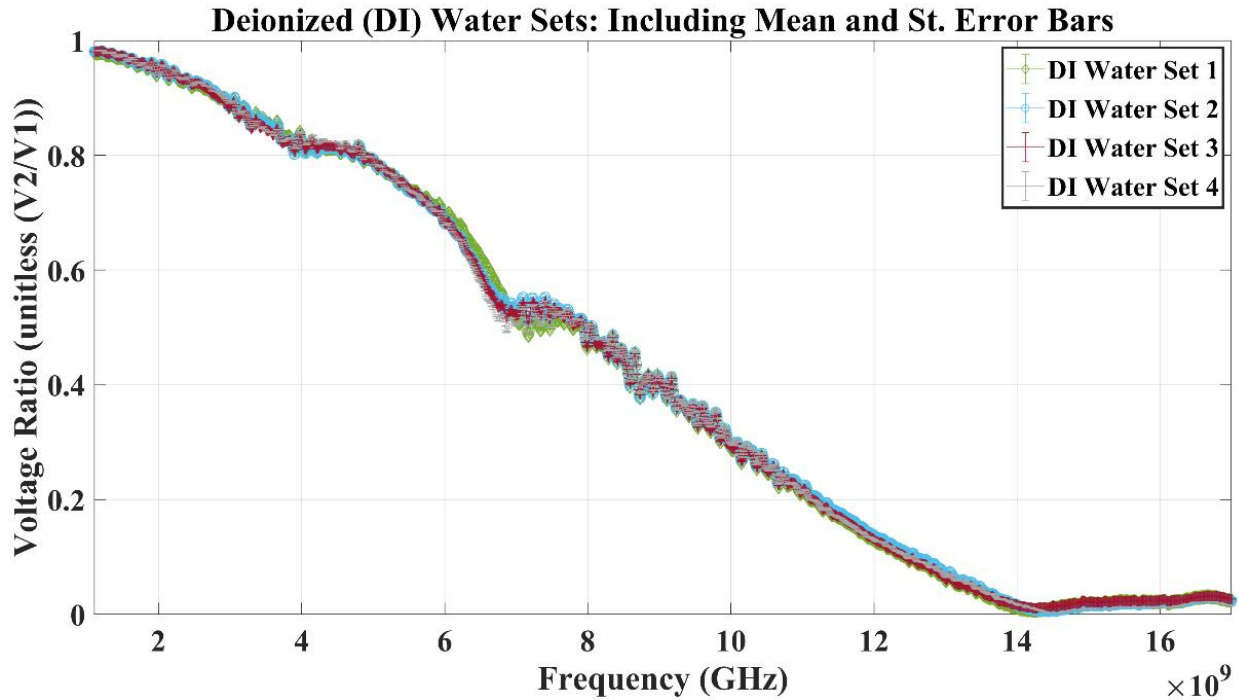


Figure 34. Comparison of Four Consecutive Experimental S_{21} Datasets Measuring Deionized Water in the Microliter Well.

Note: After loading the well with DI water at $\sim 25^{\circ}\text{C}$, the mean and corresponding \pm standard error bars show the tight overlap of each of the four sets of sweeps.

5.7.2. Sensitivity Measurements

A second important aspect of biosensing is the ability of the device to collect measurements that have low variability, or high sensitivity, between measurements. To test the sensitivity of the RF biosensor, the collected sweep data, shown in Figure 34, was analyzed to determine the amount of error, or put simply, ensure consistent values were measured for the same solution, at the same frequency, each time. To evaluate the level of error observed during the experimental testing, absolute average, min/max, and relative standard error were calculated using the parametric analysis equations outlined in Section 4.6.3. These error calculations, shown in Table 6, indicated an elevated level of sensitivity observed within experimentally gathered data.

Table 6. Calculations of Absolute Average Error, Min/Max Standard Error Range, and Relative Standard Error Range.

	Air-filled Well	DI Water
Absolute Average Error	5.08e-05	2.75e-04
Min/Max Standard Error Range	6.54e-06 to 1.85e-04	1.25e-05 to 7.40e-04
Relative Standard Error Range (%)	0.00065% to 0.025%	0.0013% to 0.36%

Note: Experimental data was measured in 4 consecutive sets of 10 sweeps without solution replacement in the well. The results show the lowest sensitivity measured by the DI water set was at maximum standard error value being 7.40×10^{-4} . For both the empty well and the well filled with DI water the relative standard error range was 0.36% or smaller, indicated by an elevated level of sensitivity in measurements.

5.7.3. Reproducibility of Measurements Independent of Vector Network Analyzers Used

The last step in the verification of the RF biosensor was to ensure the validity of the experimental setup. To complete this, two separate VNAs were used an E5071C Vector Network Analyzer (VNA), 4 port, 100kHz-20GHz, which also collected measurements from stages 2 and 3, and an N5230A VNA, 2 port, 10MHz-20GHz. The RF biosensor was connected via two 3.5mm 50Ω coaxial cables and each machine was then calibrated via the procedure in Stage 1. Afterward, the biosensor’s microliter well was loaded with various aqueous solutions. S-parameter data was measured and compared the agreement of waveform and magnitude from the two machines.

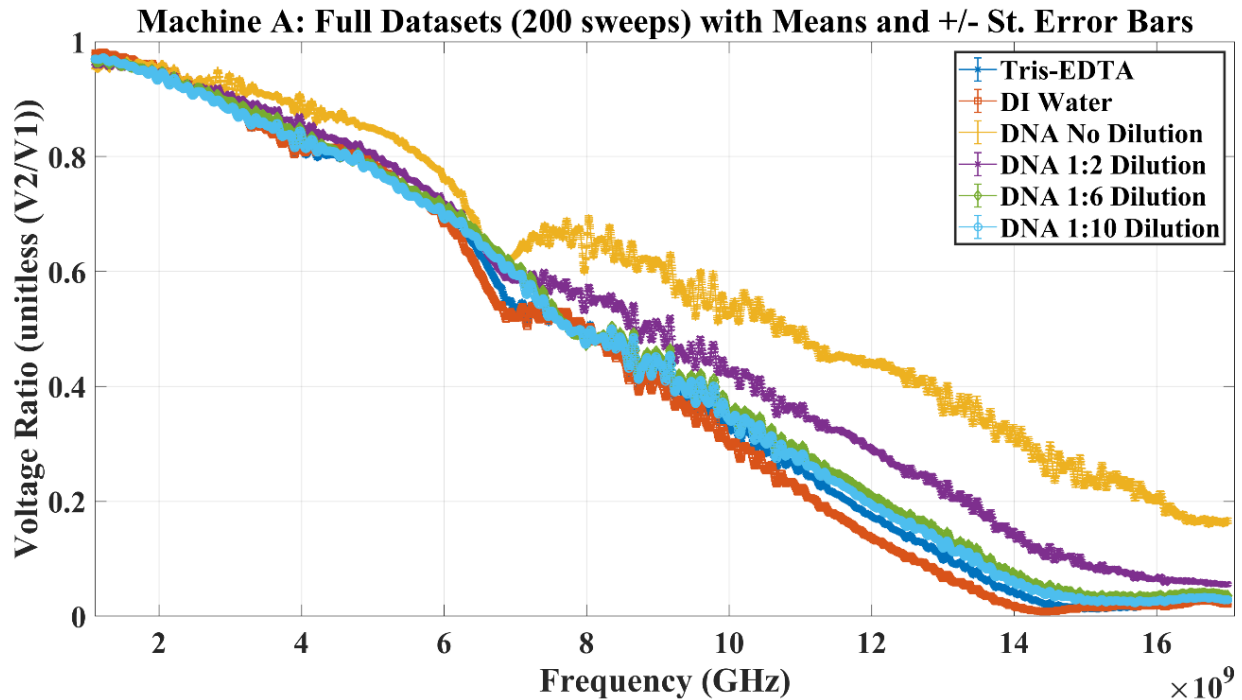


Figure 35. Voltage Ratio Measurements Taken on Machine A of Tris-EDTA, DI Water, and DNA Diluted in Increasing Concentrations Tris-EDTA Buffer.

Note: Machine A, the E5071C VNA, displays results from the six aqueous solutions being tested. The data displayed in voltage ratio shows distinct waveforms which are observably different in magnitude based on the specific concentration/type of aqueous solution tested.

Machine A, the E5071C VNA, included measurements from the well loaded with deionized (DI) water, Tris-EDTA buffer, lambda DNA (not diluted), and lambda DNA diluted in Tris-EDTA buffer of various concentrations. This portion of the experiment collected 5 sets of 40 sweeps, resulting in 200 sweeps total. Figure 35 lays out the resulting waveforms, after measurement conversion to voltage ratio, $(\frac{V_2^+}{V_1^+})$ with calculated standard error bars attached to the population mean. Each concentration of lambda DNA diluted in Tris-EDTA is distinctly observable from “No Dilution” to “1:10 Dilution.” Below is seen the voltage ratio waveforms of Tris-EDTA, DI water, and various concentrations of lambda DNA diluted in Tris-EDTA.

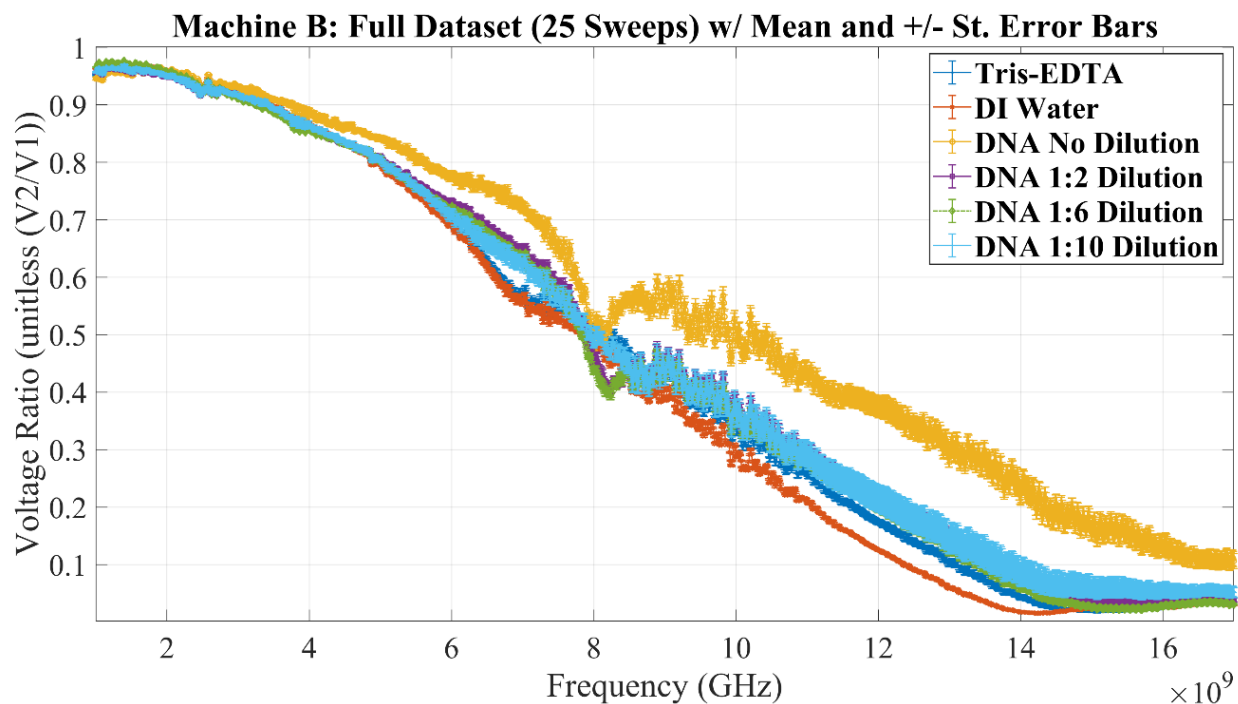


Figure 36. Voltage Ratio Measurements Taken on Machine B of Tris-EDTA, DI Water, and DNA Diluted in Increasing Concentrations Tris-EDTA Buffer.

Note: Machine B, the N5230A VNA, shows similar waveforms, displayed in voltage ratio, in comparison to Machine A. Machine B was an older machine and fewer sweeps were collected, which is noticeable in the higher amount of standard error seen in each solution's dataset.

Machine B, the N5230A VNA, includes measurements from the well loaded with deionized (DI) water, Tris-EDTA buffer, and lambda DNA diluted in Tris-EDTA buffer in various concentrations. This portion of the experiment collected 5 sets of 5 sweeps, resulting in 25 sweeps total. As seen in Figure 36, there is an increase in the noise seen on all collected measurements with increased standard error bars. This signal noise increase is believed to be caused by measurements collected by an older machine with the ability to collect dramatically fewer sweeps.

Overall, both machine A and machine B data resulted in similar waveforms and magnitudes. The mean and standard error were calculated for all aqueous solutions that were

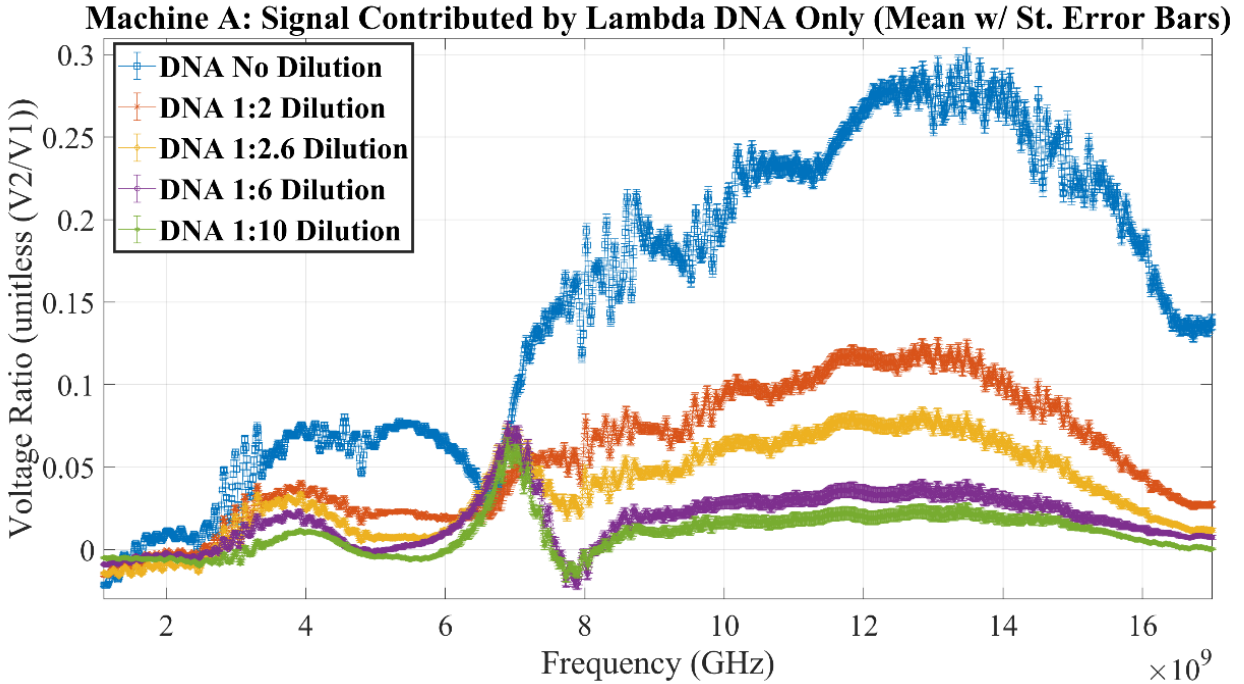


Figure 37. Voltage Ratio Magnitude Calculations from Machine A of the Resulting Signal Contributed by each Concentration of Lambda DNA.

Note: The RF biosensor shows enough sensitivity in measurements to distinguish the difference between varying concentrations of aqueous solutions held within the well.

loaded into the RF biosensor and plotted as voltage ratios. Due to the small sample size of measurements taken on machine B, the standard error seen was much larger, but the aqueous solutions similarly interacted with RF and therefore repeatable measurements could be gathered on various VNAs.

5.7.4. Determining Interaction by Calculating the DNA Signal

A specific aim of this work was to determine if an aqueous solution loaded into the RF biosensor would show levels of interaction at specific frequencies to determine any frequencies of interest to compare with past work and use in future work. Comparing Machine A and Machine B data, the following section will show the DNA “signal” from all concentrations of lambda DNA diluted in Tris-EDTA to determine this interaction. To calculate the DNA “signal” the datasets of the mean of the lambda DNA diluted in Tris-EDTA were subtracted from

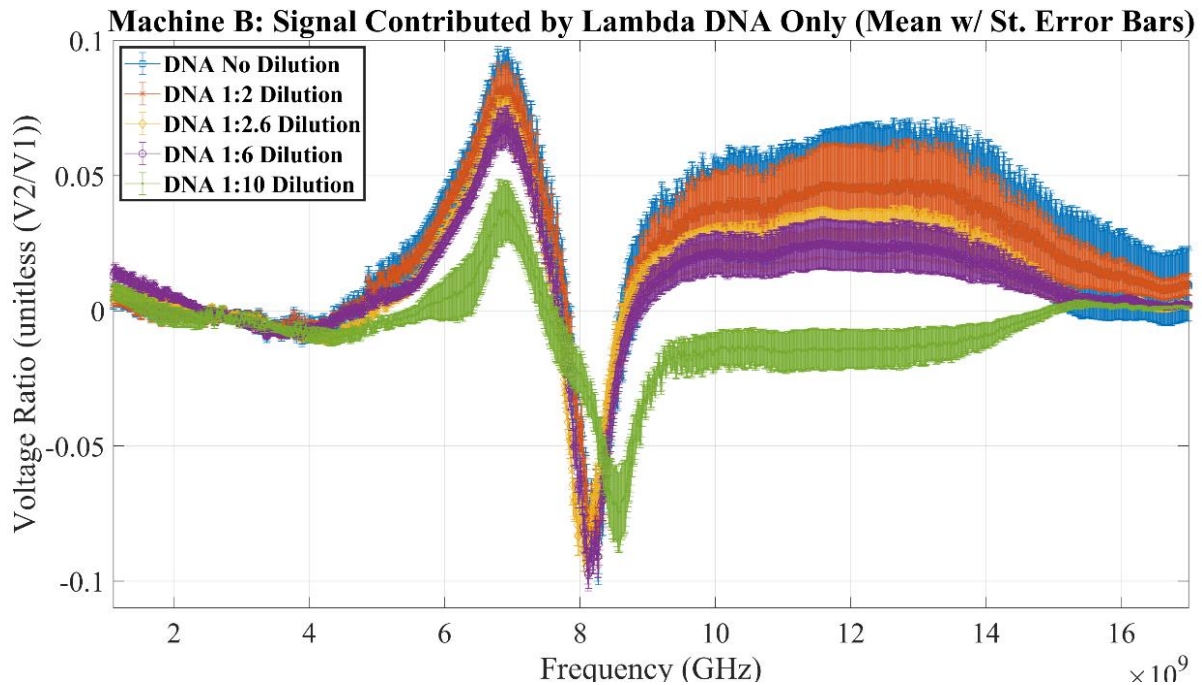


Figure 38. Voltage Ratio Magnitude Calculations from Machine B of the Resulting Signal Contributed by each Concentration of Lambda DNA.

Note: The lambda DNA signal at varying concentrations measured using Machine B. The RF biosensor sensitivity is decreased due to a much smaller sample size.

the mean of the Tris-EDTA buffer. We infer this difference of means is the result of signal due to lambda DNA alone.

Both Machine A and Machine B were able to distinguish the varying concentrations of lambda DNA. Albeit Machine A, which collected 8x the number of sweeps, resulted in data with increased sensitivity, as seen in Figure 37. Meanwhile Machine B, had decreased sensitivity, seen in Figure 38, due to a lower number of experimental sweeps taken on an older machine. However, both machines seem to layout waveforms that were similar in structure. One interesting note is that around 8GHz the lambda DNA signal dips below the y-axis resulting in negative voltage ratio values. This may be due to the fact that subtraction of two MUT signals may not accurately portray the exact lambda DNA signal. Or may show that at these frequencies the Tris-EDTA buffer is a greater contributor to the signal than the lambda DNA.

Another insight into the functionality of the RF biosensor is the extended phase measurements taken by both Machine A and Machine B. As seen below, both VNA machines display a correlation between the increase in lambda DNA concentration within the microliter well and the increase in phase measurements. Specifically, Figure 39, is the difference of means in extended phase (in degrees) measurements taken from Machine A. Again, Machine A has an increased number of experimental sweeps recorded with higher sensitivity in measurements. Meanwhile, the is the difference of means in extended phase (in degrees) measurements taken from Machine B, seen in Figure 40, has decreased sensitivity which makes an observable pattern more difficult to detect.

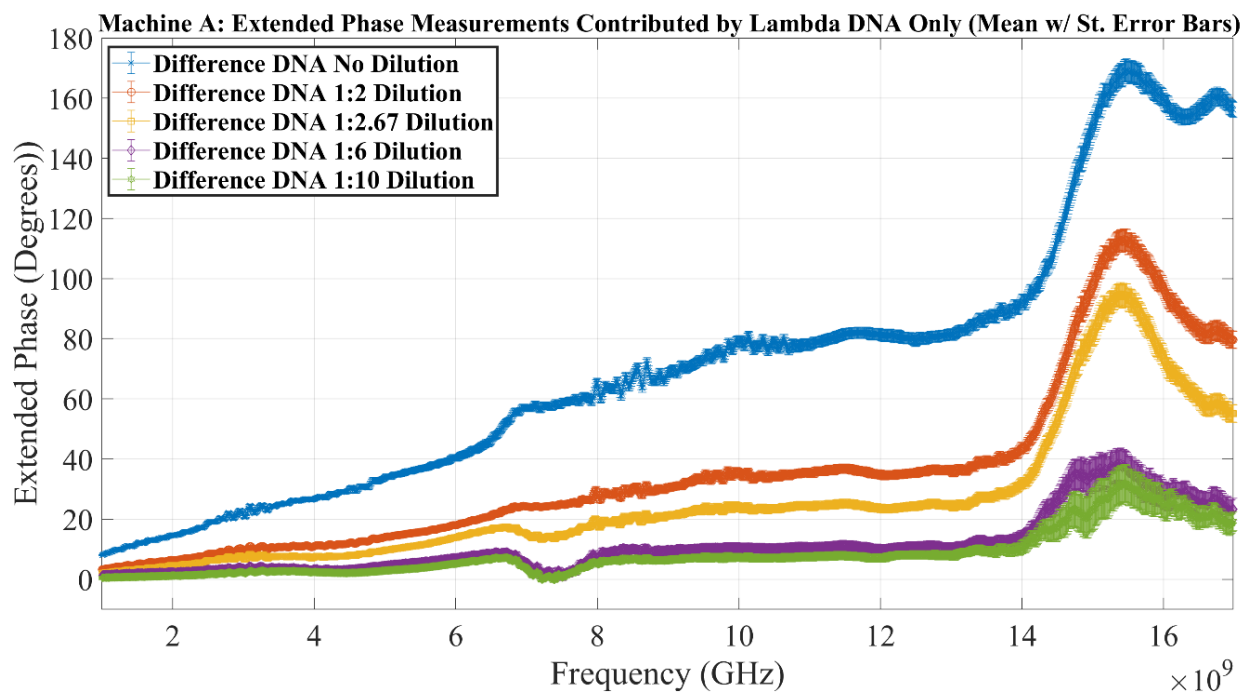


Figure 39. Voltage Ratio Extended Phase Calculations from Machine A of the Resulting Signal of each Concentration of Lambda DNA.

Note: Machine A extended phase measurements show that as the concentration of lambda DNA increases within the microliter well of the RF biosensor, the phase also increases.

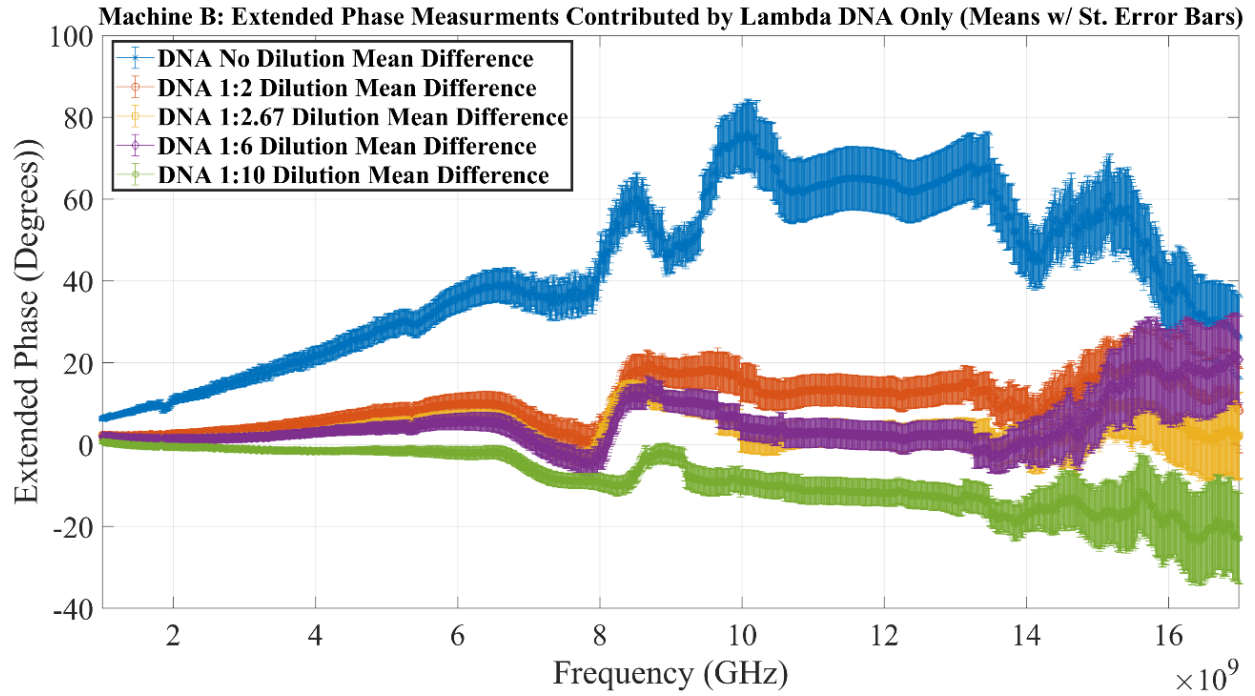


Figure 40. Voltage Ratio Extended Phase Calculations from Machine B of the Resulting Signal of each Concentration of Lambda DNA.

Note: Machine B extended phase measurements also give evidence showing that the concentration of lambda DNA increases the phase increases. This group of measurements does not as clearly demonstrate the increase of phase corresponding with increase in lambda DNA concentration, which is attributable to the reduction of experimentally gathered data.

6. DISCUSSION

The primary aim of this research was to design a millimeter-sized, inexpensive to produce, RF biosensor that measured interaction levels, in S-parameters, of aqueous materials under test during exposure to RF energy. Incremental design steps, starting with simulation models in ADS and HFSS, mapped out a prototype to test the proof of concept of the design by simulating test cases of 1) a 50-ohm microstrip transmission line, 2) an RF biosensor on TMM4 substrate including SMA connectors and a microliter well which was left empty, and finally 3) the RF biosensor prototype including the well filled with deionized water. Simulation results were compared to experimentally gathered data to verify a reliable SOP for laboratory testing. After a valid SOP was created, the proposed RF biosensor was verified by performing experimental testing to establish repeatability, sensitivity, and reproducibility. Finally, the secondary aim of this research was investigated experimentally by loading the microliter well with Tris-EDTA and increasing concentrations of lambda DNA resuspended in Tris-EDTA.

Before any verification of the RF biosensor took place, agreement between 2D and 3D simulation models with experimental data were compared and it was concluded there was good agreement between the three models - ADS, HFSS and experimental results. Comparison of HFSS simulations to experimental results showed a general waveform agreement, but a frequency shift was noted between the simulation model and lab testing. This shift could be explained by either the HFSS software making incorrect mathematical model assumptions or a non-exact SMA connector design match compared to what was used in experimental testing.

After Stage 1, calibration of the experimental setup, Stage 2, the repeatability verification stage, was conducted where two drastically different voltage waveforms were observed when comparing an empty microliter well to a deionized (DI) water filled well. These two waveforms

demonstrated the biosensor's ability to determine if the microliter well was loaded or not. Despite the aqueous solution being replaced between each set, which potentially introduces error into the system, a low relative standard error range was observed. Sensitivity within measurements being defined in this work as the variation between two or more repeated collections of the same data. So, with the maximum standard error observed within the range of 10^{-4} to 10^{-5} led to the conclusion the data collected experimentally was highly sensitive, satisfying the requirements of Stage 3 in the experimentation protocol. All of these findings gave confidence in the RF biosensor's ability to collect repeatable and sensitive measurements.

Experimental protocol Stage 4, focusing on reproducibility of gathered measurements yielded testing of two separate VNA machines. The E5071C VNA, labeled Machine A in results section, demonstrated distinguishable waveforms between various concentrations of aqueous lambda DNA diluted in Tris-EDTA. Machine A's ability to measure S-parameters with small standard error enabled the distinction of these various MUTs to be observed, as seen in Figure 35. The older model, N5230A VNA, labeled Machine B, captured similar waveforms to Machine A, but since it did not have an automatic sweep feature, less experiment sets were gathered therefore making the error and noise experienced on the measurements greater.

Finally addressing the second research aim of this dissertation, the signal resulting from lambda DNA alone was backed out from experimental measurements. The signal was approximated by calculating the mean and standard error for each concentration of lambda DNA diluted in Tris-EDTA loaded into the microliter well. Since each lambda DNA solution was resuspended in the Tris-EDTA buffer, the dataset means at each lambda DNA concentration was subtracted from the mean of the Tris-EDTA buffer only. The resulting "Lambda DNA Only" waveforms, shown in Figure 37 and Figure 38, display the interaction of RF from lambda DNA

alone, at each dilution. These signals show detectable differences. As the concentration of lambda DNA increases so do the resulting voltage ratio measurements and alternatively as the concentration of lambda DNA decreases in the MUT so does the resulting voltage ratio.

The results suggest the interaction between radio frequencies and lambda DNA change with respect to the frequency transmitted through the aqueous MUT. When the voltage ratio ($\frac{V_2^+}{V_1^+}$), observed a value less than one, it was understood that the voltage at Port 2 (V_2^+) is smaller than the voltage at Port 1 (V_1^+). Meaning the transmitted energy is absorbed or stored within the system, however, it is not possible to conclude which with the current experimental data and setup. Conversely, observed voltage ratio values greater than zero, indicated frequencies where the lambda DNA was interacting at higher levels than the Tris-EDTA buffer possibly due to the structure and polarity of each. Finally, an interesting range occurred when the voltage ratio fell below zero in value, which indicated to the authors that the Tris-EDTA buffer interacted with those radio frequencies at a higher rate than the lambda DNA did.

7. CONCLUSION

The RF biosensor proposed, designed, and validated in this research, offers a sensing option that meets the needs for a millimeter-sized device, requiring microliter sample volumes within a non-ionizing frequency range, operating at broadband sweep of 1.0-17.0 GHz, to measure interaction levels between MUTs and radiofrequency energy. To do this a rendering was proposed, built in 2D simulation software ADS and then 3D simulation software HFSS, which resulted in S-parameter results. Next various iterations of the RF biosensor were milled to compare experimental and simulation results. With agreement in simulation and experimental results, tests were conducted to ensure 1) the RF biosensor could detect loaded versus unloaded well conditions, 2) TMM4's ceramic porosity was not absorbing a large amount of the MUT, and 3) the biosensor's top and ground plane were not heating during experimentation. After testing these conditions, the RF biosensor prototype moved beyond the proof-of-concept phase and onto validation testing.

By designing a 4-stage standard testing procedure, the RF biosensor was validated in its ability to collect repeatable, sensitive, and reproducible experimental results. This work obtained highly repeatable and sensitive measurements with maximum standard error values calculated in the 10^{-4} range. These results showed that interaction levels between MUTs and radio frequencies fluctuated as the concentration of the MUT either increased or decreased. Repeating the experimental testing using a second, older VNA showed measurement reproducibility independent of machine use by similar resulting data, albeit with higher noise due to the decreased number of sweeps collected within a given time period.

With validation complete, the RF biosensor also collected experimental results giving insight into the interaction between lambda DNA and radio frequencies of 1.0-17.0 GHz. These

results showed distinctive resulting waveforms of each individual concentration of lambda DNA resuspended in Tris-EDTA buffer. A finding of interest was that as DNA concentrations increased, the resulting voltage ratio waveforms also increased in magnitude and extended phase. This suggests the increased concentration of lambda DNA present in the material being loaded and tested inside the microliter well interacts at a higher level. This result could also suggest a baseline concentration that is needed for proper detection using the RF biosensor.

To try to observe the resulting interaction signal between radio frequency and lambda DNA, the point-by-point mean of the Tris-EDTA buffer was subtracted from the point-by-point mean of the lambda DNA diluted in Tris-EDTA buffer. These values were calculated as voltage ratios for easier comparison since the values are linear as compared to dB which is exponential. Voltage ratios with values greater than zero observed in the lambda DNA only signals indicate radio frequencies interacted in a greater way with the lambda DNA. Conversely, voltage ratios less than zero indicate radio frequencies interacted with the Tris-EDTA buffer in a greater way.

These results suggest that during applied EM fields, a MUT is changing its behavior in some way, whether that be by ion shifting, polarizations occurring, or molecular change in shape or orientation, as some possible examples. Currently, the RF biosensor design is not equipped to extrapolate the detection of what is happening to the MUT during applied EM field exposure. However, it is reasonable to suggest that absorption or storage of EM energy is taking place on the molecular level of the MUT inside the microliter well of the biosensor.

To summarize, the results of this work show a valid biosensor design, requiring microliter quantities, that can measure interaction levels of electromagnetic energy and MUTs with high repeatability, sensitivity, and reproducibility. This design innovatively meets the need for a biosensing device requiring only microliter-sized samples for testing. Other dielectric

sensing classifications of the biosensor design include a label-free MUT, operating in non-ionizing frequency ranges, collecting ex-vivo measurements, via direct biosensing.

Even though the field of biosensing is incredibly massive and fragmented by numerous sensing types, measurement schemes, operational frequencies, detection methods, and targeted MUTs, there is still a great amount of space for improvement to continue enhancing patient care and diagnostic testing. This dissertation work also has many potential directions to take for future improvements. To start, an increased variety of liquids should be simulated in HFSS and then experimentally tested by the RF biosensor. These MUTs could include oils, buffers, household liquids, and most interestingly, blood samples used in healthcare diagnostics which test glucose, nutrient, and protein levels within humans.

Another area of improvement would be to investigate and derive theoretical models to communicate the experimental results as complex permittivity values, derive a circuit model of the RF biosensor's behavior, and create a predictive model for measured yet unknown MUTs. Creating a mathematical model to convert collected S-parameter results to complex permittivity values would bridge a gap between a full body of previous work on dielectric sensing reporting results as complex permittivity values and this RF biosensor's S-parameter results. Deriving a theoretical model or circuit model of the behavior of the microstrip transmission line with the inclusion of the microliter well would also be an area of interest. Finally, the development of a predictive model based on interaction behaviors of characterized MUTs could lead to the ability to predict the presence of unknown MUTs inside the microliter well. The development of these models could yield an impactful integration of the RF biosensor with a handheld, transportable VNA device leading to an innovative POCT device.

REFERENCES

- [1] R. Chang and K. Goldsby, *Chemistry*, 11th ed. McGraw-Hill, 2013.
- [2] M. Karplus and H. J. Kolker, “Van der Waals Forces in Atoms and Molecules,” *J. Chem. Phys.*, vol. 41, no. 12, pp. 3955–3961, Dec. 1964, doi: 10.1063/1.1725842.
- [3] B. R. Holstein, “The van der Waals interaction,” *Am. J. Phys.*, vol. 69, no. 4, pp. 441–449, Apr. 2001, doi: 10.1119/1.1341251.
- [4] A. Ben-Naim, “Water and Aqueous Solutions,” in *Statistical Thermodynamics for Chemists and Biochemists*, Boston, MA: Springer, 1992.
- [5] F. E. Harris and C. T. O’Konski, “Dielectric Properties of Aqueous Ionic Solutions at Microwave Frequencies,” *J. Phys. Chem.*, vol. 61, no. 3, pp. 310–319, Mar. 1957, doi: 10.1021/j150549a009.
- [6] S. Romanenko, R. Begley, A. R. Harvey, L. Hool, and V. P. Wallace, “The interaction between electromagnetic fields at megahertz, gigahertz and terahertz frequencies with cells, tissues and organisms: risks and potential,” *J. R. Soc. Interface*, vol. 14, no. 137, p. 20170585, Dec. 2017, doi: 10.1098/rsif.2017.0585.
- [7] C. A. Balanis, *Advanced Engineering Electromagnetics*, 2nd ed. John Wiley & Sons, Inc., 2012.
- [8] D. Pozar, *Microwave Engineering*, 4th ed. University of Massachusetts, MA, USA: John Wiley & Sons, Inc., 2012.
- [9] V. Mandrić Radivojević, S. Rupčić, M. Srnović, and G. Benšić, “Measuring the Dielectric Constant of Paper Using a Parallel Plate Capacitor,” *Int. J. Electr. Comput. Eng. Syst.*, vol. 9, no. 1, pp. 1–10, 2018, doi: 10.32985/ijeces.9.1.1.
- [10] M. Havas, “Biological effects of non-ionizing electromagnetic energy: A critical review of the reports by the US National Research Council and the US National Institute of Environmental Health Sciences as they relate to the broad realm of EMF bioeffects,” *Environ. Rev.*, vol. 8, no. 3, pp. 173–253, Mar. 2000, doi: 10.1139/a00-004.
- [11] L. C. Shen and J. A. Kong, *Applied Electromagnetism (Pws Engineering Foundation)*, 3rd Edition. Boston: Cengage Learning, 1995.
- [12] K. R. Foster, M. C. Ziskin, and Q. Balzano, “Thermal Response of Human Skin to Microwave Energy: A Critical Review,” *Health Phys.*, vol. 111, no. 6, pp. 528–541, Dec. 2016, doi: 10.1097/HP.0000000000000571.
- [13] D. R. Black and L. N. Heynick, “Radiofrequency (RF) effects on blood cells, cardiac, endocrine, and immunological functions,” *Bioelectromagnetics*, vol. 24, no. S6, pp. S187–S195, Nov. 2003, doi: 10.1002/bem.10166.

- [14] Y. Mackeyev, C. Mark, N. Kumar, and R. E. Serda, “The influence of cell and nanoparticle properties on heating and cell death in a radiofrequency field,” *Acta Biomater.*, vol. 53, pp. 619–630, Apr. 2017, doi: 10.1016/j.actbio.2017.02.003.
- [15] D. J. Panagopoulos, O. Johansson, and G. L. Carlo, “Evaluation of Specific Absorption Rate as a Dosimetric Quantity for Electromagnetic Fields Bioeffects,” *PLoS ONE*, vol. 8, no. 6, p. e62663, Jun. 2013, doi: 10.1371/journal.pone.0062663.
- [16] J. Vanderstraeten and L. Verschaeve, “Gene and protein expression following exposure to radiofrequency fields from mobile phones,” *Environ. Health Perspect.*, vol. 116, no. 9, pp. 1131–1135, Sep. 2008, doi: 10.1289/ehp.11279.
- [17] L. J. Challis, “Mechanisms for interaction between RF fields and biological tissue,” *Bioelectromagnetics*, vol. 26, no. S7, pp. S98–S106, Jun. 2005, doi: 10.1002/bem.20119.
- [18] “IEEE Standard for Safety Levels with Respect to Human Exposure to Radio Frequency Electromagnetic Fields, 3 kHz to 300 GHz,” *IEEE Std C951-2005 Revis. IEEE Std C951-1991*, pp. 1–238, Apr. 2006, doi: 10.1109/IEEESTD.2006.99501.
- [19] “6 Techniques for Measuring Dielectric Properties,” 2015, pp. 52–77. doi: 10.1515/9783110455403-007.
- [20] A. Salim and S. Lim, “Review of Recent Metamaterial Microfluidic Sensors,” *Sensors*, vol. 18, no. 1, p. 232, Jan. 2018, doi: 10.3390/s18010232.
- [21] F. Artis *et al.*, “Microwaving Biological Cells: Intracellular Analysis with Microwave Dielectric Spectroscopy,” *IEEE Microw. Mag.*, vol. 16, no. 4, pp. 87–96, May 2015, doi: 10.1109/MMM.2015.2393997.
- [22] P. Mehrotra, B. Chatterjee, and S. Sen, “EM-Wave Biosensors: A Review of RF, Microwave, mm-Wave and Optical Sensing,” *Sensors*, vol. 19, no. 5, p. 1013, Feb. 2019, doi: 10.3390/s19051013.
- [23] W. S. Klug, M. R. Cummings, C. A. Spencer, and M. A. Palladino, *Essentials of Genetics*, 8th ed. Pearson Education Inc., 2013.
- [24] K. C. Yaw, “Measurement of Dielectric Material Properties,” p. 36.
- [25] W. Choi and H.-D. Yun, “21 - Non-destructive evaluation (NDE) of composites: use of acoustic emission (AE) techniques,” in *Non-Destructive Evaluation (NDE) of Polymer Matrix Composites*, V. M. Karbhari, Ed., Woodhead Publishing, 2013, pp. 557–573. doi: 10.1533/9780857093554.4.557.
- [26] “Measuring Dielectric Properties Using Keysight’s Materials Measurement Solutions - Brochure,” p. 7.

- [27] M. Pearson, J. Parrow, B. Braaten, J. Wandler, K. Nawarathna, and D. Ewert, "Interaction Of Radio Frequency And Lambda-DNA," p. 6, 2015.
- [28] "Keysight N1500A technical documentation.pdf." Keysight Technologies, Feb. 16, 2018. [Online]. Available: <https://literature.cdn.keysight.com/litweb/pdf/5992-0263EN.pdf?id=2547117>
- [29] G. Guarin, M. Hofmann, J. Nehring, R. Weigel, G. Fischer, and D. Kissinger, "Miniature Microwave Biosensors: Noninvasive Applications," *IEEE Microw. Mag.*, vol. 16, no. 4, pp. 71–86, May 2015, doi: 10.1109/MMM.2015.2394024.
- [30] S. Grimnes and O. Martinsen, *Bioimpedance and Bioelectricity Basics*, 3rd ed. Academic Press, 2014.
- [31] V. Rawat, S. Dhobale, and S. N. Kale, "Ultra-fast selective sensing of ethanol and petrol using microwave-range metamaterial complementary split-ring resonators," *J. Appl. Phys.*, vol. 116, no. 16, p. 164106, Oct. 2014, doi: 10.1063/1.4900438.
- [32] M. Bakir, "Electromagnetic-Based Microfluidic Sensor Applications," *J. Electrochem. Soc.*, vol. 164, no. 9, pp. B488–B494, 2017, doi: 10.1149/2.0171712jes.
- [33] H. K. Kim, M. Yoo, and S. Lim, "Novel ethanol chemical sensor using microfluidic metamaterial," in *2015 IEEE International Symposium on Antennas and Propagation & USNC/URSI National Radio Science Meeting*, Vancouver, BC, Canada: IEEE, Jul. 2015, pp. 1358–1359. doi: 10.1109/APS.2015.7305068.
- [34] W. Withayachumnankul, K. Jaruwongrungrsee, A. Tuantranont, C. Fumeaux, and D. Abbott, "Metamaterial-based microfluidic sensor for dielectric characterization," *Sens. Actuators Phys.*, vol. 189, pp. 233–237, Jan. 2013, doi: 10.1016/j.sna.2012.10.027.
- [35] H.-J. Lee, H.-S. Lee, K.-H. Yoo, and J.-G. Yook, "DNA sensing using split-ring resonator alone at microwave regime," *J. Appl. Phys.*, vol. 108, no. 1, p. 014908, Jul. 2010, doi: 10.1063/1.3459877.
- [36] C. Ellison, M. Mckeown, S. Trabelsi, and D. Boldor, "Dielectric Properties of Biomass/Biochar Mixtures at Microwave Frequencies," *Energies*, vol. 10, Apr. 2017, doi: 10.3390/en10040502.
- [37] A. K. Jonscher, "Low-loss dielectrics," p. 12, 1999.
- [38] J. Baker-Jarvis and S. Kim, "The Interaction of Radio-Frequency Fields with Dielectric Materials at Macroscopic to Mesoscopic Scales," *J. Res. Natl. Inst. Stand. Technol.*, vol. 117, p. 1, 2012, doi: 10.6028/jres.117.001.
- [39] W. Stutzman and G. Thiele, *Antenna Theory and Design*, 3rd ed. John Wiley & Sons, Inc., 2013.

- [40] A. Hobson, “HANDBOOK OF MODERN SENSORS, by Jacob Fraden, Springer/AIP Press, 2004, xvii+ 589 pp., with index, ISBN 0-387-00750-4. 295 ref. distributed chapter by chapter.(Hardback£ 73),” *Robotica*, vol. 23, no. 3, pp. 397–397, 2005.
- [41] K. Entesari, A. A. Helmy, and M. Moslehi-Bajestan, “Integrated Systems for Biomedical Applications: Silicon-Based RF/Microwave Dielectric Spectroscopy and Sensing,” *IEEE Microw. Mag.*, vol. 18, no. 5, pp. 57–72, Jul. 2017, doi: 10.1109/MMM.2017.2690884.
- [42] J. Leroy *et al.*, “Microfluidic biosensors for microwave dielectric spectroscopy,” *Sens. Actuators Phys.*, vol. 229, pp. 172–181, Jun. 2015, doi: 10.1016/j.sna.2015.04.002.
- [43] S. Kobel and M. P. Lutolf, “Biomaterials meet microfluidics: building the next generation of artificial niches,” *Curr. Opin. Biotechnol.*, vol. 22, no. 5, pp. 690–697, Oct. 2011, doi: 10.1016/j.copbio.2011.07.001.
- [44] E. Samiei, M. Tabrizian, and M. Hoorfar, “A review of digital microfluidics as portable platforms for lab-on a-chip applications,” *Lab. Chip*, vol. 16, no. 13, pp. 2376–2396, 2016, doi: 10.1039/C6LC00387G.
- [45] G. M. Whitesides, “The origins and the future of microfluidics,” *Nature*, vol. 442, no. 7101, pp. 368–373, Jul. 2006, doi: 10.1038/nature05058.
- [46] M. Borse, S. Bhushan, D. K. Walters, and G. W. Burgreen, “Numerical simulations of flow pattern and particle trajectories in feline aorta for hypertrophic cardiomyopathy heart conditions,” *Eng. Appl. Comput. Fluid Mech.*, vol. 12, no. 1, pp. 57–73, Jan. 2018, doi: 10.1080/19942060.2017.1339640.
- [47] C. Gabriel, S. Gabriel, and E. Corthout, “The dielectric properties of biological tissues: I. Literature survey,” *Phys. Med. Biol.*, vol. 41, no. 11, pp. 2231–2249, Nov. 1996, doi: 10.1088/0031-9155/41/11/001.
- [48] S. Gabriel, R. W. Lau, and C. Gabriel, “The dielectric properties of biological tissues: II. Measurements in the frequency range 10 Hz to 20 GHz,” *Phys. Med. Biol.*, vol. 41, no. 11, pp. 2251–2269, Nov. 1996, doi: 10.1088/0031-9155/41/11/002.
- [49] S. Gabriel, R. W. Lau, and C. Gabriel, “The dielectric properties of biological tissues: III. Parametric models for the dielectric spectrum of tissues,” *Phys. Med. Biol.*, vol. 41, no. 11, pp. 2271–2293, Nov. 1996, doi: 10.1088/0031-9155/41/11/003.
- [50] J. L. Schepps and K. R. Foster, “The UHF and microwave dielectric properties of normal and tumour tissues: variation in dielectric properties with tissue water content,” *Phys. Med. Biol.*, vol. 25, no. 6, pp. 1149–1159, Nov. 1980, doi: 10.1088/0031-9155/25/6/012.

- [51] J. Baker-Jarvis, M. D. Janezic, J. H. J. Grosvenor, and R. G. Geyer, "Transmission/reflection and short-circuit line methods for measuring permittivity and permeability," p. 124.
- [52] M. C. Jain, A. V. Nadaraja, S. Mohammadi, B. M. Vizcaino, and M. H. Zarifi, "Passive Microwave Biosensor for Real-Time Monitoring of Subsurface Bacterial Growth," *IEEE Trans. Biomed. Circuits Syst.*, vol. 15, no. 1, pp. 122–132, Feb. 2021, doi: 10.1109/TBCAS.2021.3055227.
- [53] J. Baker-Jarvis, E. J. Vanzura, and W. A. Kissick, "Improved technique for determining complex permittivity with the transmission/reflection method," *IEEE Trans. Microw. Theory Tech.*, vol. 38, no. 8, pp. 1096–1103, Aug. 1990, doi: 10.1109/22.57336.
- [54] S. Subbaraj, V. S. Ramalingam, M. Kanagasabai, E. F. Sundarsingh, Y. P. Selvam, and S. Kingsley, "Electromagnetic Nondestructive Material Characterization of Dielectrics Using EBG Based Planar Transmission Line Sensor," *IEEE Sens. J.*, vol. 16, no. 19, pp. 7081–7087, Oct. 2016, doi: 10.1109/JSEN.2016.2591320.
- [55] K. N. Bocan, M. H. Mickle, and E. Sejdic, "Multi-Disciplinary Challenges in Tissue Modeling for Wireless Electromagnetic Powering: A Review," *IEEE Sens. J.*, vol. 17, no. 20, pp. 6498–6509, Oct. 2017, doi: 10.1109/JSEN.2017.2748338.
- [56] K. Kupfer, *Electromagnetic Aquametry: Electromagnetic Wave Interaction with Water and Moist Substances*, 1st ed. Springer-Verlag, 2005.
- [57] Note, Application and others, "Basics of measuring the dielectric properties of materias," *Agilent Technologies*, p. 1e31, 2006.
- [58] E. Balidemaj *et al.*, "In vivo electric conductivity of cervical cancer patients based on maps at 3T MRI," *Phys. Med. Biol.*, vol. 61, no. 4, p. 1596, 2016.
- [59] P. Gajsek, W. D. Hurt, J. M. Ziriach, and P. A. Mason, "Parametric dependence of SAR on permittivity values in a man model," *IEEE Trans. Biomed. Eng.*, vol. 48, no. 10, pp. 1169–1177, 2001.
- [60] R. Andreuccetti, R. Fossi, and C. Petrucci, "An Internet resource for the calculation of the dielectric properties of body tissues in the frequency range 10 Hz-100 GHz," *Florence Italy Tech Rep*, 1997, [Online]. Available: Available: <http://niremf.ifac.cnr.it/tissprop/>
- [61] H. P. Schwan, "Application of UHF impedance measuring techniques in biophysics," *IRE Trans. Instrum.*, pp. 75–83, 1955.
- [62] R. Pethig and D. B. Kell, "The passive electrical properties of biological systems: their significance in physiology, biophysics and biotechnology," *Phys. Med. Biol.*, vol. 32, no. 8, p. 933, 1987.

- [63] “Romanenko et al. - 2017 - The interaction between electromagnetic fields at .pdf.”
- [64] C. Rønne, L. Thrane, P.-O. Åstrand, A. Wallqvist, K. V. Mikkelsen, and S. R. Keiding, “Investigation of the temperature dependence of dielectric relaxation in liquid water by THz reflection spectroscopy and molecular dynamics simulation,” *J. Chem. Phys.*, vol. 107, no. 14, pp. 5319–5331, 1997.
- [65] E. Pickwell and V. Wallace, “Biomedical applications of terahertz technology,” *J. Phys. Appl. Phys.*, vol. 39, no. 17, p. R301, 2006.
- [66] J. Kindt and C. Schmuttenmaer, “Far-infrared dielectric properties of polar liquids probed by femtosecond terahertz pulse spectroscopy,” *J. Phys. Chem.*, vol. 100, no. 24, pp. 10373–10379, 1996.
- [67] J.-H. Son, *Terahertz biomedical science and technology*. CRC Press, 2014.
- [68] C. Rønne and S. R. Keiding, “Low frequency spectroscopy of liquid water using THz-time domain spectroscopy,” *J. Mol. Liq.*, vol. 101, no. 1–3, pp. 199–218, 2002.
- [69] L. Thrane, R. H. Jacobsen, P. U. Jepsen, and S. R. Keiding, “THz reflection spectroscopy of liquid water,” *Chem. Phys. Lett.*, vol. 240, no. 4, pp. 330–333, 1995.
- [70] J. Šponer, J. Leszczynski, and P. Hobza, “Electronic properties, hydrogen bonding, stacking, and cation binding of DNA and RNA bases,” *Biopolym. Orig. Res. Biomol.*, vol. 61, no. 1, pp. 3–31, 2001.
- [71] A. R. Orlando and G. P. Gallerano, “Terahertz radiation effects and biological applications,” *J. Infrared Millim. Terahertz Waves*, vol. 30, no. 12, pp. 1308–1318, 2009.
- [72] J. T. Brosnan and M. E. Brosnan, “The sulfur-containing amino acids: an overview,” *J. Nutr.*, vol. 136, no. 6, pp. 1636S-1640S, 2006.
- [73] M. C. Chen and R. C. Lord, “Laser-excited Raman spectroscopy of biomolecules. VIII. Conformational study of bovine serum albumin,” *J. Am. Chem. Soc.*, vol. 98, no. 4, pp. 990–992, 1976.
- [74] M. T. Devlin, G. Barany, and I. W. Levin, “Conformational properties of asymmetrically substituted mono-, di- and trisulfides: solid and liquid phase Raman spectra,” *J. Mol. Struct.*, vol. 238, pp. 119–137, 1990.
- [75] T. J. Thamann, “A vibrational spectroscopic assignment of the disulfide bridges in recombinant bovine growth hormone and growth hormone analogs,” *Spectrochim. Acta. A. Mol. Biomol. Spectrosc.*, vol. 55, no. 7–8, pp. 1661–1666, 1999.

- [76] A. Beneduci, K. Cosentino, and G. Chidichimo, “Millimeter wave radiations affect membrane hydration in phosphatidylcholine vesicles,” *Materials*, vol. 6, no. 7, pp. 2701–2712, 2013.
- [77] A. Beneduci, K. Cosentino, S. Romeo, R. Massa, and G. Chidichimo, “Effect of millimetre waves on phosphatidylcholine membrane models: a non-thermal mechanism of interaction,” *Soft Matter*, vol. 10, no. 30, pp. 5559–5567, 2014.
- [78] A. Beneduci, L. Filippelli, K. Cosentino, M. L. Calabrese, R. Massa, and G. Chidichimo, “Microwave induced shift of the main phase transition in phosphatidylcholine membranes,” *Bioelectrochemistry*, vol. 84, pp. 18–24, 2012.
- [79] M. Zhadobov, R. Sauleau, V. Vié, M. Himdi, L. Le Coq, and D. Thouroude, “Interactions between 60-GHz millimeter waves and artificial biological membranes: dependence on radiation parameters,” *IEEE Trans. Microw. Theory Tech.*, vol. 54, no. 6, pp. 2534–2542, 2006.
- [80] G. Konoplev *et al.*, “Label-Free Physical Techniques and Methodologies for Proteins Detection in Microfluidic Biosensor Structures,” *Biomedicines*, vol. 10, no. 2, p. 207, Jan. 2022, doi: 10.3390/biomedicines10020207.
- [81] R. A. Alahnomi *et al.*, “Review of Recent Microwave Planar Resonator-Based Sensors: Techniques of Complex Permittivity Extraction, Applications, Open Challenges and Future Research Directions,” *Sensors*, vol. 21, no. 7, p. 2267, Mar. 2021, doi: 10.3390/s21072267.
- [82] J. Muñoz-Enano, P. Vélez, M. Gil, and F. Martín, “Planar Microwave Resonant Sensors: A Review and Recent Developments,” *Appl. Sci.*, vol. 10, no. 7, p. 2615, Apr. 2020, doi: 10.3390/app10072615.
- [83] H. Wang *et al.*, “Recent progress in terahertz biosensors based on artificial electromagnetic subwavelength structure,” *TrAC Trends Anal. Chem.*, vol. 158, p. 116888, Jan. 2023, doi: 10.1016/j.trac.2022.116888.
- [84] W. Grundler and F. Keilmann, “Sharp resonances in yeast growth prove nonthermal sensitivity to microwaves,” *Phys. Rev. Lett.*, vol. 51, no. 13, p. 1214, 1983.
- [85] H. Fröhlich and F. Kremer, *Coherent excitations in biological systems*. Springer Science & Business Media, 2012.
- [86] A. Z. Smolyanskaya and R. L. Vilenskaya, “Effects of millimeter-band electromagnetic radiation on the functional activity of certain genetic elements of bacterial cells,” *Sov. Phys. USPEKHI*, vol. 16, no. 4, p. 571, 1974.
- [87] V. I. Fedorov and G. F. Bakharev, “Influence of THz radiation on early phase of seed germinating and yield of wheat,” in *ICONO 2010: International Conference*

- on Coherent and Nonlinear Optics*, International Society for Optics and Photonics, 2011, p. 799327.
- [88] S. Hadjiloucas, M. S. Chahal, and J. W. Bowen, “Preliminary results on the non-thermal effects of 200–350 GHz radiation on the growth rate of *S. cerevisiae* cells in microcolonies,” *Phys. Med. Biol.*, vol. 47, no. 21, p. 3831, 2002.
- [89] N. Y. Weisman, V. I. Fedorov, E. F. Nemova, and N. A. Nikolaev, “Survival and life span of *Drosophila melanogaster* in response to terahertz radiation,” *Adv. Gerontol.*, vol. 4, no. 3, pp. 187–192, 2014.
- [90] N. P. Bondar, I. L. Kovalenko, D. F. Avgustinovich, A. G. Khamoyan, and N. N. Kudryavtseva, “Behavioral effect of terahertz waves in male mice,” *Bull. Exp. Biol. Med.*, vol. 145, no. 4, pp. 401–405, 2008.
- [91] V. F. Kirichuk, N. V. Efimova, and E. V. Andronov, “Effect of high power terahertz irradiation on platelet aggregation and behavioral reactions of albino rats,” *Bull. Exp. Biol. Med.*, vol. 148, no. 5, p. 746, 2009.
- [92] V. Kirichuk, O. Antipova, and Y. A. Krylova, “Effect of continuous irradiation with terahertz electromagnetic waves of the NO frequency range on behavioral reactions of male albino rats under stress conditions,” *Bull. Exp. Biol. Med.*, vol. 157, no. 2, 2014.
- [93] G. P. Gallerano *et al.*, “THz-BRIDGE: an European project for the study of the interaction of terahertz radiation with biological systems,” in *Infrared and Millimeter Waves, Conference Digest of the 2004 Joint 29th International Conference on 2004 and 12th International Conference on Terahertz Electronics, 2004.*, IEEE, 2004, pp. 817–818.
- [94] S. F. Boev *et al.*, “A Study of the Effect of Terahertz Electromagnetic Radiation on Microbial Cell Viability,” *Biophysics*, vol. 64, no. 3, pp. 416–423, May 2019, doi: 10.1134/S0006350919030059.
- [95] O. P. Cherkasova *et al.*, “Cellular effects of terahertz waves,” *J. Biomed. Opt.*, vol. 26, no. 09, Sep. 2021, doi: 10.1117/1.JBO.26.9.090902.
- [96] Junji Miyakoshi, “Cellular and Molecular Responses to Radio-Frequency Electromagnetic Fields,” *Proc. IEEE*, vol. 101, no. 6, pp. 1494–1502, Jun. 2013, doi: 10.1109/JPROC.2013.2248111.
- [97] S. Mohammadi, A. V. Nadaraja, K. Luckasavitch, M. C. Jain, D. J. Roberts, and M. H. Zarifi, “A Label-Free, Non-Intrusive, and Rapid Monitoring of Bacterial Growth on Solid Medium Using Microwave Biosensor,” *IEEE Trans. Biomed. Circuits Syst.*, vol. 14, no. 1, pp. 2–11, Feb. 2020, doi: 10.1109/TBCAS.2019.2952841.

- [98] A. A. Abduljabar, D. J. Rowe, A. Porch, and D. A. Barrow, "Novel Microwave Microfluidic Sensor Using a Microstrip Split-Ring Resonator," *IEEE Trans. Microw. Theory Tech.*, vol. 62, no. 3, pp. 679–688, Mar. 2014, doi: 10.1109/TMTT.2014.2300066.
- [99] K. Wadhvani, S. Hussaini, A. Mazumder, and A. Syed, "Solvent-Based Optimization of CSRR and IDC RF Bio-Sensors," *IEEE Sens. J.*, vol. 22, no. 6, pp. 5651–5661, Mar. 2022, doi: 10.1109/JSEN.2022.3148349.
- [100] A. Kandwal *et al.*, "Highly Sensitive Closed Loop Enclosed Split Ring Biosensor With High Field Confinement for Aqueous and Blood-Glucose Measurements," *Sci. Rep.*, vol. 10, no. 1, p. 4081, Dec. 2020, doi: 10.1038/s41598-020-60806-9.
- [101] T. Chretiennot, D. Dubuc, and K. Grenier, "A Microwave and Microfluidic Planar Resonator for Efficient and Accurate Complex Permittivity Characterization of Aqueous Solutions," *IEEE Trans. Microw. Theory Tech.*, vol. 61, no. 2, pp. 972–978, Feb. 2013, doi: 10.1109/TMTT.2012.2231877.
- [102] M. L. Pall, "Millimeter (MM) wave and microwave frequency radiation produce deeply penetrating effects: the biology and the physics," *Rev. Environ. Health*, vol. 0, no. 0, p. 000010151520200165, May 2021, doi: 10.1515/reveh-2020-0165.
- [103] N. Vasilevskii, N. Suvorov, and M. Medvedeva, "Experimental analysis of biological effects of microwaves: their systemic, ultrastructural and neuronal mechanisms," *Gig. Sanit.*, no. 10, pp. 41–45, 1989.
- [104] A. Bryukhova and R. Vilenskaya, "Certain methodological problems and results of experimental investigation of the effects of microwaves on microorganisms and animals," *Sov. Phys. Uspekhi*, vol. 16, p. 569, 1973.
- [105] N. Zalyubovskaya, "Reactions of living organisms to exposure to millimeter-band electromagnetic waves," *Sov. Phys. Uspekhi*, vol. 16, no. 4, p. 574, 1974.
- [106] O. Betskii, N. Devyatkov, and V. Kislov, "Low intensity millimeter waves in medicine and biology," *Crit. Rev. Biomed. Eng.*, vol. 28, no. 1 & 2, 2000.
- [107] O. Betskii, N. Devyatkov, S. Pletnev, and V. Faikin, "Effect of low-energy and high-peak-power nanosecond pulses of microwave radiation on malignant tumors," *Crit. Rev. Biomed. Eng.*, vol. 29, no. 1, 2001.
- [108] N. Sinitsyn, V. Petrosyan, V. Yolkin, N. Devyatkov, Y. Gulyaev, and O. Betskii, "Special function of the" millimeter wavelength waves-aqueous medium" system in nature," *Crit. Rev. Biomed. Eng.*, vol. 28, no. 1 & 2, 2000.
- [109] S. Romanenko, P. H. Siegel, and V. Pikov, "Microdosimetry and physiological effects of millimeter wave irradiation in isolated neural ganglion preparation," presented at the 2013 International Kharkov Symposium on Physics and

- Engineering of Microwaves, Millimeter and Submillimeter Waves, IEEE, 2013, pp. 512–516.
- [110] S. Romanenko, P. H. Siegel, V. Pikov, and V. Wallace, “Alterations in neuronal action potential shape and spiking rate caused by pulsed 60 GHz millimeter wave radiation,” presented at the 2016 41st International Conference on Infrared, Millimeter, and Terahertz Waves (Irrmmw-Thz), IEEE, 2016, pp. 1–2.
- [111] K. Cosentino, A. Beneduci, A. Ramundo-Orlando, and G. Chidichimo, “The influence of millimeter waves on the physical properties of large and giant unilamellar vesicles,” *J. Biol. Phys.*, vol. 39, no. 3, pp. 395–410, 2013.
- [112] A. Ramundo-Orlando, F. Mattia, A. Palombo, and G. D’Inzeo, “Effect of low frequency, low amplitude magnetic fields on the permeability of cationic liposomes entrapping carbonic anhydrase: II. No evidence for surface enzyme involvement,” *Bioelectromagn. J. Bioelectromagn. Soc. Soc. Phys. Regul. Biol. Med. Eur. Bioelectromagn. Assoc.*, vol. 21, no. 7, pp. 499–507, 2000.
- [113] S. Romanenko, P. H. Siegel, D. A. Wagenaar, and V. Pikov, “Comparison of the effects of millimeter wave irradiation, general bath heating, and localized heating on neuronal activity in the leech ganglion,” presented at the Terahertz and Ultrashort Electromagnetic Pulses for Biomedical Applications, International Society for Optics and Photonics, 2013, p. 85850N.
- [114] R. K. Adair, “Biophysical limits on athermal effects of RF and microwave radiation,” *Bioelectromagn. J. Bioelectromagn. Soc. Soc. Phys. Regul. Biol. Med. Eur. Bioelectromagn. Assoc.*, vol. 24, no. 1, pp. 39–48, 2003.
- [115] A. G. Pakhomov, Y. Akyel, O. N. Pakhomova, B. E. Stuck, and M. R. Murphy, “Current state and implications of research on biological effects of millimeter waves: a review of the literature,” *Bioelectromagn. J. Bioelectromagn. Soc. Soc. Phys. Regul. Biol. Med. Eur. Bioelectromagn. Assoc.*, vol. 19, no. 7, pp. 393–413, 1998.
- [116] M. Zhadobov, N. Chahat, R. Sauleau, C. Le Quement, and Y. Le Drean, “Millimeter-wave interactions with the human body: state of knowledge and recent advances,” *Int. J. Microw. Wirel. Technol.*, vol. 3, no. 2, pp. 237–247, 2011.
- [117] D. Manna and R. Ghosh, “Effect of radiofrequency radiation in cultured mammalian cells: A review,” *Electromagn. Biol. Med.*, vol. 35, no. 3, pp. 265–301, 2016.
- [118] K. Hossmann and D. Hermann, “Effects of electromagnetic radiation of mobile phones on the central nervous system,” *Bioelectromagn. J. Bioelectromagn. Soc. Soc. Phys. Regul. Biol. Med. Eur. Bioelectromagn. Assoc.*, vol. 24, no. 1, pp. 49–62, 2003.

- [119] C. Haarala *et al.*, “Effect of a 902 MHz electromagnetic field emitted by mobile phones on human cognitive function: A replication study,” *Bioelectromagnetics*, vol. 24, no. 4, pp. 283–288, 2003.
- [120] C. L. Baird and D. G. Myszka, “Current and emerging commercial optical biosensors,” *J. Mol. Recognit.*, vol. 14, no. 5, pp. 261–268, 2001.
- [121] E. B. Bahadır and M. K. Sezgintürk, “Applications of commercial biosensors in clinical, food, environmental, and biothreat/biowarfare analyses,” *Anal. Biochem.*, vol. 478, pp. 107–120, 2015.
- [122] C. Jang, H.-J. Lee, and J.-G. Yook, “Radio-Frequency Biosensors for Real-Time and Continuous Glucose Detection,” *Sensors*, vol. 21, no. 5, p. 1843, Mar. 2021, doi: 10.3390/s21051843.
- [123] E. Silavwe, N. Somjit, and I. D. Robertson, “A Microfluidic-Integrated SIW Lab-on-Substrate Sensor for Microliter Liquid Characterization,” *IEEE Sens. J.*, vol. 16, no. 21, pp. 7628–7635, Nov. 2016, doi: 10.1109/JSEN.2016.2599099.
- [124] K. Grenier *et al.*, “Integrated Broadband Microwave and Microfluidic Sensor Dedicated to Bioengineering,” *IEEE Trans. Microw. Theory Tech.*, vol. 57, no. 12, pp. 3246–3253, Dec. 2009, doi: 10.1109/TMTT.2009.2034226.
- [125] Z. Wei *et al.*, “A High-Sensitivity Microfluidic Sensor Based on a Substrate Integrated Waveguide Re-Entrant Cavity for Complex Permittivity Measurement of Liquids,” *Sensors*, vol. 18, no. 11, p. 4005, Nov. 2018, doi: 10.3390/s18114005.
- [126] G. Rong, S. R. Corrie, and H. A. Clark, “In Vivo Biosensing: Progress and Perspectives,” *ACS Sens.*, vol. 2, no. 3, pp. 327–338, Mar. 2017, doi: 10.1021/acssensors.6b00834.
- [127] S. Guha, F. I. Jamal, and C. Wenger, “A Review on Passive and Integrated Near-Field Microwave Biosensors,” *Biosensors*, vol. 7, no. 4, p. 42, Sep. 2017, doi: 10.3390/bios7040042.
- [128] M. Pearson, D. Ewert, R. Striker, and B. Braaten, “Development Of A RF Biosensor Design To Detect Changes In Scattering Parameters Of Aqueous Materials During Radio Frequency Wave Exposure,” *Biomed. Sci. Instrum.*, vol. 57, no. 2, pp. 290–297, Apr. 2021, doi: 10.34107/YHPN9422.04290.
- [129] M. Godfrey, D. Ewert, R. Striker, and B. Braaten, “A Microstrip Transmission Line Biosensor to Measure the Interaction between Microliter Aqueous Solutions and 1.0–17.0 GHz Radio Frequencies,” *Sensors*, vol. 23, no. 11, p. 5193, May 2023, doi: 10.3390/s23115193.
- [130] “Mechanical and Laser Machining in One System LPKF ProtoMat D104,” LPKF Lasers & Electronics. Accessed: Mar. 22, 2023. [Online]. Available:

https://www.lpkf.com/fileadmin/mediafiles/user_upload/products/pdf/DQ/flyer_lpkf_protomat_d104_en.pdf

APPENDIX A. ADS TRANSMISSION LINE SIMULATION SOP

Created for Advanced Design System (ADS) 2017 Software

1. After opening the software package and arriving at the (Main) screen, click **File -> New -> Workspace**
2. In the **Name:** box, insert the desired name of your workspace. Then click the **Create Workspace** button.
3. In the first pop-up Wizard window choose **Standard ADS Layers, 0.0001 mil layout resolution** option. And click **Finish**. The workspace should appear as follows.

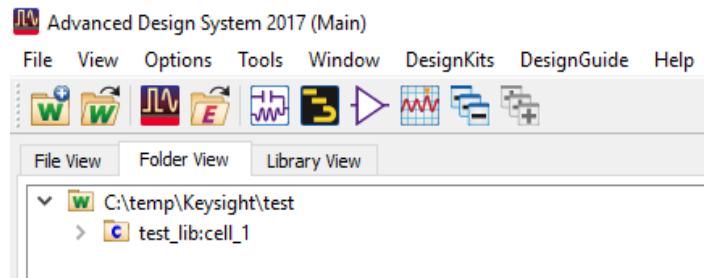





Figure A1. Screenshot of ADS main workspace screen.

4. On the top icon bar, choose the  button (New Schematic Window). Give it a name in the **Cell:** box and click **Create Schematic**.
5. This will prompt the schematic window to open.
6. In the part library, under **Simulation-S Param**, choose the part Term (Port Impedance for S-Parameters) and insert the part into the schematic workspace by clicking in the workspace. Put 2 Term parts in the workspace. Right-click and press **End Command** to stop inserting this part.
 - a. To create a matched load leave $Z = 50\Omega$. The coaxial cables used to connect the experimental setup are 50Ω . To create a mismatched load, $Z = 75\Omega$ was inputted as this is a standard impedance of other coaxial cables not used in this experiment.
7. Next, under the part library, **TLines-Microstrip**, choose the part **MLIN** (Libra Microstrip Line) and add it to the workspace by clicking inside the workspace. Again, **right-click** and choose **End Command** to stop inserting this part.
 - a. The characteristics of the microstrip line were assigned as follows:
 - i. Subst = "MSub1" (where the substrate "MSub1" will be created in a later step)
 - ii. $W = 0.8160\text{mm}$
 - iii. $L = 40.0\text{mm}$
8. Located on the top toolbar, the **INSERT GROUND**  button can be found. Add two grounds to this circuit.

9. To connect this circuit setup, on the top toolbar is the **Insert Wire**  button. To connect components simply click the red circle (or blue circle if ground component) on the edge of one component and then click the red circle on the edge of the other component. When finished connecting the circuit as desired, **right-click** and choose **End Command** to stop inserting more wire.
10. To designate the characteristics of the substrate, go under the **TLines - Microstrip** library and insert the **MSub** (Microstrip Substrate) part. The parameters for this substrate are
 - a. $H = 1\text{mm}$
 - b. $\epsilon_r = 4.7$
 - c. $\mu_r = 1$
 - d. $\text{Cond} = 4.17\text{e}7$
 - e. $H_u = 3.93701\text{e}+34\text{ mil}$
 - f. $T = 17.5\text{ um}$
 - g. $\text{TanD} = 0.002$
 - h. $\text{Rough} = 0\text{mm}$
 - i. $\text{Bbase} =$
 - j. $\text{Dpeaks} =$

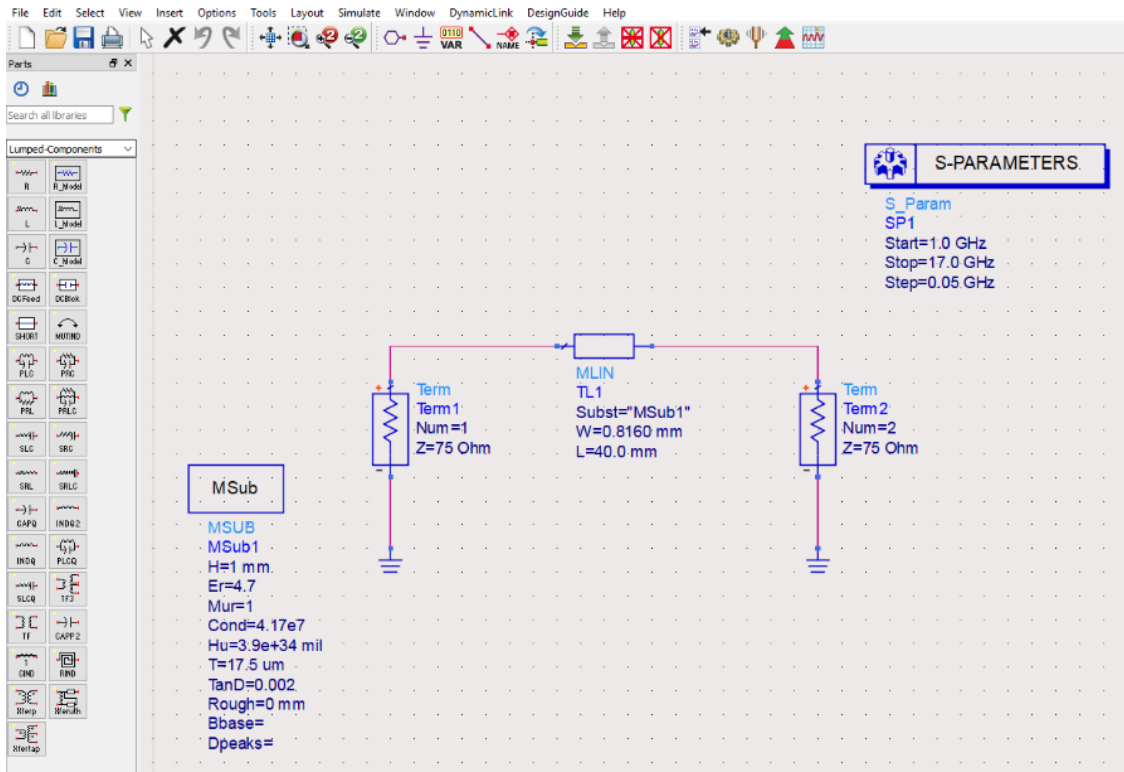


Figure A2. The finished 75Ω transmission line model in ADS workspace.

11. In the (Main) window, go under the **Layout** menu and click **Generate/Update Layout**. This will cause the Layout window to pop up with a 2D model of the circuit as a transmission line.
12. The Layout window will display the designed transmission line. The first task will be to create the substrate layer. To start this, click **EM -> Substrate** on the top toolbar. A popup box will appear saying “No substrate found” click OK.
13. A second pop-up box will appear asking what to name the file of the new substrate. Type in a file name and hit **Create Substrate**.
14. In the Substrate Creation window, the desired layers can be assigned. For this simulation, Rogers TMM4 (E= 4.7) is the substrate of choice. It will have two conductor layers with the inside being ceramic.
15. Leave layer 1, as the dielectric AIR, layer 2, as the Conductor Layer, cond(1). Set Conductor Layer Thickness to 0.0175mm and material to copper.
16. In Layer 3 we will input the material properties for Rogers TMM4. Under Layer 3, click on the Dielectric, under Type, and click the ... on the popup, next to Material. A second popup will appear, Under the **Dielectrics** tab, click Add Dielectric. Material Name, TMM4, Real, 4.7, Hit Ok.
17. Going back to the sidebar, under **Material**, choose the newly assigned material, TMM4. Assign Thickness to be 1.0mm.
18. Right-click, Cover, and click **Insert Substrate Layer Above**.
19. Assign the newly formed Dielectric Layer Material to be AIR and a Thickness of 0.0 mm.
20. Right-click on the **Cover layer** and click **Delete Cover**.
21. Next, right-click on the bottom conductor layer, on the 3D graphic. Click **Map Conductor Layer**. A cond(2) should appear in the 3D graphic, and a second Conductor Layer will appear in the Substrate Layer Stackup. Set Conductor Layer Thickness to 0.0175mm and material to copper.
22. Finally, click **Save** to save the Substrate Layer Design. And minimize this window.
23. In the Layout Window, click **Insert Pin**. Assign Pin 1 on the left side of the TL, and insert Pin 2 on the right side of the TL making sure, the Layer (on the Properties bar on the right-hand side) is set to Layer **cond:drawing**. Click the corresponding blue dots to insert each pin.
24. Assign Pin 3 on the left side of the TL, and insert Pin 4 on the right side of the TL making sure, the Layer (on the Properties bar on the right-hand side) is set to Layer **cond2:drawing**. Close the Insert Pin window popup.
25. Open **EM -> Port Editor**.
26. Under Number 3, click the red plus symbol P3 and drag it to the black minus symbol under number 1. This will make P1 (+) and P3 (-). Repeat for number 4. Making P2 (+) and P4 (-).

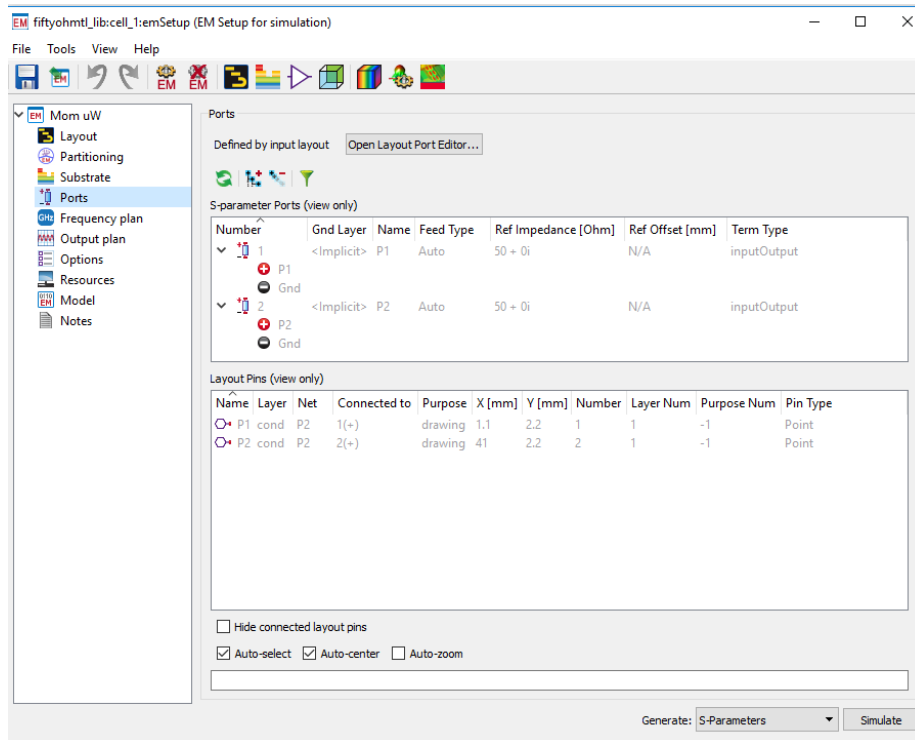


Figure A3. Assigning a 2-Port system and frequency setup in ADS for the 50Ω transmission line model.

27. Open **EM** -> **Simulations Settings**. A popup should appear. Click **Create EM Setup View**. Here we can set our frequency sweep, under **Frequency Plan**. Choose Type, Linear, Fstart 1.0 GHz, Fstop 17 GHz, Step 0.05GHz. Click the **Save** button and close the window.
28. Finally, click **EM** -> **Simulate**. A simulation progress window will pop up. Wait for the simulation to finish.
29. When the simulation has finished, the Status Message will read “Job Finished” and the Data Display window will appear.
30. The data from the simulation can be plotted in numerous ways, by clicking on the plot buttons. We will use the **Rectangular Plot** to plot the S21 and S11 results of the design.

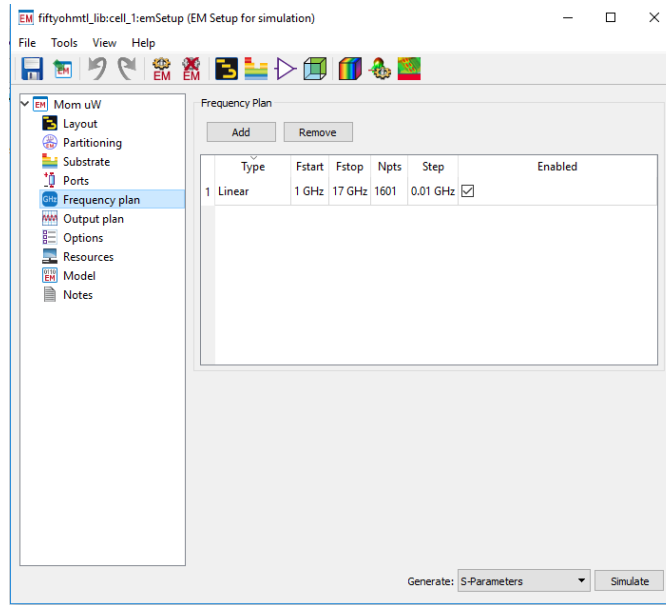


Figure A4. Assigning a 1.0-17.0 GHz frequency sweep for the 50Ω transmission line model.

31. In the pop-up window, click the **Rectangular Plot** button and click to insert the window. Click S(2,1) and any other data of interest.

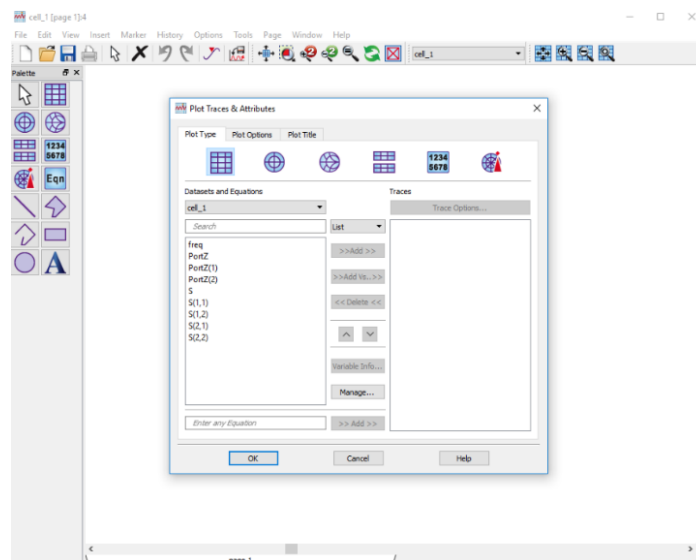


Figure A5. Selecting a rectangular plot for S₂₁ data or any S-parameter of interest.

APPENDIX B. HFSS TRANSMISSION LINE SIMULATION SOP

Created for Ansys HFSS – Electronics Desktop software 2021

1. Open a new “Insert HFSS design”
2. **HFSS -> Solution Type -> Terminal -> Ok**
3. Click **Draw** box and sketch a box
4. Double click on **Box 1**. Name it “substrate,” change color, material “Rogers TMM4,” and transparency (if desired) -> hit **Ok**
5. Double-click **Create Box**

Position: -15, -15, 0 mm

Xsize: 30mm

Ysize: 30mm

Zsize: 1mm

6. Click the **Draw** box. Name “trace,” change color, material “copper”
7. Double-click **Create Box**

Position: -15, -0.9, 1 mm

Xsize: 30mm

Ysize: 1.8mm

Zsize: 0.0175mm

8. Click the **Draw** box. Name “ground,” change color, material “copper”
9. Double-click **Create Box**

Position: -15, -15, 0 mm

Xsize: 30mm

Ysize: 30mm

Zsize: 0.0175mm

10. Right Click -> **Select Edges**-> select the edge of your copper trace -> hold the control key -> select the edge of the substrate.
11. **Modeler** ->**Edge**-> **CreateObjectfromEdge**. Select both new lines (first select trace line and then select substrate line) -> **Draw** -> **Sweep** -> **AlongPath** -> **Ok**
12. Double click on the new object and rename “P1”, change color if desired.
13. Select the face of “P1” and right-click -> **Assign Excitation** -> **Lumped Port** -> **Use Conducting Plane**. Then check Ground, Use as Reference.
14. Repeat steps 10-13 to make port 2 “P2.”
15. Click the **Draw** box. Rename “well,” material “vacuum,” change color
16. Double-click **Create Box**

Position: -15, -5, 0.75 mm

Xsize: 30mm

Ysize: 1.8mm

Zsize: 0.25mm
17. Select “substrate” and “well” and click **subtract** button. Substrate – Well -> **Ok**. This will create one unified shape.
18. *Note: we want to keep some side on the well so that the liquid does not come out. So, if you already subtracted substrate from the well, then add two sides. Click **Rectangle** and draw a rectangle.

Side 1

Position: -15, -5, 0.75

Axis: X

Ysize: 1.8 mm

Zsize: 0.25 mm

Side 2

Position: 15, -5, 0.75

Axis: X

Ysize: 1.8 mm

Zsize: 0.25 mm

19. Next, we need to set boundary conditions. Click on the ground face. Right click -> **Assign Boundary** -> **Perfect E** -> name it -> **Ok**
20. Select the copper trace. Right click -> **Assign Boundary** -> **Finite Conductivity** -> name it -> check **use material** -> click **vacuum** -> search: copper -> **Ok**
21. Assign boundary conditions to top substrate faces by selecting them with the control key. Right click -> **Assign Boundary** -> **Perfect E**-> name it -> **Ok**
22. Add air volume. Click **Region** (under **Draw**) -> **Absolute Offset** -> 10 mm-> **In all directions** -> **Ok**
23. Right-click -> Select **AllObjectFaces** -> right click -> **Assign Boundary Conditions** -> **Radiation** -> **OK**
24. Right-click **Analysis** -> **Add Solution Setup** -> change frequency, delta S, and any other parameters as needed/wanted -> **Ok**
25. Right-click **Setup1** -> **Add frequency sweep** -> **Linear Step** and change the start and end frequency and step size.
26. Click **Validation**
27. Click **Analyze All**. The simulation will run now, and you can analyze the results after the simulation is complete.

APPENDIX C. RF BIOSENSOR MEASUREMENT SOP

There are two parts to preparing the E5071C VNA machine for collecting experimental data. The first is to perform a full calibration using Keysight's Full 2-Port Calibration manual and 85052D Calibration kit.

Part A:

1. Connect a 50 Ω coax cable to Port 1 and another to Port 2 of the VNA.
2. Follow instructions in calibration manual using the short, open, matched loads of the 85052D Calibration kit. **Note:** When performing Thru calibration step, connect the RF biosensor between Ports 1 and 2 via the 50 Ω coax cables and secure the cables to a level surface. This is to reduce any movement of cables and the biosensor after calibration.

Part B:

The second part is to set up the E5071C VNA settings and connect equipment for the experiment.

1. Leaving the RF biosensor secured to a level surface and connected to the 50 Ω coax cables, input the following sweep setting on the VNA:

Frequency Sweep: 1.0 - 17.0 GHz

Data Points: 1601

Input Power Level: -5 dB

Measure S_{11} and S_{21} in logarithmic magnitude (dB) and extended phase (degrees)

2. Load 'Agilent' automatic sweep saving script received from Agilent.
3. Insert a flash drive to save all .s2p (Touchstone) files off machine.
4. First, the interaction (in S-parameters (dB) and extended phase (degrees) were measured for the well left empty (air-filled). 4 sets of 10 sweeps (40 sweeps total) were collected and saved to the flash drive.
5. Then using a micropipette, 15 μ L of aqueous MUTs at room temperature, \sim 21 $^{\circ}$ C were loaded into the well.

6. The sweep button was pushed on the script prompt window and a set of 10 frequency sweeps were measured and saved as .s2p files on the flash drive.
7. In between sweep sets, the MUT was removed using a Kimtech wipe and the well was allowed ~1 minute to completely dry before reloading the well.
8. This process was repeated for each MUT until 4 sets of 10 sweeps (40 sweeps total) were collected and saved to the flash drive. If varying the MUT type, 70% ethanol spray was used to clean the RF biosensor in between experimental sets.

APPENDIX D. MATLAB EXAMPLE CODE FOR S-PARAMETER TO VOLTAGE

RATIO CONVERSIONS

```
% Importing frequency data
F = readtable('empty_set1_sweep1.csv', 'HeaderLines',1); frequency = F{:,1};

% Importing S21 and S11 magnitude data - Sweep 1
empty_set1_sweep1 = readtable('empty_set1_sweep1.csv', 'HeaderLines',1);
empty_set1_s11_sweep1= empty_set1_sweep1{:,2}; empty_set1_s21_sweep1=
empty_set1_sweep1 {:,4};

% Importing S21 and S11 magnitude data -Sweep 2
empty_set1_sweep2 = readtable('empty_set1_sweep2.csv', 'HeaderLines',1);
empty_set1_s11_sweep2= empty_set1_sweep2{:,2}; empty_set1_s21_sweep2=
empty_set1_sweep2 {:,4};

% Importing S21 and S11 magnitude data -Sweep 3
empty_set1_sweep3 = readtable('empty_set1_sweep3.csv', 'HeaderLines',1);
empty_set1_s11_sweep3= empty_set1_sweep3{:,2}; empty_set1_s21_sweep3=
empty_set1_sweep3 {:,4};

%% % Plotting raw dB data - From Set 1 (sweep 1-3) and importing sweeps 1-3 into a
single matrix
plot(frequency, empty_set1_s21_sweep1, frequency, empty_set1_s21_sweep2, frequency,
empty_set1_s21_sweep3);

xlabel('Frequency (GHz)') % X-axis label
ylabel('S21 Parameters (dB)') % Y-axis label
title('Experimental Empty S21 Sweeps 1-3') % Title of the plot
    axis on
    grid on
legend('Sweep 1', ' Sweep 2', 'Sweep 3')

%% % Compile a single, full matrix of 3 sweeps of 30 data points
empty_s21_set_1 = [empty_set1_s21_sweep1, empty_set1_s21_sweep2,
empty_set1_s21_sweep3];

%% % Converting empty well (filled with air) data from dB to voltage ratio (VR)
empty_s21_VR = 10.^(empty_s21_set_1 ./ 20); % Convert to VR
empty_s21_VR_mag = abs(empty_s21_VR); % Calculate magnitude
empty_Mean_All_Sets_VR = mean(empty_s21_VR_mag'); % Calculate point-by-point mean
std_empty_s21_VR = std(empty_s21_VR_mag); % Calculate standard deviation
upper_envelope_empty_s21_VR = 3* std_empty_s21_VR; % Calculate upper envelope bound
lower_envelope_empty_s21_VR = -3* std_empty_s21_VR; % Calculate lower envelope bound.
standard_error_empty_s21 = std(empty_s21_VR_mag')/sqrt(3); % Calculate standard error

%% % Plotting empty well data with standard error bars
    hold on
errorbar(frequency, empty_Mean_All_Sets_VR, standard_error_empty_s21)
title('Empty Well Full Set (Mean and St. Error Bars)')
xlabel('Frequency (GHz)');
ylabel('Voltage Ratio (unitless (V2/V1))');
legend('Empty Well Mean w/ St. Error')
```

```

grid on
axis on

%% % Find absolute average error
empty_absavgerror = abs(mean(standard_error_empty_s21));

%% % Calculate relative standard error
min_absoluteerror = min(standard_error_empty_s21); %find min RSE
%Now need to find the buffer population mean at this same point in the frequency
sweep
%Will find out which column the min occurs at so we can look up that column
%and know the population mean value and frequency that it occurs at too.
[a] = min_absoluteerror;
column_min = find(standard_error_empty_s21==a);
mean_empty_full_population_min = empty_Mean_All_Sets_VR(column_min);
minRSEinpercent = ((min_absoluteerror) ./ (mean_empty_full_population_min))*100

% Repeat process to find maximum SE value.
max_absoluteerror = max(standard_error_empty_s21); %find max RSE
%Now need to find the buffer population mean at this same point in the frequency
sweep
[b] = max_absoluteerror;
column_max = find(standard_error_empty_s21==b);
mean_empty_full_population_max = empty_Mean_All_Sets_VR(column_max);
maxRSEinpercent = ((max_absoluteerror) ./ (mean_empty_full_population_max))*100

```

APPENDIX E. SAMPLE DATA FOR TESTING MATLAB CODE

Sample data from file saved as “empty_set1_sweep1.csv”

Frequency	Tr1_S11_Real	Tr1_S11_Imag	Tr2_S21_Real	Tr2_S21_Imag
1.00E+09	-1.23E+01	0.00E+00	-2.76E-01	0.00E+00
1.01E+09	-1.23E+01	0.00E+00	-2.72E-01	0.00E+00
1.02E+09	-1.23E+01	0.00E+00	-2.70E-01	0.00E+00
1.03E+09	-1.23E+01	0.00E+00	-2.60E-01	0.00E+00
1.04E+09	-1.23E+01	0.00E+00	-2.42E-01	0.00E+00
1.05E+09	-1.24E+01	0.00E+00	-2.31E-01	0.00E+00
1.06E+09	-1.24E+01	0.00E+00	-2.14E-01	0.00E+00
1.07E+09	-1.24E+01	0.00E+00	-2.06E-01	0.00E+00
1.08E+09	-1.24E+01	0.00E+00	-2.05E-01	0.00E+00
1.09E+09	-1.24E+01	0.00E+00	-2.12E-01	0.00E+00
1.10E+09	-1.24E+01	0.00E+00	-2.30E-01	0.00E+00
1.11E+09	-1.23E+01	0.00E+00	-2.59E-01	0.00E+00
1.12E+09	-1.24E+01	0.00E+00	-2.90E-01	0.00E+00
1.13E+09	-1.24E+01	0.00E+00	-3.23E-01	0.00E+00
1.14E+09	-1.24E+01	0.00E+00	-3.54E-01	0.00E+00
1.15E+09	-1.24E+01	0.00E+00	-3.76E-01	0.00E+00
1.16E+09	-1.24E+01	0.00E+00	-3.91E-01	0.00E+00
1.17E+09	-1.25E+01	0.00E+00	-3.88E-01	0.00E+00
1.18E+09	-1.25E+01	0.00E+00	-3.67E-01	0.00E+00
1.19E+09	-1.25E+01	0.00E+00	-3.33E-01	0.00E+00
1.20E+09	-1.26E+01	0.00E+00	-2.90E-01	0.00E+00
1.21E+09	-1.26E+01	0.00E+00	-2.41E-01	0.00E+00
1.22E+09	-1.26E+01	0.00E+00	-1.99E-01	0.00E+00
1.23E+09	-1.26E+01	0.00E+00	-1.69E-01	0.00E+00
1.24E+09	-1.27E+01	0.00E+00	-1.54E-01	0.00E+00
1.25E+09	-1.27E+01	0.00E+00	-1.69E-01	0.00E+00
1.26E+09	-1.28E+01	0.00E+00	-2.00E-01	0.00E+00
1.27E+09	-1.28E+01	0.00E+00	-2.49E-01	0.00E+00
1.28E+09	-1.29E+01	0.00E+00	-3.04E-01	0.00E+00
1.29E+09	-1.29E+01	0.00E+00	-3.60E-01	0.00E+00

Sample data from file saved as “empty_set1_sweep2.csv”

Frequency	Tr1_S11_Real	Tr1_S11_Imag	Tr2_S21_Real	Tr2_S21_Imag
1.00E+09	-1.23E+01	0.00E+00	-2.77E-01	0.00E+00
1.01E+09	-1.23E+01	0.00E+00	-2.74E-01	0.00E+00
1.02E+09	-1.23E+01	0.00E+00	-2.70E-01	0.00E+00
1.03E+09	-1.23E+01	0.00E+00	-2.61E-01	0.00E+00
1.04E+09	-1.23E+01	0.00E+00	-2.46E-01	0.00E+00
1.05E+09	-1.23E+01	0.00E+00	-2.32E-01	0.00E+00
1.06E+09	-1.24E+01	0.00E+00	-2.15E-01	0.00E+00
1.07E+09	-1.24E+01	0.00E+00	-2.05E-01	0.00E+00
1.08E+09	-1.24E+01	0.00E+00	-2.05E-01	0.00E+00
1.09E+09	-1.23E+01	0.00E+00	-2.14E-01	0.00E+00
1.10E+09	-1.24E+01	0.00E+00	-2.32E-01	0.00E+00
1.11E+09	-1.23E+01	0.00E+00	-2.59E-01	0.00E+00
1.12E+09	-1.24E+01	0.00E+00	-2.91E-01	0.00E+00
1.13E+09	-1.24E+01	0.00E+00	-3.27E-01	0.00E+00
1.14E+09	-1.24E+01	0.00E+00	-3.54E-01	0.00E+00
1.15E+09	-1.24E+01	0.00E+00	-3.77E-01	0.00E+00
1.16E+09	-1.24E+01	0.00E+00	-3.91E-01	0.00E+00
1.17E+09	-1.25E+01	0.00E+00	-3.85E-01	0.00E+00
1.18E+09	-1.25E+01	0.00E+00	-3.66E-01	0.00E+00
1.19E+09	-1.25E+01	0.00E+00	-3.33E-01	0.00E+00
1.20E+09	-1.26E+01	0.00E+00	-2.92E-01	0.00E+00
1.21E+09	-1.26E+01	0.00E+00	-2.40E-01	0.00E+00
1.22E+09	-1.26E+01	0.00E+00	-1.98E-01	0.00E+00
1.23E+09	-1.26E+01	0.00E+00	-1.69E-01	0.00E+00
1.24E+09	-1.27E+01	0.00E+00	-1.53E-01	0.00E+00
1.25E+09	-1.27E+01	0.00E+00	-1.66E-01	0.00E+00
1.26E+09	-1.28E+01	0.00E+00	-2.00E-01	0.00E+00
1.27E+09	-1.28E+01	0.00E+00	-2.51E-01	0.00E+00
1.28E+09	-1.29E+01	0.00E+00	-3.06E-01	0.00E+00
1.29E+09	-1.29E+01	0.00E+00	-3.60E-01	0.00E+00

Sample data from file saved as “empty_set1_sweep3.csv”

Frequency	Tr1_S11_Real	Tr1_S11_Imag	Tr2_S21_Real	Tr2_S21_Imag
1.00E+09	-1.23E+01	0.00E+00	-2.76E-01	0.00E+00
1.01E+09	-1.23E+01	0.00E+00	-2.73E-01	0.00E+00
1.02E+09	-1.23E+01	0.00E+00	-2.71E-01	0.00E+00
1.03E+09	-1.23E+01	0.00E+00	-2.61E-01	0.00E+00
1.04E+09	-1.23E+01	0.00E+00	-2.43E-01	0.00E+00
1.05E+09	-1.24E+01	0.00E+00	-2.31E-01	0.00E+00
1.06E+09	-1.24E+01	0.00E+00	-2.16E-01	0.00E+00
1.07E+09	-1.23E+01	0.00E+00	-2.06E-01	0.00E+00
1.08E+09	-1.24E+01	0.00E+00	-2.04E-01	0.00E+00
1.09E+09	-1.24E+01	0.00E+00	-2.14E-01	0.00E+00
1.10E+09	-1.24E+01	0.00E+00	-2.32E-01	0.00E+00
1.11E+09	-1.23E+01	0.00E+00	-2.62E-01	0.00E+00
1.12E+09	-1.24E+01	0.00E+00	-2.92E-01	0.00E+00
1.13E+09	-1.24E+01	0.00E+00	-3.23E-01	0.00E+00
1.14E+09	-1.24E+01	0.00E+00	-3.54E-01	0.00E+00
1.15E+09	-1.24E+01	0.00E+00	-3.76E-01	0.00E+00
1.16E+09	-1.24E+01	0.00E+00	-3.91E-01	0.00E+00
1.17E+09	-1.25E+01	0.00E+00	-3.87E-01	0.00E+00
1.18E+09	-1.25E+01	0.00E+00	-3.67E-01	0.00E+00
1.19E+09	-1.25E+01	0.00E+00	-3.34E-01	0.00E+00
1.20E+09	-1.26E+01	0.00E+00	-2.90E-01	0.00E+00
1.21E+09	-1.26E+01	0.00E+00	-2.43E-01	0.00E+00
1.22E+09	-1.26E+01	0.00E+00	-1.98E-01	0.00E+00
1.23E+09	-1.26E+01	0.00E+00	-1.70E-01	0.00E+00
1.24E+09	-1.27E+01	0.00E+00	-1.52E-01	0.00E+00
1.25E+09	-1.27E+01	0.00E+00	-1.68E-01	0.00E+00
1.26E+09	-1.28E+01	0.00E+00	-1.99E-01	0.00E+00
1.27E+09	-1.28E+01	0.00E+00	-2.50E-01	0.00E+00
1.28E+09	-1.29E+01	0.00E+00	-3.05E-01	0.00E+00
1.29E+09	-1.29E+01	0.00E+00	-3.60E-01	0.00E+00

APPENDIX F. COMPARISON OF HAND CALCULATIONS VERSUS MATLAB SCRIPT ON STATISTICAL ANALYSIS

Below is a worked-out hand calculation versus MATLAB calculation proving the MATLAB script (sample in Appendix D) runs as expected for voltage ratio, standard deviation, and error calculations. The following steps were taken to import and convert data from S-parameters (dB) to voltage ratio and perform statistical analysis. For this example, 3 sweeps with 4 data points will be used for ease of hand calculations.

Steps A-I

A. Read in experimental data (dB)

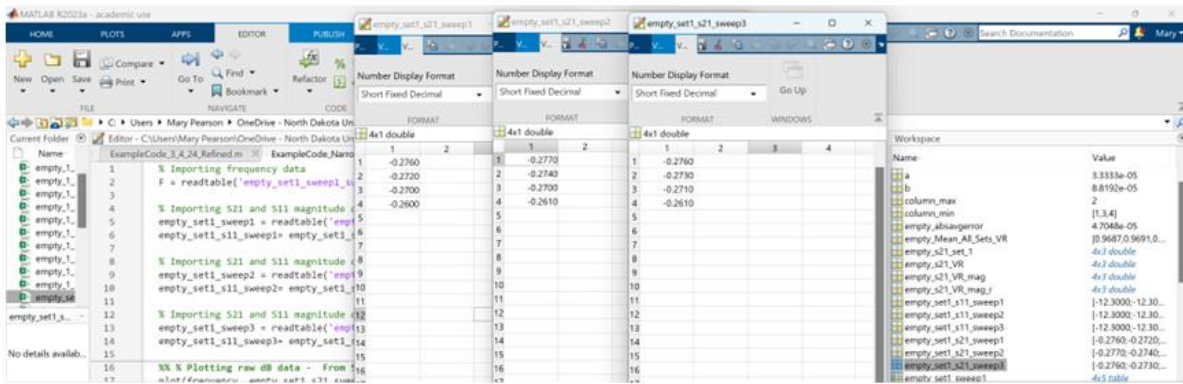
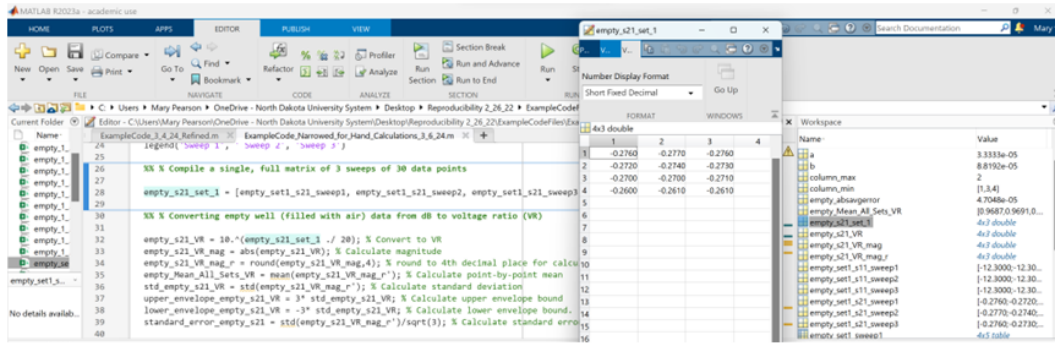


Figure F1. Screenshot verifying MATLAB imported experimental data as expected.

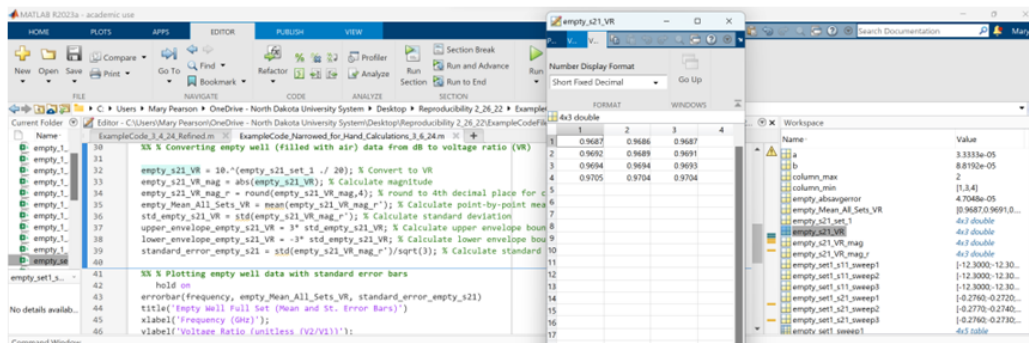
B. Converge all 3 sweeps into one 4x3 matrix



Sweep 1	Sweep 2	Sweep 3
-0.2760	-0.2770	-0.2760
-0.2720	-0.2740	-0.2730
-0.2700	-0.2700	-0.2710
-0.2600	-0.2610	-0.2610

Figure F2. Screenshot verifying MATLAB result matches data combined into a table.

C. Convert dB to voltage ratio ($\frac{V_2^+}{V_1^-}$)

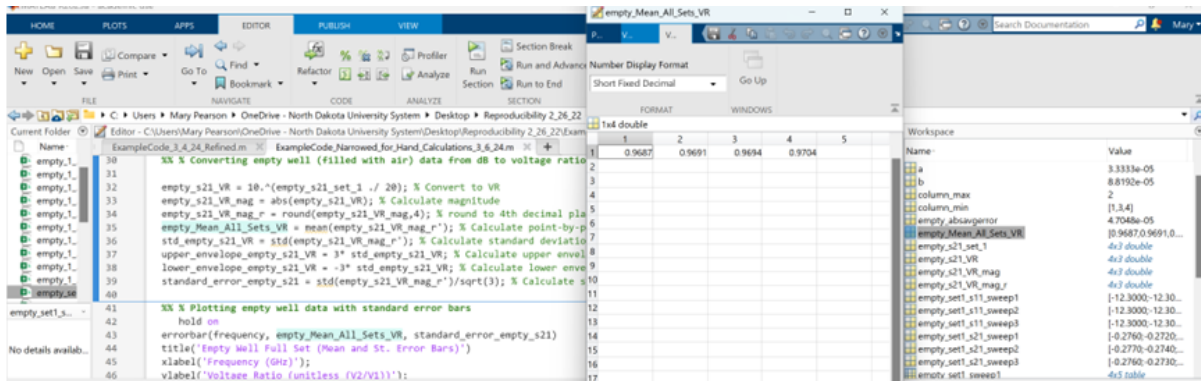


Using the following equation: $\frac{V_2^+}{V_1^-} = 10^{\frac{dB}{20}}$

Frequency Point	Sweep 1	Sweep 2	Sweep 3
freq1	0.9687	0.9686	0.9687
freq2	0.9692	0.9689	0.9691
freq3	0.9694	0.9694	0.9693
freq4	0.9705	0.9704	0.9704

Figure F3. Screenshot verifying MATLAB result of dB conversion to voltage ratio values in comparison to hand calculations located in table.

D. Calculate point-by-point mean of the 4x3 matrix

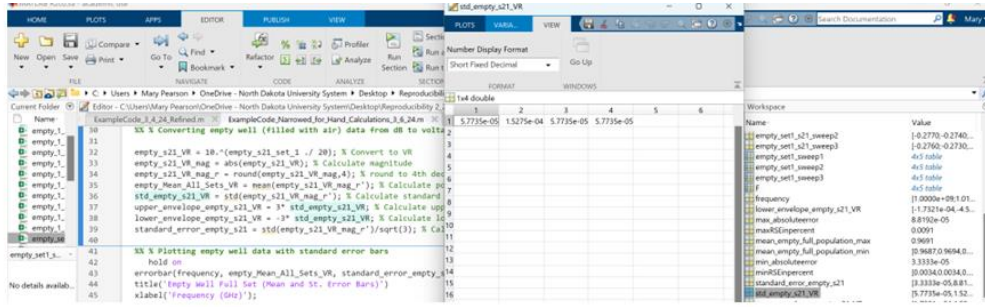


$$mean = \frac{\sum(x)}{n}$$

mean@freq1	$\frac{(0.9687 + 0.9686 + 0.9687)}{3}$	0.9687
mean@freq2	$\frac{(0.9692 + 0.9689 + 0.9691)}{3}$	0.9691
mean@freq3	$\frac{(0.9694 + 0.9694 + 0.9693)}{3}$	0.9694
mean@freq4	$\frac{(0.9705 + 0.9704 + 0.9704)}{3}$	0.9704

Figure F4. Screenshot verifying MATLAB result of point-by-point mean calculation in comparison to hand calculations located in table.

E. Calculate standard deviation of the 4x3 matrix

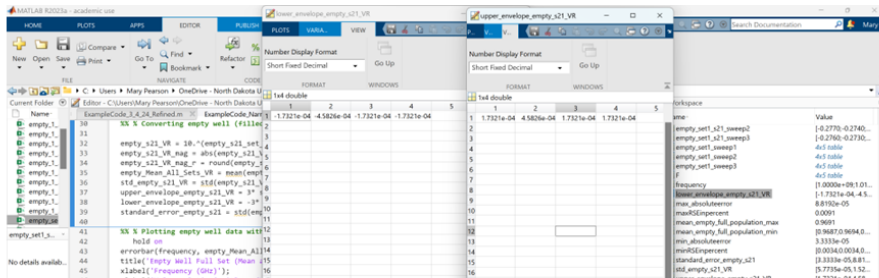


$$SD = \sqrt{\frac{\sum(x_i - \text{mean})^2}{n}}$$

stdev@freq1	$\sqrt{\frac{(0.9687+0.9687)^2}{3}} + \sqrt{\frac{(0.9686-0.9687)^2}{3}} + \sqrt{\frac{(0.9687-0.9687)^2}{3}}$	5.7735e-05
stdev@freq2	$\sqrt{\frac{(0.9692-0.9691)^2}{3}} + \sqrt{\frac{(0.9689-0.9691)^2}{3}} + \sqrt{\frac{(0.9691-0.9691)^2}{3}}$	1.732e-04
stdev@freq3	$\sqrt{\frac{(0.9694-0.9694)^2}{3}} + \sqrt{\frac{(0.9694-0.9694)^2}{3}} + \sqrt{\frac{(0.9693-0.9694)^2}{3}}$	5.7735e-05
stdev@freq4	$\sqrt{\frac{(0.9705-0.9704)^2}{3}} + \sqrt{\frac{(0.9704-0.9704)^2}{3}} + \sqrt{\frac{(0.9704-0.9704)^2}{3}}$	5.7735e-05

Figure F5. Screenshot verifying MATLAB result of standard deviation calculation in comparison to hand calculations located in table.

F. Calculate 99.5% confidence envelope of 3 sweep dataset by finding +/- 3 standard deviations of the 4x3 matrix

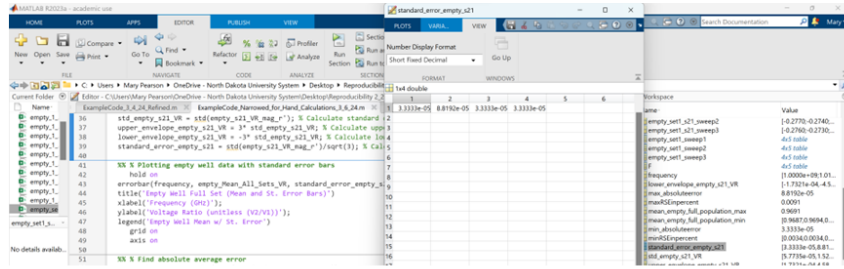


$$99.5\% \text{ CE} = \text{mean} \pm 3(\text{standard deviation})$$

Frequency Point	Upper CE bound	Lower CE Bound
@freq1	$(5.7735e-05 \cdot 3) = 1.732e-04$	$(5.7735e-05 \cdot -3) = -1.732e-04$
@freq2	$(1.732e-04 \cdot 3) = 5.196e-04$	$(1.732e-04 \cdot -3) = -5.196e-04$
@freq3	$(5.7735e-05 \cdot 3) = 1.732e-04$	$(5.7735e-05 \cdot -3) = -1.732e-04$
@freq4	$(5.7735e-05 \cdot 3) = 1.732e-04$	$(5.7735e-05 \cdot -3) = -1.732e-04$

Figure F6. Screenshot verifying MATLAB result of 99.5% confidence envelope calculation in comparison to hand calculations located in table.

G. Calculate standard error of the 4x3 matrix

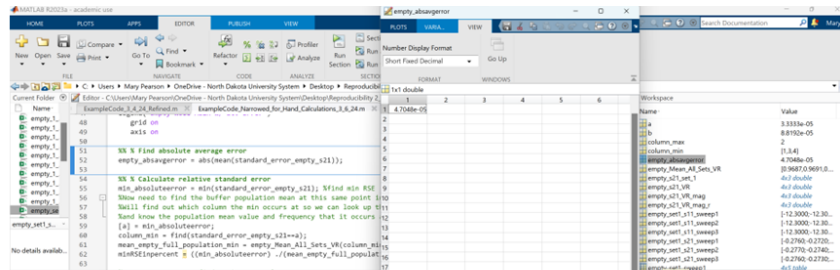


$$SE = \frac{\text{standard deviation}}{\sqrt{n}}$$

Frequency Point	SE
@freq1	$\frac{5.7735e-05}{\sqrt{3}} = 3.3333e-05$
@freq2	$\frac{1.732e-04}{\sqrt{3}} = 9.9999e-05$
@freq3	$\frac{5.7735e-05}{\sqrt{3}} = 3.3333e-05$
@freq4	$\frac{5.7735e-05}{\sqrt{3}} = 3.3333e-05$

Figure F7. Screenshot verifying MATLAB result of standard error calculation in comparison to hand calculations located in table.

H. Calculate absolute average error of the 4x3 matrix

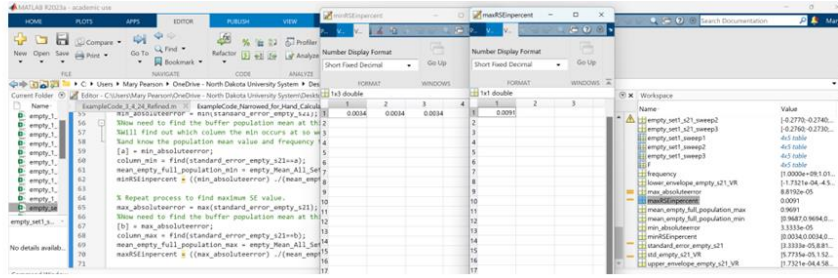


$$AE = | \text{mean}(SE \text{ of entire dataset}) |$$

$$AE = \left| \frac{(3.3333e-05 + 9.9999e-05 + 3.3333e-05 + 3.3333e-05)}{4} \right| = 4.9999e-05$$

Figure F8. Screenshot verifying MATLAB result of absolute average error calculation in comparison to hand calculations located in table.

I. Calculate relative standard error of the 4x3 matrix



$$RSE = \frac{\text{max/min in standard error}}{\text{population mean (at identified max/min standard error frequency)}} * 100\%$$

Min RSE	$\frac{3.3333e-05}{0.9687} \times 100\% = 0.0034\%$
Max RSE	$\frac{9.9999e-05}{0.9687} \times 100\% = 0.0103\%$

Figure F9. Screenshot verifying MATLAB result of relative standard error calculation in comparison to hand calculations located in table.